

Energetic Particles in the Jovian magnetosphere and their relation to auroral emissions

Von der Fakultät für Physik und Geowissenschaften
der Technischen Universität Carolo-Wilhelmina
zu Braunschweig
zur Erlangung des Grades einer
Doktorin der Naturwissenschaften
(Dr.rer.nat.)
genehmigte
Dissertation

von Ana Teresa Monteiro Tomás
aus Lisboa/Portugal

Bibliografische Information Der Deutschen Bibliothek

Die Deutsche Bibliothek verzeichnet diese Publikation in der Deutschen Nationalbibliografie; detaillierte bibliografische Daten sind im Internet über <http://dnb.ddb.de> abrufbar.

1. Referentin oder Referent: Prof. Dr. K.-H. Glassmeier

2. Referentin oder Referent: Prof. Dr. M. K. Dougherty

eingereicht am: 4 Februar 2005

mündliche Prüfung (Disputation) am: 10 Mai 2005

Copyright © Copernicus GmbH 2005

ISBN 3-936586-39-X

Copernicus GmbH, Katlenburg-Lindau

Druck: Schaltungsdienst Lange, Berlin

Printed in Germany

Vorveröffentlichungen der Dissertation

Teilergebnisse aus dieser Arbeit wurden mit Genehmigung der Gemeinsamen Naturwissenschaftlichen Fakultät, vertreten durch den Mentor oder den Betreuer der Arbeit, in folgenden Beiträgen vorab veröffentlicht:

Publikationen

Tomás, A., J. Woch, N. Krupp, A. Lagg, K.-H. Glassmeier, M. K. Dougherty and P. G. Hanlon, *Changes of the energetic particle characteristics in the inner part of the Jovian magnetosphere: a topological study*. Planet. Space Sci., 52, 491-498, 2004.

Tomás, A., J. Woch, N. Krupp, A. Lagg, K.-H. Glassmeier and W. S. Kurth, *Energetic electrons in the inner part of the Jovian magnetosphere and their relation to auroral emissions*. J. Geophys. Res., 109, A06203, doi:10.1029/2004JA010405, 2004.

Woch, J., N. Krupp, A. Lagg and A. Tomás, *The structure and dynamics of the Jovian energetic particle distribution*. Adv. Space Res., 33, 2030-2038, 2004.

Tagungsbeiträge

Tomás, A., J. Woch, N. Krupp, A. Lagg, K.-H. Glassmeier, *Energetic electrons in the inner part of the Jovian magnetosphere and their relation to Jovian aurorae* (Talk), European Geophysical Union (EGU), First General Assembly. Nice, France, 2004.

Tomás, A., J. Woch, N. Krupp, A. Lagg, K.-H. Glassmeier, *Energetic electrons in the inner part of the Jovian magnetosphere and their relation to auroral emissions* (Poster), Deutsche Physikalische Gesellschaft (DPG) - Arbeitsgemeinschaft Extraterrestrische Forschung (AEF), Frühjahrstagung. Kiel, Germany, 2004.

Tomás, A., J. Woch, N. Krupp, A. Lagg, K.-H. Glassmeier, M. K. Dougherty and P. G. Hanlon, K. K. Khurana, R. Prangé, *Changes of the energetic particle characteristics in the inner part of the Jovian magnetosphere and the relation to auroral features* (Poster), European Geophysical Society (EGS)-American Geophysical Union-European Geophysical Union (EGU), Joint Assembly. Nice, France, 2003.

Tomás, A., J. Woch, N. Krupp, A. Lagg, K.-H. Glassmeier, K. K. Khurana, *Changes of the energetic particle characteristics in the inner part of the Jovian magnetosphere and the relation to auroral features* (Talk), Jupiter after Galileo and Cassini - Euroconference

on Giant Planets. Lisbon, Portugal, 2002.

Contents

Vorveröffentlichungen der Dissertation	1
Summary	9
1 The Jovian Magnetosphere	11
1.1 Comparing Earth and Jupiter's magnetosphere: Basic differences	11
1.2 The Exploration of the Jovian Magnetosphere	15
1.3 The Jovian particle environment and magnetic field structure	19
1.4 Charged particle motion	24
1.5 Pitch Angle Diffusion and wave particle interaction	25
1.5.1 Whistler waves in the Jovian magnetosphere	26
1.5.2 The pitch angle diffusion coefficient	27
1.6 The Nishida recirculation model	29
1.7 The Jovian aurorae	31
1.7.1 Spacecraft observations of the Jovian aurorae	31
1.7.2 Characteristics of the Jovian aurorae	33
1.8 Summary	36
2 The Galileo Mission and instrumentation used	37
2.1 The Galileo mission	37
2.2 The EPD instrument	39
2.2.1 Low Energy Magnetospheric Measurement System (LEMMS)	42
2.2.2 The Composition Measurement System (CMS)	45
2.3 The Magnetometer	46
2.4 The Plasma Wave Spectrometer (PWS)	46
2.5 The coordinate system	46
3 Energetic particle and magnetic field observations	49
3.1 Energetic particle and magnetic field characteristics in the Jovian magnetosphere inside $40 R_J$ - A case study	51
3.1.1 Particle Flux and Energy-time spectrogram	51
3.1.2 Magnetic field	53
3.1.3 Energy Spectral Index	54
3.1.4 Pitch angle distribution	57
3.1.5 Further examples	60
3.1.6 Location of the boundaries	63

3.2	Complementary analysis	64
4	Origin of the PAD boundary and relation to auroral emissions	67
4.1	Tracing of magnetic field lines - From the equatorial plane to the ionosphere	67
4.2	The pitch angle boundary and the secondary oval	71
4.3	Simulation of electron pitch angle distribution changes	75
4.4	Pitch angle scattering by whistler waves	82
4.5	Precipitation energy flux	88
4.6	The PAD boundary and the Nishida model	92
5	Summary and conclusions	95
A	Charged particle motion in a magnetosphere	97
A.1	The guiding center approximation	98
A.2	The adiabatic invariants	100
B	Galileo instruments and associated principal investigators	103
C	Record mode coverage	105
D	Jovian magnetic field models	107
	Acknowledgements	121
	Curriculum Vitae	123

List of Figures

1.1	Schematic view of the Earth's magnetosphere	12
1.2	Earth's magnetosphere: Plasma regions and current systems	13
1.3	Birkeland current loop	15
1.4	Trajectories of the missions to Jupiter	18
1.5	Average flow pattern in the Jovian magnetosphere	21
1.6	Anisotropy vectors of protons	23
1.7	Schematic view of plasma flow and associated magnetic field in the Jovian magnetosphere	23
1.8	Charged particle motion in the Jovian magnetosphere	24
1.9	Schematic view of the Nishida recirculation model	30
1.10	HST image of the Jovian northern auroral emissions	32
1.11	Field-aligned current system	34
1.12	Brightness profile of the northern auroral emissions	35
2.1	Sketch of the Galileo orbiter	38
2.2	Sketch of the Energetic Particle Detector	40
2.3	View of the EPD instrument	41
2.4	Cross-section of the LEMMS telescope	43
2.5	The CMS detector	45
2.6	Jupiter coordinate Systems	47
3.1	Galileo orbits showing the EPD coverage	50
3.2	Differential particle flux and energy-time spectrograms	52
3.3	Magnetic field behaviour	53
3.4	Electron pitch angle distribution	54
3.5	Energy Spectra of two proton channels	55
3.6	Spectral index profiles for electrons, protons, sulphur and oxygen	56
3.7	Energy spectra of protons and sulphur	57
3.8	Normalised electron pitch angle distribution	58
3.9	Electron pitch angle distribution in two different regions of the magnetosphere compared to the normalized PAD of electrons	59
3.10	Normalised ion and proton pitch angle distributions	59
3.11	Parameters of the energetic particles and magnetic field components - G7 orbit	61
3.12	Normalised pitch angle distribution of electrons - G7 orbit	62
3.13	Equatorial map of the transition region with particle boundaries location	63
3.14	High resolution normalised electron pitch angle distribution - G28 orbit	65

List of Figures

3.15	High resolution electron pitch angle distribution - G28 orbit	65
3.16	High resolution normalised electron pitch angle distribution - C9 orbit	66
4.1	Footprints with the Khurana model	69
4.2	Footprints with the VIP4 model	70
4.3	Footprints in the northern hemisphere (30 R_J and Io) - Khurana and VIP4 model	70
4.4	Footprints in the northern hemisphere (20 R_J and Ganymede) - Khurana and VIP4 model	71
4.5	HST observations of the satellites footprints	72
4.6	Polar view of the Jovian north auroral zone	72
4.7	Sketch of the Jovian magnetosphere and the auroral emissions in the northern hemisphere	75
4.8	Electron pitch angle distribution - E11 and E26 orbit	77
4.9	Initial electron distribution	78
4.10	Obtaining the final distribution	79
4.11	Simulated normalised pitch angle distribution	80
4.12	Simulated and measured normalised pitch angle distribution	81
4.13	Critical flux compared with the measured flux	83
4.14	Wave frequency-time spectrogram	84
4.15	Pitch Angle distribution of electrons compared with frequency-time spectrogram	85
4.16	Ratio between the pitch angle diffusion coefficient and the strong diffusion limit	87
4.17	Longitudinal dependence of the precipitation energy flux	91
4.18	Streaming index for protons	93
4.19	Ratio of the spectral index for low and high energies	94
A.1	Coordinate system for particle gyration in a inhomogeneous magnetic field . . .	99

List of Tables

2.1	Characteristics of the EPD instrument	42
2.2	Characteristics of the record and real-time mode data	42
2.3	Energy range of the LEMMS ions channels	44
2.4	Energy range of the LEMMS electrons channels	44
4.1	Location of the PAD boundary in the Jovian equatorial plane	73
4.2	Coordinates of the secondary oval	74
4.3	Range of parameters for estimation of the pitch angle diffusion coefficient	86
4.4	Location of the PAD boundary in the Jovian equatorial plane and estimated precipitation fluxes	90
B.1	Galileo Orbiter instruments and the associated principal investigators	104
C.1	Record mode data coverage	105
D.1	Schmidt normalised spherical harmonic coefficients	110

Summary

This thesis discusses the relation between the energetic particle characteristics measured by Galileo in the inner to middle Jovian magnetosphere, and the auroral emissions observed by the Hubble Space Telescope. The thesis determines particle and field properties in the transition region between the dipolar and the current sheet region of the Jovian magnetosphere. The prime focus of the work is on the analysis and interpretation of the electron pitch angle distribution. A discussion is presented on how adiabatic processes and particle diffusion processes, such as pitch angle diffusion by whistler waves, can explain the observed distributions in the equatorial plane and how they can be related to the Jovian auroral emissions. Furthermore, the importance of these mechanisms in the framework of global plasma transport models is discussed.

The introductory chapter briefly describes the fundamental features of the Jovian magnetosphere, with specific emphasis on phenomena which have no equivalence in the Earth's magnetosphere. The most outstanding factors that make the Jovian magnetosphere a particular case are the presence of the moon Io and the fast rotation of the planet. Io is the most important source of plasma in the Jovian magnetosphere releasing 1 ton/s of sulphur and oxygen ions, and therefore clearly conditions the plasma transport, acceleration and diffusion processes. Thus in contrast to the solar wind driven terrestrial magnetosphere, the magnetosphere of Jupiter is rotationally driven. The Chapter summarises the relation of magnetospheric processes and auroral phenomena, specifically the importance of particle diffusion processes for auroral emissions.

Chapter 2 contains a brief description of the relevant features of the Galileo mission and its instrumentation.

The analysis of the energetic particle data and magnetic field data obtained with the Energetic Particles Detector and with the Magnetometer is discussed in Chapter 3. A topological study of the energetic particle evolution (intensity, energy-time spectrograms, spectral index and pitch angle distributions) as well as magnetic field characteristics in the transition region is presented. The most distinct boundary is found in the electron pitch angle distribution (PAD).

Chapter 4 discusses the relation between the PAD boundary and the secondary auroral oval, a discrete feature observed equatorward of the main auroral oval. Magnetic field models are used to trace field lines threading the boundary in the equatorial plane, to the Jovian ionosphere. A simulation of electron pitch angle distribution changes under the assumption of adiabatic motion is performed, and compared with the observed distribution. The possibility of whistler wave generation as an important electron scattering mechanism is discussed. The resulting precipitation fluxes are estimated and compared to the auroral observations. It is concluded that the PAD boundary is the magnetospheric source region of the secondary auroral oval.

1 The Jovian Magnetosphere

1.1 Comparing Earth and Jupiter's magnetosphere: Basic differences

In this chapter the basic differences between the two magnetospheres, Earth and Jupiter are introduced. The magnetosphere of Earth is a well-known system which has been intensively studied for centuries. Jupiter's magnetosphere, in contrary, was not discovered until the 1950's and although our knowledge about it has greatly increased in the recent years, many questions remain open.

The magnetic properties of Earth were discovered in China around the year 1000, when the north-south pointing property of the compass needles was discovered, but only in the 16th century William Gilbert did explain these properties by considering the Earth as a huge magnet. Presently, the Earth's magnetic field is explained by dynamo theory, which considers the effects of convection in the Earth's inner metallic core together with the planetary rotation, to be responsible for electric currents and the magnetic field. To first approximation the Earth's magnetic field is described by a dipole whose axis is inclined about 11° from the spin axis. This magnetic field shields the Earth from the continuous flow of magnetised plasma (mainly protons and electrons) from the Sun's ionised upper atmosphere, the solar wind. The interaction of the solar wind with the Earth's magnetic field distorts the magnetic field lines and forms a cavity known as the magnetosphere.

The Earth's magnetosphere has been extensively studied since its discovery. In particular, the spacecraft era allows one to obtain a profound knowledge of our surroundings. Its basic features are summarised in a greatly oversimplified picture in figures 1.1 and 1.2. The size of the magnetosphere on the dayside is basically determined by the balance between the magnetospheric pressure and the solar wind dynamic pressure (*Russell 2001*). The standoff distance is much shorter on the dayside where the solar wind compresses the magnetosphere, than on the nightside where the magnetic field lines are stretched out in the solar wind downstream direction, creating the magnetotail.

The first point of encounter of the solar wind with the Earth's magnetic field causes a shock due to the fact that the solar wind moves faster than the waves which propagate in the magnetised solar wind plasma. The shock is known as the bow shock. The outer boundary of the magnetosphere is called the magnetopause. The region between the bow shock and the magnetopause is known as the magnetosheath. It is populated by thermalised and decelerated solar wind plasma. Inside the magnetosphere the particle population originates from the solar wind and from the ionosphere. Different regions can be observed on the nightside as one progresses from the high latitude magnetopause

towards the equatorial plane (see e.g. Voigt (1995)).

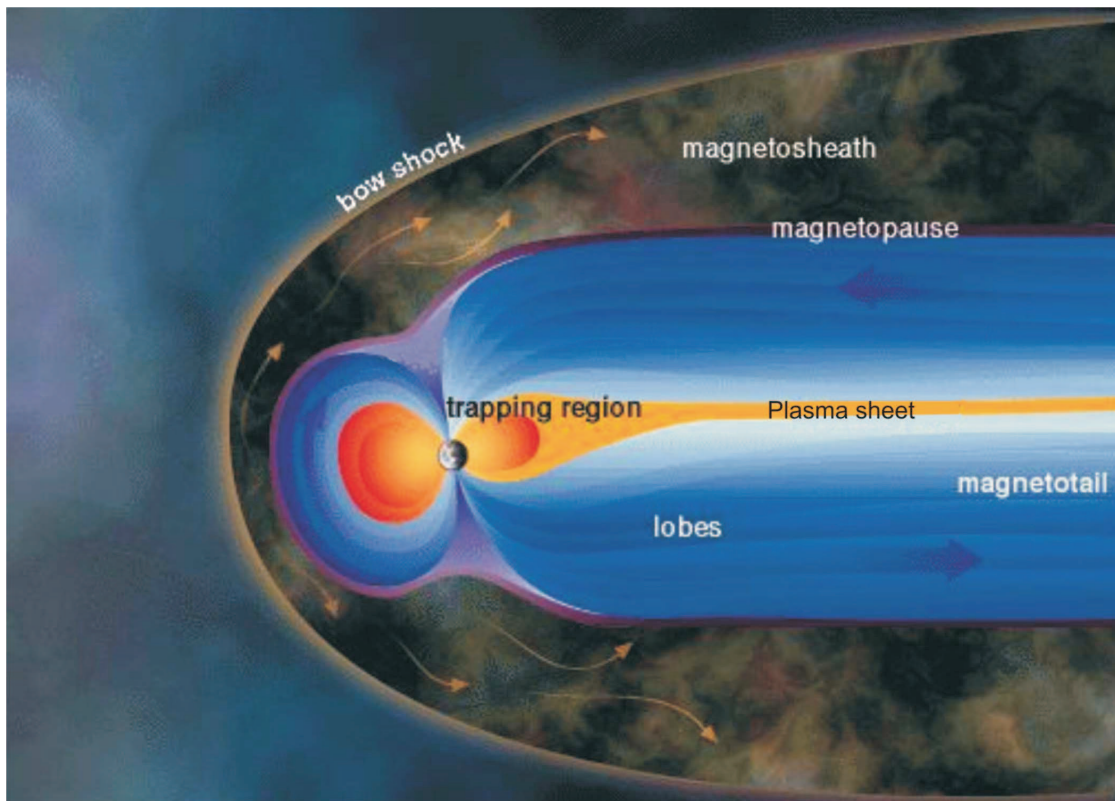


Figure 1.1: View of the Earth's magnetosphere indicating the different plasma regions.

Adjacent to the magnetopause there is a thin layer of plasma originating primarily from the magnetosheath, known as the plasma mantle. This region is followed by the magnetotail lobes, where almost no plasma is found. Close to the equatorial plane, a current sheet and an associated plasma sheet separate the northern from the southern lobe. In the very center of the current sheet, the neutral sheet, the magnetic field strength is weak and the field reverses sign. Closer to the planet is the plasmasphere, a region of closed field lines, which contains corotating high density low energy plasma trapped on the Earth's magnetic field lines. The plasma originates mainly from the ionosphere. The outer boundary of this region is known as the plasmapause. It is located at 4 to 6 R_E ¹ and separates corotating field lines from field lines which are strongly influenced by the solar electric field. Partially coincident with the plasmasphere but extending to distances of 6 to 8 R_E are the radiation or Van Allen belts populated by high energy ionised trapped particles, of solar wind, ionospheric and galactic origin, which are trapped in the Earth's magnetosphere.

A very important aspect of the magnetosphere and its plasma population, is the presence of different electric field and current systems. The convection electric field is generated by the solar wind-magnetosphere-ionosphere coupling. The corotation electric field is associated with the rotation of the planet.

¹The Earth radius (R_E) is 6.378×10^3 Km.

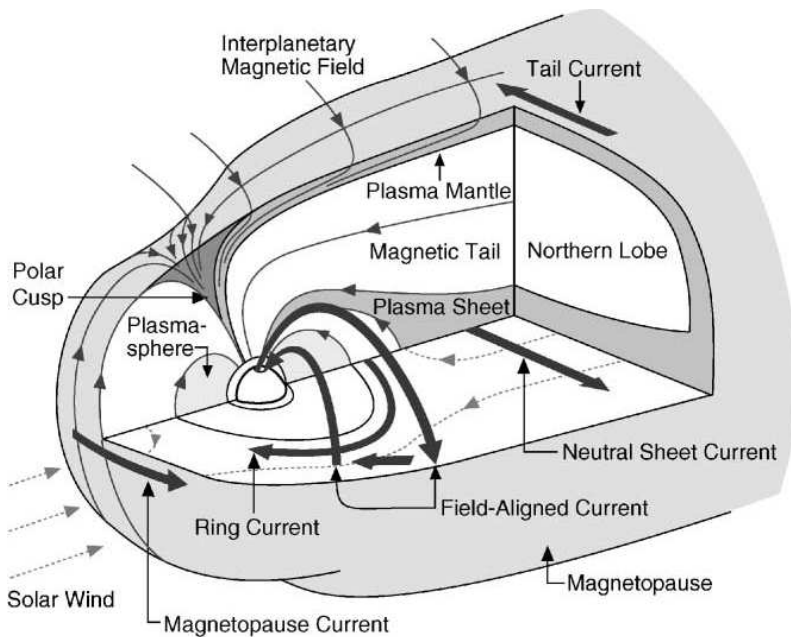


Figure 1.2: View of the Earth's magnetosphere indicating the different plasma regions and current systems (*Russell 2001*).

The convection electric field is related to the dayside magnetic reconnection (merging) of the interplanetary magnetic and the geomagnetic field lines. As a consequence open field lines are created which are connected to the Earth on one side and stretched out into the interplanetary medium on the other side. The open field lines originating at each polar region are then swept back over the polar caps, and the plasma in the associated flux tubes experiences a dawn-to-dusk solar wind electric field. The field lines will then reconnect in the magnetotail, forming a new set of closed field lines which are returned to the dayside by the planet's rotation, thereby recovering the magnetic flux. In general the convection electric field causes the motion of particles from the magnetotail in the sunward direction and induces a large scale circulation of the plasma. The separation region between open and closed field lines becomes visible through auroral emissions, it forms part of the auroral oval. The corotation electric field causes the plasma to drift azimuthally due to the $\mathbf{E} \times \mathbf{B}$ drift. This drift motion is not charge dependent and both electrons and protons corotate with the planet. The plasma motion due to the corotational electric field is of major importance only closer to the planet, in the plasmasphere, while the plasma motion due to the convection electric field is of greater importance further out.

An important azimuthal drift of particles is caused by the curvature of the magnetic field lines and the magnetic field gradient (due to the decrease of the field with increasing radial distance). In this case the charge of the particles is of importance. Electrons drift eastward, protons drift westward. The resulting current is known as the ring current. The coupling of the solar wind-magnetosphere-ionosphere system generates large scale current systems. On the nightside the magnetopause surface current, which ensures force balance across the magnetopause boundary closes through the cross tail neutral sheet current. On the dayside it is partly closed by a current loop system via field-aligned currents

(FAC) so-called Birkeland currents, and the ionospheric Hall and Pedersen currents. During times of specifically strong solar wind magnetopause interaction, the neutral sheet current may disrupt and divert through FACs into the ionosphere. The FACs are of particular importance for the Earth's aurora, where the most intense discrete aurora is caused by the precipitation of electrons into the ionosphere which are accelerated by parallel electric potential drops along the magnetic field lines in upward parallel current regions (*Russell 2001*).

This summarises some of the most important aspects of the Earth's magnetosphere, but what about other planets? Are their magnetospheres similar or are there significant differences? It was not unexpected that other planets, such as Jupiter, would have a magnetosphere, but it wasn't until 1955 that it was inferred from radio measurements that Jupiter indeed had a magnetic field (*Burke and Franklin 1955*). Initially the models developed for the Jovian magnetosphere were Earth-like models but with the spacecraft exploration of the Jovian system it soon became clear that significant differences between these two systems exist.

One of the most obvious differences is the size of the magnetosphere, which is to first order, governed by the balance between the magnetospheric pressure and the solar wind dynamic pressure, as previously mentioned. The dynamic pressure of the solar wind decreases with the square of the distance to the Sun, making it 25 times smaller at Jupiter than at Earth. In addition Jupiter's magnetic moment is about 20 000 times bigger than Earth's ², which results in a distance to the subsolar point in Jupiter's magnetopause of about 100 times the terrestrial distance (*Russell 2001*).

At Earth dynamical processes are externally controlled by the solar wind kinetic properties and the strength and orientation of the interplanetary field. At Jupiter dynamics and also the configuration are controlled mainly by two internal factors: the fast rotation of the planet and the presence of the moon Io, which releases 1 ton/sec of neutral atoms due to its volcanic activity. This has very important consequences for the global configuration and dynamics of Jupiter's magnetosphere. The atoms become ionised and a torus of hot ions is formed around the planet. Due to largely unknown processes the plasma is then transported outwards. Centrifugal forces confine the plasma to the equatorial plane leading and stretching the magnetic field lines, forming a magnetodisk. The fast rotation of the planet (approximately 10 hours) causes strong rotational electric fields which maintain the plasma in corotation up to large radial distances. Theoretical considerations show that Jupiter's plasmopause (the boundary up to which plasma convection is dominated by rotation) would extend beyond the magnetopause (*Kennel and Coroniti 1977*). The fact that, to large extent, Jupiter's corotational electric field is stronger than the convection electric field is an indicator of an internally driven magnetosphere. The situation is opposite at Earth, where the convection electric field dominates, indicating an externally driven magnetosphere. The fast corotation also has consequences on the stability of the system. While at Earth the magnetosphere and specifically its tail is driven unstable by solar wind forcing and energy input, at Jupiter instability arises primarily through internal processes such as mass loading (*Woch et al. 1998, Kronberg et al. 2005*).

The Jovian aurora shows a complex variety of features, such as the satellite footprints, which have no correspondence on Earth. The brightest discrete emissions at Jupiter form

²The dipole magnetic moment at Earth is $8.05 \times 10^{22} \text{ Am}^2$ (*Russell 2001*)

the main auroral oval. These emissions are 10 times brighter and 100 times more energetic than at Earth. It is now widely accepted (*Cowley and Bunce 2001*) that the main auroral oval emissions are not related to the boundary region between open and closed field lines or substorms like at Earth, and thus mainly controlled by solar wind-magnetosphere interactions, but associated with the breakdown of corotation in the middle magnetosphere and the generation of field-aligned currents (*Cowley and Bunce 2001, Hill 2004*), as can be seen in figure 1.3 (this process is explained in section 1.7). Thus it is generated by a fully internal process as evidenced by the observation that at Jupiter the main auroral features corotate with the planet, which does not happen at Earth.

Jupiter's magnetosphere is therefore to a large extent different from Earth's. In the following section the magnetosphere of Jupiter is described in greater detail.

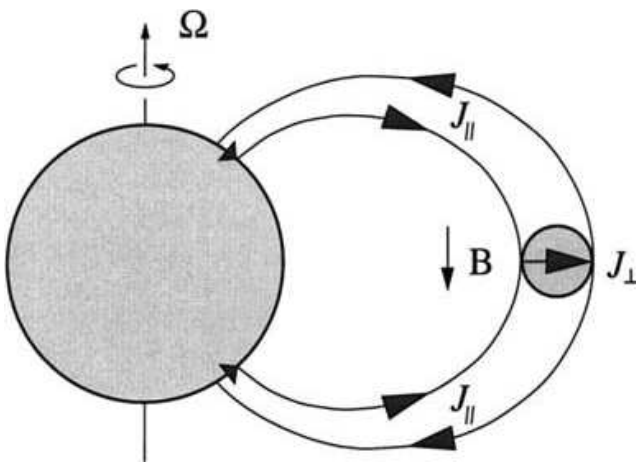


Figure 1.3: Birkeland current loop (*Hill 2004*). Ω is the angular velocity of the planet, J_{\parallel} the field-aligned currents, B the magnetic field.

1.2 The Exploration of the Jovian Magnetosphere

As previously mentioned the Jovian magnetosphere is the region in space controlled by Jupiter's magnetic field. It is a complex region with a variety of processes determining its structure and dynamics, which has intrigued scientists ever since it was discovered. Before the spacecraft exploration of the Jovian magnetosphere began, all the knowledge was obtained from ground-based observations and theoretical models based on the only magnetosphere which had been thoroughly studied, the Earth's one.

The existence of a magnetic field at Jupiter was inferred by *Burke and Franklin (1955)* from observations of circularly polarised decametric radiation (DAM, in the frequency range $0.1 \text{ MHz} \leq f \leq 40 \text{ MHz}$) and later confirmed by observations of decimetric radiation (DIM, in the frequency range $100 \text{ MHz} \leq f \leq 3000 \text{ MHz}$) due to synchrotron emissions. The synchrotron emission is the result of the acceleration that a charged particle experiences as it moves along a helical path in a magnetic field. The characteristics of the emissions which were observed, such as a non-thermal spectrum with a high degree

of linear polarisation and a small degree of circular polarisation and a beaming effect, indicated the presence of trapped high energy electrons in a dipole magnetic field. It also gave indications of the angle of inclination between the rotation and the dipole axis. In a first approach the magnetic field in the region where the trapped particles were located, was estimated to be ~ 2 G, corresponding to a magnetic moment of $M = 1.4 \times 10^{27}$ Am² (Goertz 1976). In the years following the discovery of Jupiter's magnetic field the continuous observations of radio emissions provided accurate measurements of Jupiter's rotation period and led to the development of the longitude system III (1957), corrected in 1965 to what is now the system III (SIII) in use. In the middle of the 1960's, measurements of the circular polarisation allowed to determine the direction of the magnetic field. It was concluded that it points southward at the equator, which means that the field lines emerge from the north pole and converge towards the south pole, opposite to the Earth's case. Theoretical investigations studied the impact of the different ambient conditions surrounding Jupiter, which were obtained by extrapolating the solar wind parameters from 1 to 5 AU³ (Carr and Gulkis 1969) and the effects of the fast rotation of the planet. Other properties derived only from theoretical work included the electron energy and pitch angle distributions necessary to emit the observed synchrotron radiation, and a centred dipole with an inclination of 10° from the rotation axis, but the results at this time were considered doubtful (Carr and Gulkis 1969).

Many questions remained unanswered at the time. The origin of the particles and how they are accelerated and transported in the magnetosphere were the most important unknowns.

It wasn't until the early 1970's that the knowledge of the Jovian magnetosphere greatly evolved with the first fly-by of a man-made spacecraft at an outer planet, Pioneer 10 followed by Pioneer 11. Pioneer 10 was launched in 1972 and arrived at Jupiter in 1973. It was the first mission to be sent to the outer Solar System and the first to explore the giant planet and its magnetosphere. A year later (in 1973) Pioneer 11 followed its sibling spacecraft. In addition to further investigate Jupiter, it became the first spacecraft to explore Saturn. Both spacecraft contained important experimental packages intended to study the Jovian system, its aurorae, radio waves, energetic particle population and the satellites. The trajectories of Pioneer 10 and 11 were chosen to complement each other, with Pioneer 10 in a nearly equatorial trajectory, with closest approach to the planet at $2.8 R_J$ ⁴, while Pioneer 11 approached Jupiter near the equator and exited at northern latitudes of 30° with the closest approach occurring at $1.59 R_J$. These two spacecraft were the first to provide in-situ measurements adding a valuable contribution to the understanding of the Jovian system, answering some of the major questions, in particular concerning the structure of the magnetosphere and the energetic particle distribution. However they posed many new questions.

This led the way to the development of two other fly-by missions, Voyager 1 and 2 in 1979. The Voyager 1 and 2 fly-bys were a major step to better understand some of the remaining questions about the Jovian magnetosphere. Voyager 1 closest approach to Jupiter occurred at $\sim 5 R_J$ while for Voyager 2 this distance was of $\sim 10 R_J$. The trajectories of both spacecraft complemented each other, with Voyager 2 approaching the planet at higher latitudes than Voyager 1 and exiting through the magnetotail. Both

³The astronomical unit (AU) is 1.496×10^8 Km.

⁴The Jovian radius (R_J) is 71.492×10^3 Km.

missions had close encounters with the Galilean moons. Of particular importance was the close fly-by to Io by Voyager 1. The instruments on board the Voyager 1 and 2 spacecraft extended the measured energy ranges from the Pioneer spacecraft, allowing to obtain low energy (≤ 200 keV) ion measurements.

In 1992 another fly-by of the Jovian system gave the opportunity to complement the previous missions. The main aim of the Ulysses spacecraft was to study the interplanetary space out of the ecliptic plane and in particular the poles of the Sun. To be able to perform the needed trajectory the gravity force of Jupiter was used to redirect the spacecraft. The Ulysses inbound trajectory was similar to the previous fly-bys, approaching the planet from 10:00h local time, then reaching high latitudes close to the planet. During the outbound pass Ulysses crossed the dusk side, at high southern latitudes, a region which had not been studied previously.

One of the most important moments in the exploration of the Jovian magnetosphere was the arrival of Galileo in 1995. Galileo was the first, and up to now the only, orbiter exploring this unique system. The 8 years orbit of Galileo (1995-2003) provided an extensive and unique database giving the opportunity to further disentangle the mysteries of the Jovian magnetosphere. This mission is presented in detail in Chapter 2.

The sixth fly-by mission through the Jovian system was Cassini. Launched in October 1997, the spacecraft passed Jupiter between October 2000 and April 2001 on its way to Saturn. Cassini investigated for the first time the dusk to midnight magnetosheath of the planet in the equatorial plane. The closest approach occurred at $138 R_J$. This was a unique fly-by since it was the first time that two spacecraft (Galileo was already in orbit) investigated Jupiter simultaneously. While Cassini was still outside the magnetosphere its trajectory gave a complementary view to that of Galileo allowing to see how the solar wind conditions influence the magnetosphere. A comparative view of the trajectories of these missions can be seen in figure 1.4.

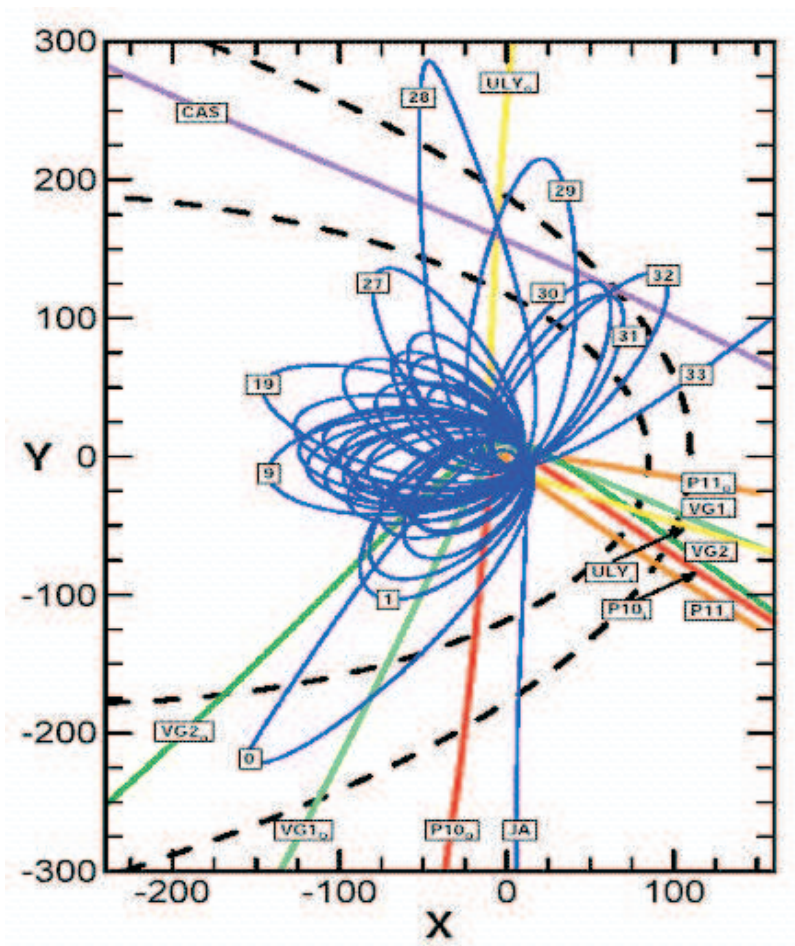


Figure 1.4: . Comparative view of the trajectories of the different missions, in the $x - y$ plane of the Jupiter Solar Ecliptic (JSE) coordinate system. Pioneer 10 and 11 fly-bys are shown in red and orange (respectively), Voyager 1 and 2 are shown in green, Ulysses is shown in yellow, Cassini in violet and in blue are the Galileo orbits. The Sun is to the right of the figure. Dotted lines indicate nominal bow shock and magnetopause locations.

1.3 The Jovian particle environment and magnetic field structure

Already, from the measurements obtained by the first fly-by missions, the Jovian magnetosphere has been divided into three different regions: the inner, middle and outer region. In the following the current knowledge of these three regions of the magnetosphere will be described, focusing on the magnetic field structure and on the energetic particle measurements, as observed during the fly-bys and by the Galileo orbiter.

The existence of a strong magnetic field with a dipole moment of 4.2 GR_J^3 (which is 10^4 times stronger than the one at Earth) was confirmed by all the missions. The dipole axis was found to be tilted by 9.8° from the rotation axis.

The inner magnetosphere

The inner part of the Jovian magnetosphere is the region where the internal planetary field dominates. It extends to approximately $10 R_J$. This region is characterised by a close to dipolar field, and a periodic 10 hour fluctuation in the particle fluxes and the magnetic field due to the rotation of the tilted dipole. The higher magnetic field moments detected (initially by Pioneer and Voyager) led to the development of field models with dipole, quadrupole and octupole moments.

One of the most important features for this region is the existence of active volcanos at Io, which orbits Jupiter at $6 R_J$, first detected by Voyager 1 (*Morabito et al.* 1979). With these measurements it became clear that Io is the most important source of plasma. It continuously releases 1 ton/s of sulphur and oxygen in neutral gas form. The neutrals accumulate first in a torus around Jupiter and are then partly ionised and released into the Jovian magnetosphere (see *Thomas et al.* (2004) for a review).

Furthermore, the presence of H_3^+ was detected by Voyager. It indicated that the ionosphere is also a plasma source (*Hamilton et al.* 1980). Studies of the plasma phase space densities showed that the energetic particles are transported inwards by radial diffusion and accelerated adiabatically to high energies. A decrease in the particle fluxes observed at the orbit of Io and, to a lesser extent, at the orbits of Europa and Amalthea, allowed for an estimate of the radial diffusion coefficient, radial diffusion being considered the principal mode of transport in this region. The loss of particles was believed to be mostly due to wave-particle interaction which scatters the particles into the loss cone. Also satellite absorption contributes to particle loss. It was observed that the primary source of energy is the fast planetary rotation which enforces plasma corotation (*Goertz and Thomsen* 1979). The particle instrument onboard the different missions covered various energy ranges for both electrons and ions. Combining the measurements it was possible to show that the particle energy spectrum can be fitted by a convected Maxwellian distribution for energies $\lesssim 200 \text{ keV}$ and a power law of the form $E^{-\gamma}$ describing a non-thermal high energy tail (*Krimigis et al.* 1979). This region of the magnetosphere is also characterised by a nearly constant spectral shape without major temporal or spatial variations (*Krimigis et al.* 1979).

Another aspect of the particle distribution which is particularly important is the pitch angle distribution. The pitch angle is defined as the angle between the particle velocity and the magnetic field direction. The details of particle motion in magnetic fields are

discussed in the following section. In the inner region the pitch angle distribution of both ions and electrons is found to be a trapped or pancake distribution, with a maximum of the particle flux at 90° perpendicular to the magnetic field direction (*Goertz and Thomsen 1979*), similar to the Earth's radiation belts.

The middle magnetosphere

The middle magnetosphere covers the region from approximately $10 R_J$ up to $40 R_J$. The measurements in this region of the magnetosphere revealed a thin azimuthal current sheet as the dominant feature, which resulted in radially stretched magnetic field lines, leading to a dominant radial field in contrast to the dipolar field in the inner region. The plasma was found to be confined in a narrow sheet around the current sheet. Its origin was assumed to be due to the centrifugal force acting on the trapped plasma. Current sheet crossings were detected by a reduction in the magnetic field magnitude and a reversal of the radial field component and a maximum in the particle intensities. One of the most important observations made by Ulysses was the existence of field-aligned currents, visible in the sharp gradients of ΔB_ϕ which represent localised current sheets (*Dougherty et al. 1993*). These field-aligned currents, revealed the transfer of momentum from the high-latitude ionosphere of the planet to the equatorial region of the middle magnetosphere in order to enforce plasma corotation (*Dougherty et al. 1993*).

Beside the change from a dipolar to a radial magnetic field, another aspect which lead to the distinction of inner and middle magnetosphere is the change in the particle pitch angle distribution, from a mostly pancake distribution in the inner magnetosphere to an isotropic or bi-directional distribution further out (*Goertz and Thomsen 1979*).

In regions of $R \gtrsim 25 R_J$, a strong local time dependence in the electron pitch angle distributions was observed (*Krimigis and Roelof 1983*). For the same region a softening of the energy spectral slope with increasing radial distance was also observed, for oxygen, sulphur and helium (*Hamilton et al. 1981*). The change of the pitch angle distribution posed some questions as to the transport mode of particles in this region. One of the suggested explanations is the existence of a local source of small pitch angle particles, which are part of a recirculation process (*Goertz and Thomsen 1979*). Other suggestions indicated that the injection of an isotropic distribution at radial distances $\leq 12 R_J$, would diffuse outwards driving the particles to smaller pitch angles, or the existence in the middle magnetosphere of a loss process acting preferentially on large pitch angle particles. This transition will be further discussed in Chapter 3.1.

Calculation of the ion anisotropy, based on the measurements of the Energetic Particles Detector onboard Galileo, allowed to determine the global particle flow pattern (*Krupp et al. 2001*). Figure 1.5 shows the average flow pattern in the equatorial plane of the Jovian magnetosphere (*Woch et al. 2004*). The flow is corotational up to $150 R_J$, the largest distance reached by Galileo. It can be seen that the flow velocity does not increase with radial distance as would be the case for rigid corotation. A strong deviation from rigid corotation occurs in the middle magnetosphere and the plasma flow velocity is sub-corotational for most of the Jovian magnetotail (*Krupp et al. 2001*). A pronounced local time asymmetry is visible in the flow pattern. The ions are observed to corotate in the predawn-noon sector, even at relatively large distances from the planet, while in the postnoon-postdusk sector they are sub-corotating already close to the planet.

Another important dawn-dusk asymmetry is visible in the thickness of the current sheet (*Kivelson and Khurana 2002*). The magnetic field properties measured by the magnetometer on board Galileo indicated that a thinner current sheet is present on the dawn side, as opposed to a thicker current sheet on the dusk side.

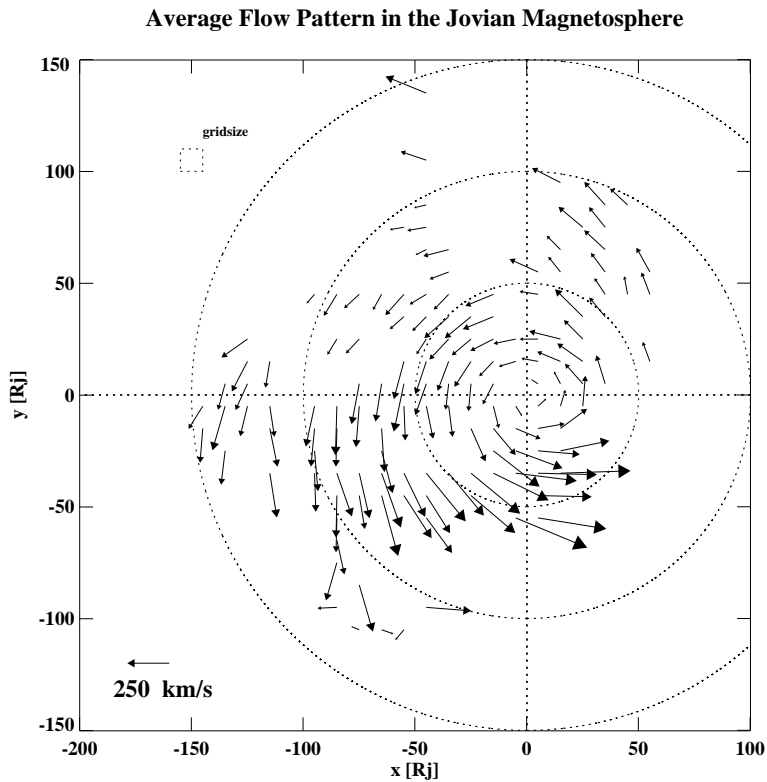


Figure 1.5: Global averaged view of the ion flow estimations based on 30 min average measurements taken throughout the Galileo orbiting period, from 1995 to 2002. The vectors shown result from binning the ion flow values into a $10 \times 10 R_J$ grid and averaging (from *Woch et al. (2004)*).

The outer magnetosphere

The outer magnetosphere covers the region from $40 R_J$ up to the magnetopause including the magnetotail. The location of the magnetopause was observed to vary considerably. The magnetopause was recorded by Pioneer 10 at $96.4 R_J$ inbound and $80 R_J$ outbound and by Pioneer 11 at $97 R_J$ outbound which confirmed the huge extent of the magnetosphere (Opp 1974, 1975, Smith *et al.* 1974, 1975). The fly-bys of Voyager 1 and 2 showed that the magnetopause location varies from $\sim 45 R_J$ to $\sim 100 R_J$ (Acuña *et al.* 1983). During the Ulysses fly-by in 1992 the magnetosphere was even more expanded. In the outer magnetosphere the magnetic field was observed to be predominantly southward with strong time and spatial variations. The existence of the magnetotail was first confirmed by the Voyager measurements, which showed that at large radial distances the current sheet aligned with the magnetic equator, changes to a tail current sheet with the field parallel to the ecliptic plane (Ness *et al.* 1979).

The outer part of the magnetosphere revealed strong spatial and temporal variations in flux and angular distribution whereas averages of the electron and proton fluxes over 10 hours remained nearly constant with radial distance, the particle spectra being similar to that in the middle magnetosphere. Observations with Cassini showed that the electron distribution remained bi-directional on the duskside of the magnetosphere up to $200 R_J$, which indicated closed magnetic field lines at that distance (Krupp *et al.* 2004b).

One of the most important features occurring in the magnetotail are the quasi-periodic bursts of energetic particles, detected by the energetic particle measurements (Woch *et al.* 1998, 1999, Krupp *et al.* 1998, Kronberg *et al.* 2005). These are strongly collimated particle jets directed predominantly radially outward or inward, occurring every 2 to 4 days. Figure 1.6 shows the first order anisotropy vectors for protons, during one of the Galileo orbits in the predawn sector. According to Woch *et al.* (1998) these bursts suggest a reconfiguration process between two different states of the magnetosphere, one of plasma loading and the other of plasma unloading. This process is related to the centrifugally driven reconnection scenario in the Jovian magnetotail suggested by Vasyliūnas (1983). Figure 1.7 shows a sketch of the expected flow pattern and the magnetic field topology.

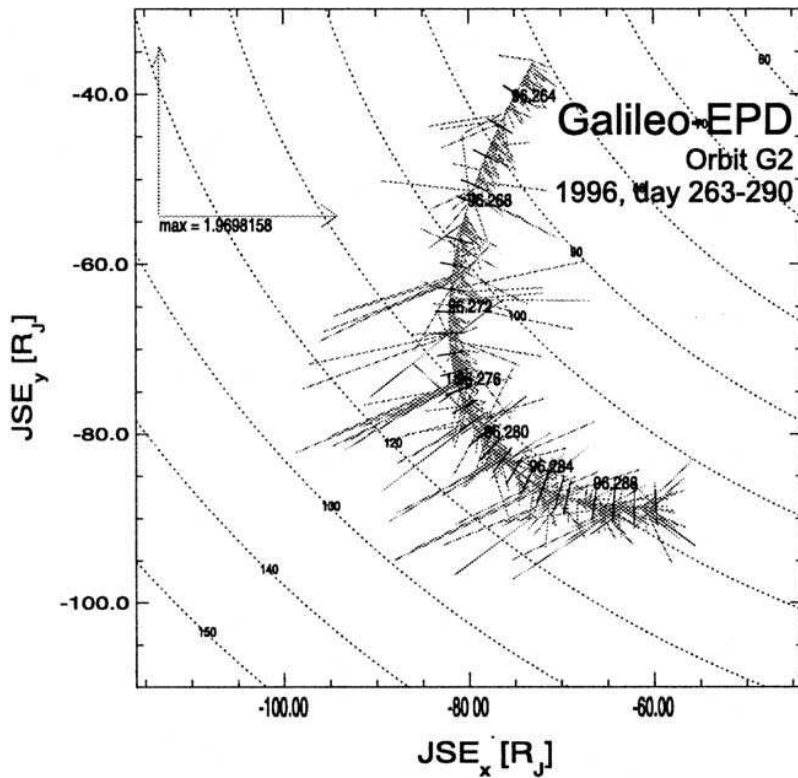


Figure 1.6: First-order anisotropy vectors of protons (in the energy range 80 to 220 keV) projected into the equatorial plane of Jupiter. The vectors are plotted along one of the Galileo orbits in the predawn section of the Jovian magnetosphere (from *Krupp et al. (1998)*).

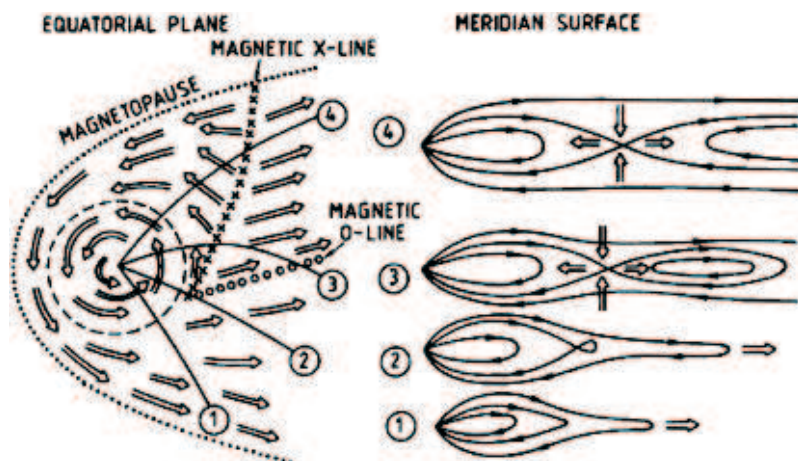


Figure 1.7: Left panel: schematic view of the plasma flow in the equatorial plane. Right panel: associated magnetic field and plasma flow in a sequence of meridian surface (from *Vasyliūnas (1983)*).

1.4 Charged particle motion

In the previous sections it was seen how the different missions to the Jovian system have given us a global view of the energetic particle environment and magnetic field structure of the Jovian magnetosphere. The charged particle distributions are very sensitive to the magnetosphere structure and any changes thereof. Thus the study of their behaviour is of great importance to our knowledge of the magnetosphere, helping us to define the magnetic field geometry, and the physical processes occurring therein, such as particle acceleration, transport and loss. In this section a brief introduction to the basic behaviour of a charged particle in a magnetic field will be given, and some of the most important plasma processes occurring in the Jovian magnetosphere will be addressed.

The charged particle populations, electrons and ions, in a magnetosphere are influenced by the electric (\mathbf{E}) and magnetic (\mathbf{B}) fields. The motion of charged particles in electromagnetic fields is governed by the Maxwell equations and the Lorentz force. The particle describes three types of motion: gyromotion around the field line, bounce motion along the field line between mirror points and drift motion around the planet as the scheme in figure 1.8 shows. Each of these three motions has associated a quantity, known as adiabatic invariant, that will remain constant if changes in the magnetic field are small when compared to the characteristic time scales of the particle motion. The derivation of the equations leading to the detailed particle motion is given in Appendix A.

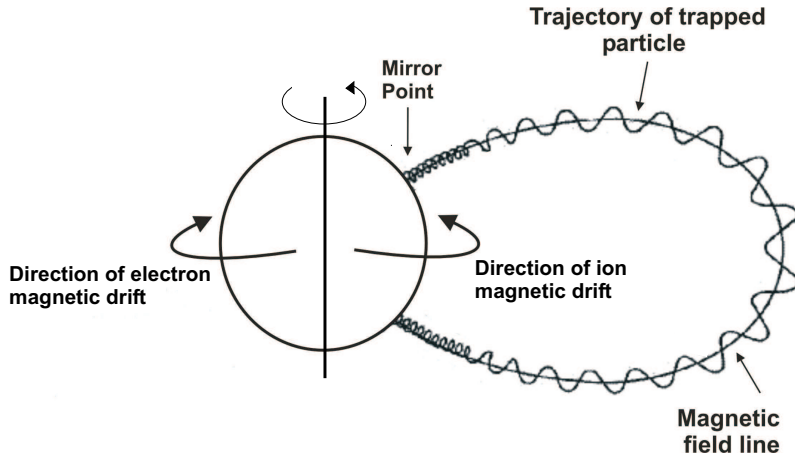


Figure 1.8: Trajectory of trapped particles showing the gyromotion, bouncing motion and the magnetic drift around the planet (adapted from *Walt* (1994)).

The first adiabatic invariant is associated with the gyromotion of the particle. It is normally expressed by the magnetic moment μ of the particle:

$$\mu = \frac{p_{\perp}^2}{2mB} = \frac{W_{\perp}}{B} = \text{constant} = \frac{W \sin^2 \alpha}{B} \quad (1.1)$$

where B is the magnetic field magnitude, p_{\perp} the perpendicular momentum of the particle, m its mass, W_{\perp} the kinetic energy, and α the pitch angle of the particle (e.g. *Walt* (1994)). From this relation one can see that the pitch angle of a particle increases as it moves towards higher magnetic fields. When the pitch angle reaches 90° the particle is at its mirror point and reverses direction.

The second adiabatic invariant is related to the bounce motion of the particle along a field line. It can be expressed only in terms of the magnetic field geometry for a certain location, by considering a quantity k which is defined for a particle of momentum p mirroring at that point. In this case k is expressed as:

$$k = \int_{S_m}^{S'_m} \sqrt{\left[1 - \frac{B(s)}{B_m}\right]} ds \quad (1.2)$$

where S_m and S'_m are the mirror points, $B(s)$ is the magnetic field magnitude at any location s along the field line and B_m is the magnetic field magnitude at the mirror point. Using this invariant it is possible to define the particle's drift path and the surfaces defined by the bouncing and drifting of the particle.

The third adiabatic invariant is related to the longitudinal drift motion of the particle around the planet. It is given by:

$$J_3 = q\Phi \quad (1.3)$$

Φ is the magnetic flux enclosed by the drift path, and q is the particle charge.

If these adiabatic invariants remain constant the particles are trapped and remain confined indefinitely. But in a magnetosphere the adiabatic invariants are not always strictly conserved, particles are injected, accelerated, diffused and lost.

Diffusion is one of the processes by which particles are transported in the magnetosphere and it can also lead to the loss of particles from the magnetosphere. Diffusion is caused by violation of one or more of the adiabatic invariants by non-adiabatic fluctuations of the magnetic field or by external forces. There are two main types of diffusion processes: radial diffusion, which moves particles across drift shells and pitch angle diffusion, in which the particle mirror point is moved along the field lines. Inward radial diffusion by violation of the third adiabatic invariant is one of the classical means of particle acceleration, while pitch angle diffusion, due to lowering of their mirror points and resulting collision with the atmosphere, caused e.g. by wave-particle interaction, is responsible for the loss of particles. A more general and detailed description of particle motion in a magnetosphere (specifically applied to the terrestrial case) can be seen in *Walt* (1994) and *Roederer* (1970).

1.5 Pitch Angle Diffusion and wave particle interaction

In this section pitch angle diffusion as a mechanism for particle loss in magnetospheres is addressed. In particular the estimation of the diffusion coefficient in the case of particle scattering by whistler waves will be discussed.

Pitch angle diffusion occurs when a mechanism acts on the particle changing its pitch angle. This can lead to loss of the particle if its pitch angle falls into the loss cone. The loss cone defines a limit value for the pitch angle. If the particle's pitch angle lies within the loss cone the particle's mirror point is too deep in the atmosphere and the particle will be lost (*Roederer* 1970). It can be caused by a variety of mechanisms, such as atmospheric scattering of electrons or wave-particle interaction. For the wave-particle interac-

tion mechanism, studies indicate scattering by whistler waves as the dominant mechanism for electron diffusion and ion cyclotron waves for the ions (*Walt 1994*).

In this work the focus is on the pitch angle diffusion by whistler waves. The interaction with the waves can lead to scattering of electrons towards small pitch angles, consequent precipitation into the ionosphere, and possible excitation of auroral emissions.

1.5.1 Whistler waves in the Jovian magnetosphere

Whistler waves are one of the modes of propagation of electromagnetic waves. The whistler waves in the Jovian magnetosphere were initially discovered by the Voyager 1 plasma wave instrument (*Scarf et al. 1979*). There are four types of whistler mode signals: lightning generated whistler, chorus, hiss and auroral hiss (*Gurnett and Scarf 1983*). As the name indicates, the first type is generated by lightning at Jupiter (or Earth), the auroral hiss gets its name from a type of whistler mode noise observed at the Earth's aurora. The chorus and the hiss mode are spontaneously generated within the magnetospheres by interaction with energetic electrons. The chorus emissions occur at frequencies of 8 kHz to 12 kHz, while the hiss emissions occur at lower frequencies, below 2 kHz. The last mode is of particular importance in this work since these emissions are associated with wave particle interactions which lead to pitch angle scattering.

A theory of the whistler mode emissions applying for both chorus and hiss was developed by *Kennel and Petschek (1966)*. They identify the electron pitch angle anisotropy produced by the atmospheric loss cone as the free energy source for causing the whistler mode instability in a magnetosphere. The authors consider that the violation of the first adiabatic invariant is responsible for the untrapping of particles and consequent precipitation. This means that changes in the pitch angle of the particle occur without changes in the energy. The conditions for violation of the first adiabatic invariant require the particle to see fluctuations near its own gyrofrequency. This suggests whistler waves for electrons and ion cyclotron waves for ions, as the likely waves to interact with the particles. In the following discussion only the interaction between electrons and whistler waves will be discussed, since they are of particular interest to this work.

If the pitch angle distribution is anisotropic, with more energy perpendicular than parallel to the magnetic field, a particle distribution is unstable. There is free energy to cause whistler mode instability. The whistler waves interact with the electrons leading to pitch angle diffusion, which results in particle precipitation into the ionosphere. The loss of particles creates a pitch angle distribution which does not allow for further wave growth, limiting the diffusion and loss. The anisotropy in the pitch angle distribution is the source of energy for wave growth. The growth rate is dependent on the amount of particles which are resonant. For electron gyroresonance, the resonant velocity V_R is defined by $kV_R = \omega - |\Omega_e|$, where k is the wave number, ω the wave frequency and Ω_e the electron gyrofrequency. This means that the velocity of the particles parallel to the magnetic field will Doppler shift the wave frequency to their gyrofrequency (because the whistler signals usually have lower frequency than Ω_e and must be Doppler shifted to produce resonance). Only the parallel waves are considered since these are the most important for pitch angle scattering.

Electrons will be accelerated or decelerated depending on their phase with respect to the wave, and therefore the appropriate velocity gradients must be present to achieve wave

growth. *Kennel and Petschek* (1966) consider only regions of the magnetosphere where the number of resonant electrons is small and therefore also the wave growth is limited. Applying these principles to a specific electron distribution F , *Kennel and Petschek* (1966) find that the growth rate is given by:

$$\gamma = \pi |\Omega_c| \left(1 - \frac{w}{|\Omega_c|}\right)^2 \eta(V_R) \cdot \left\{ A(V_R) - \frac{1}{|\Omega_c|/w - 1} \right\} \quad (1.4)$$

with the fraction of electrons which resonate given by:

$$\eta(V_R) = 2\pi \frac{|\Omega_c| - \omega}{k} \int_0^\infty v_\perp dv_\perp F(v_\perp, v_\parallel = V_R) \quad (1.5)$$

This expression gives the fraction of particles in a range Δv_\parallel about cyclotron resonance, reflecting the fact that an electron must have a specific parallel velocity (v_\parallel) to be resonant with the waves, while all the perpendicular velocities are possible.

The measure of the pitch angle anisotropy is given by :

$$A(V_R) = \frac{\int_0^\infty v_\perp dv_\perp \tan \alpha \frac{\partial F}{\partial \alpha}}{2 \int_0^\infty v_\perp dv_\perp} \Bigg|_{v_\parallel = V_R} \quad (1.6)$$

It depends only on the gradient of the distribution function with respect to the pitch angle at constant energy. If the gradient is positive the distribution at constant energy will increase towards 90° pitch angle, with more energy perpendicular than parallel to the magnetic field, which is the instability condition.

How the whistler waves interact with the particles and lead to pitch angle diffusion is explained in the next section.

1.5.2 The pitch angle diffusion coefficient

The wave-particle interaction is a stochastic process which can be described by the Fokker-Planck formalism, i.e, according to *Kennel and Petschek* (1966) the particle distribution function (F) obeys the equation:

$$\frac{\partial F}{\partial t} = \frac{1}{\sin \alpha} \frac{\partial}{\partial \alpha} \left\{ -\sin \alpha \frac{\langle \Delta \alpha \rangle}{\Delta t} F + \sin \alpha \frac{\partial}{\partial \alpha} (DF) \right\} \quad (1.7)$$

where D is the pitch angle diffusion coefficient obtained by knowing the mean square change per unit time of the pitch angle (α):

$$D = \frac{\langle (\Delta \alpha)^2 \rangle}{\Delta t} \quad (1.8)$$

The angle brackets indicate an average over all the possible pitch angle changes and Δt is the mean interval between wave collisions. The first term in the brackets is called dynamic friction. Since it contains the average of the change in pitch angle ($\langle \Delta \alpha \rangle$) this term is zero, because the probability of increases or decreases in α are similar.

Differentiating the second term of the equation yields:

$$\frac{\partial F}{\partial t} = \frac{1}{\sin \alpha} \frac{\partial}{\partial \alpha} \left\{ \sin \alpha \frac{\partial D}{\partial \alpha} F + \sin \alpha D \frac{\partial F}{\partial \alpha} \right\} \quad (1.9)$$

Using the definition of D implies:

$$\frac{\partial D}{\partial \alpha} = \left\langle \Delta \alpha \frac{\partial}{\partial \alpha} \left(\frac{\Delta \alpha}{\Delta t} \right) \right\rangle \approx \quad (1.10)$$

Which leads to the pitch angle diffusion equation:

$$\frac{\partial F}{\partial t} = \frac{1}{\sin \alpha} \frac{\partial}{\partial \alpha} \left\{ \sin \alpha D \frac{\partial F}{\partial \alpha} \right\} \quad (1.11)$$

For the purposes of this work it is now important to consider the dependence of the diffusion coefficient on the wave energy.

The particles have different parallel velocities to the magnetic field which results in different amplitude for the interacting waves implying that the diffusion coefficient depends on the pitch angle. The change in pitch angle can be estimated considering the interaction with waves in a narrow wave-number band Δk around resonance.

From the definition of pitch angle $\alpha = \tan^{-1} \frac{v_{\perp}}{v_{\parallel}}$ comes $\Delta \alpha \approx -\frac{\Delta v_{\parallel}}{v_{\perp}}$

The change in v_{\parallel} is given by the acceleration due to the waves near resonance times the time a particle stays in resonance:

$$\Delta \alpha \approx \frac{ev_{\perp}}{m} \frac{B'}{c} \frac{\Delta t}{v_{\perp}} = |\Omega_c| \frac{B'}{B} \Delta t \quad (1.12)$$

And the diffusion coefficient becomes:

$$D \approx \frac{(\Delta \alpha)^2}{2\Delta t} \approx \frac{|\Omega_c|^2}{2} \left(\frac{B'}{B} \right)^2 \Delta t \quad (1.13)$$

Where B is the magnetic field strength, B' is the wave amplitude and Ω_c is the electron cyclotron frequency. The interval Δt indicates the time a particle at distance $\Delta k/2$ out of resonance changes its phase by 1 radian: $\Delta t \approx 2/\Delta k v_{\parallel}$, and considering that $v_{\parallel} = v \cos \alpha$, the diffusion coefficient can be rewritten as:

$$D \approx |\Omega_c| \frac{(B')^2/\Delta k}{B^2} \frac{|\Omega_c|}{v |\cos \alpha|} \quad (1.14)$$

For small Δk the factor $(B')^2/\Delta k$ is the energy per unit wave number at resonance ($B'_k{}^2$) and $|\Omega_c|/v$ is a typical wave number (k^*) for the whistler mode spectrum, such that the diffusion coefficient is given by:

$$D \approx \frac{|\Omega_c|}{\cos \alpha} k^* \left(\frac{B'}{B} \right)^2 \equiv \frac{D^*}{\cos \alpha} \quad (1.15)$$

When applying this theory to observations in a magnetosphere an important question arises: How to determine from the measurements if the observed particle distribution is unstable to whistler wave emissions and consequently to pitch angle scattering and particle precipitation?

One concept which can be applied is that of critical flux. The critical flux indicates the threshold that the resonant electron flux must exceed in order for the waves to reach significant amplification. This flux is equivalent to the stably trapped flux described by *Kennel and Petschek* (1966). To determine the stably trapped flux the authors balance the wave growth rate γ given by equation 1.4, with the wave escape rate. As can be seen in equation 1.4 the wave growth rate is related to the fraction of electrons in resonance η (equation 1.5). This is an important quantity for the calculation of the stably trapped flux and is therefore related to quantities which are observable, J the omnidirectional flux, V_R the resonant velocity and N the total number density. The quantity $J/V_R N$ has the same dimensions as η and when computed in the weak diffusion limit (which means that the majority of the particles are not within the loss cone) allows the omnidirectional flux J to be obtained.

For non relativistic electrons it is given by $J_c \sim 8 \times 10^{10} (L^{-4}/E)$, where L is the radial distance and E the electron energy (according to *Thorne and Tsurutani* (1979)).

Another important step is to express the diffusion coefficient in terms of wave parameters which are measurable by instruments such as the Plasma Wave Spectrometer on board Galileo (described in Chapter 2). The average diffusion coefficient is given by (according to *Thorne and Tsurutani* (1979)):

$$D_\alpha \sim \frac{2\pi f_c}{\gamma} \cdot \left(\frac{B'}{B}\right)^2 \cdot \epsilon \quad (1.16)$$

Where f_c is the electron gyrofrequency, $(B')^2$ is the fluctuating resonant wave power and B is the ambient magnetic field. In the estimation only non-relativistic electrons were considered and therefore $\gamma \sim 1$. The ϵ parameter defines the scattering region and is given as a fraction of the total length of a field line in the interaction region ($\epsilon \sim 1/10$, e.g., assumes that the scattering region is confined to the center of the plasma sheet).

The resonant wave power $((B')^2)$ can be determined by knowing the electric field wave amplitude, which can be obtained from the wave data, according to $E' = (S \times \Delta f)^{1/2}$ with S being the spectral density (in $V^2/m^2\text{Hz}$), and Δf the bandwidth (in Hz). For nearly parallel propagating whistler-mode waves the magnetic field component of the wave is related to the electric field component by: $B' = \frac{nE'}{c}$, with the refractive index being given by $n^2 = 1 + (f_p/f_c)^2/\nu(1-\nu)$, where $\nu = f/f_c$, f is the wave frequency, f_p the plasma frequency and E' the electric field wave amplitude.

Knowing the different wave parameters, allows the pitch angle diffusion coefficient to be estimated and to establish if this diffusion process is relevant to the region of the magnetosphere studied in this work.

1.6 The Nishida recirculation model

Observations of the Jupiter magnetosphere clearly showed that with the moon Io a major plasma source exists in the inner magnetosphere (as previously discussed in section 1.3). Initially the plasma, which is accumulated in a torus around Jupiter, is electromagnetically accelerated up to the rotational speed of Jupiter (*Krupp et al.* 2004a). It is then transported outwards by centrifugal interchange instability. The transport is done in the direction of decreasing density and therefore the plasma diffuses outward, losing energy. But the

observation in interplanetary space of electrons with very high energies that escape from the Jovian magnetosphere was difficult to understand considering only outward radial diffusion. A global model of particle transport and acceleration in the Jovian magnetosphere was proposed by *Nishida (1976)*, accounting not only for this effect but also explaining observations indicating a pancake distribution in the inner part of the magnetosphere and a bi-directional distribution throughout the middle magnetosphere. The model was further developed by *Fujimoto and Nishida (1990)* as a recirculation model for particle acceleration in the Jovian magnetosphere.

The model consists of four diffusion processes. The first one is inward radial diffusion conserving the first and second adiabatic invariants, the second is the pitch angle diffusion in the inner magnetosphere, the third is latitudinal diffusion occurring at low altitudes which conserves the first but not the second adiabatic invariant and the fourth is the isotropization of pitch angles in the current sheet. A schematic view of the recirculation model can be seen in figure 1.9.

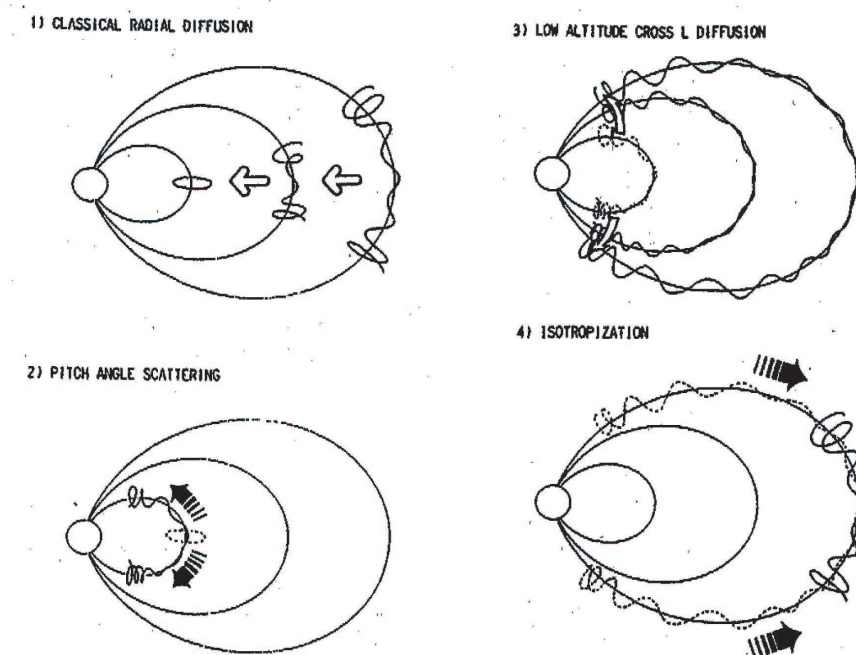


Figure 1.9: Schematic view of the Nishida recirculation model (from *Fujimoto and Nishida (1990)*). Step 1 is the inward radial diffusion; Step 2 is the pitch angle scattering in the inner magnetosphere; Step 3 portrays the low altitude cross L diffusion and step 4 is the pitch angle scattering of particles in the current sheet which brings particle to re-enter the circulation.

As the particles diffuse inwards they are accelerated, their energy is enhanced and their pitch angle increases towards 90° . When they reach distances where the pitch angle anisotropy is sufficient to excite whistler mode waves (as explained in the previous section) the pitch angle diffusion will bring the mirror point of the particles to lower altitudes. In this process some of the particles will precipitate into the ionosphere but a part can also suffer the third type of diffusion (latitudinal) which does not affect their energy and causes them to escape to outer magnetic shells. In the final step of the model the par-

icles undergo pitch angle scattering in the current sheet and reenter the circulation. This model will be of use in the interpretation of the Energetic Particles Detector data whose analysis is described in Chapter 3.

1.7 The Jovian aurorae

In this section the most important features of the Jovian auroral emissions are discussed. They result from the precipitation of particles into the ionosphere of the planet, which through collisional excitation leads to the auroral emissions. As previously discussed pitch angle scattering can lead to particle precipitation. Therefore one observable signature of this process would be the excitation of auroral emissions. A detailed knowledge of the observed auroral features help us to establish which physical processes might generate them, and thus to disentangle the dynamical processes in the magnetospheric source region.

Auroral emission is a common process on planets with strong magnetic fields and an atmosphere. On Earth the extensive knowledge of the aurora is mostly based on decades of ground-based observations. Further insight was obtained by spacecraft observation. The basic structures and sources were identified and it became clear that the solar wind is the driver of the Earth's aurorae (for a review see *Hill (2004)* and references therein). The Jovian aurorae were discovered in the 1950's with the detection of non-thermal radio emissions (*Burke and Franklin 1955*) and observations have only since then been obtained, which explains why many questions still remain open. As at Earth, also a main oval structure was identified, but it was soon understood that the Jovian aurorae were not primarily solar wind driven, but by the planet's rotation. In both cases several wavelengths were observed (x-ray, ultraviolet, infrared, radio) (*Bhardwaj and Gladstone 2000*). In the following section the focus will be on the ultraviolet (UV) emissions observed at Jupiter. These are thought to be produced by electrons, since spectral observations do not provide evidence for proton, sulphur or oxygen ions being a possible source for the emissions.

1.7.1 Spacecraft observations of the Jovian aurorae

The first spacecraft observations of Jupiter's aurorae were made by the Voyager spacecraft in 1979 (*Broadfoot et al. 1979*) at ultraviolet wavelengths (mainly due to the collisional excitation of H_2). These were followed by observations by the International Ultraviolet Explorer (IUE) which greatly contributed to a better understanding of the spatial and temporal variations of the aurorae. They also showed that, contrarily to the Earth's case where the main oval is fixed with respect to the solar wind direction, many of the Jovian auroral features are fixed to Jupiter's magnetic system (System III) and therefore corotate (or partially corotate) with the planet. In the late 1980's near-infrared (IR) thermal emission of H_3^+ was discovered with the Canada-France-Hawaii telescope using high resolution spectra at $2 \mu\text{m}$ wavelength in the southern auroral region (*Drossart et al. 1989*). The IR emissions presented a morphology similar to the UV emissions, although discrete features visible in the UV along the main auroral oval (MAO), could not be distinguished in the IR emissions.

With the development of the Hubble Space Telescope (HST) in the 1990's and its

high resolution images a new era began. Initially the Faint Object Camera (FOC) with a sensitivity limit of 50-100 kR⁵, allowed the identification of the latitude of the main oval, which was traced to distances of $\sim 30 R_J$ using magnetic field models existent at the time. Improved magnetic field models (such as the VIP4 model) later gave a different estimation and the main oval was mapped to distances of $20 R_J$ to $25 R_J$. The FOC images also showed the existence of asymmetries between the dawn and dusk sides of the northern auroral oval. The emissions were seen as distinct arc structures in the morning side while at dusk they were more diffusive.

After correction of the optics for the HST, the Wide Field Planetary Camera 2 (WFPC 2) lowered the sensitivity limit to a range between 2 kR to 10 kR. The high resolution images of both polar regions provided a more detailed distribution of the emissions and due to its consistent detection of the Io footprint they provided valuable input to the development of magnetic field models which resulted in the VIP4 model. No emissions were detected equatorward of the Io footprint and bright emissions ($> 10\text{MR}$) were detected at dawn poleward of the main oval. They were referred to as "dawn storms". Thus three separate regions were identified at the time: The Io footprint, the main auroral oval and the polar emissions. The amazing pictures of the Jovian aurora continued to improve with the Space Telescope Imaging Spectrograph (STIS) whose sensitivity limit was of ~ 1 kR. The observations allowed for the tracking of local time features as well as transient features. Furthermore, emissions from the footprints of Ganymede and Europa were discovered equatorward of the MAO, which clearly indicated that the MAO emissions map to distances greater than $15 R_J$ (Clarke *et al.* 2002) as was also indicated by magnetic field models. With 5 years of observations it became clear that the main auroral oval is fixed in SIII longitude and new reference ovals were defined for both North and South poles.

Recent studies of the Jovian aurora and in particular of the main auroral oval region showed the existence of a secondary oval (as can be seen in figure 1.10), located equatorward of the MAO, with half the brightness of the MAO emissions (Grodent *et al.* 2003). These emissions as well as its source processes are the subject of this work, and will be described in more detail in the following section.

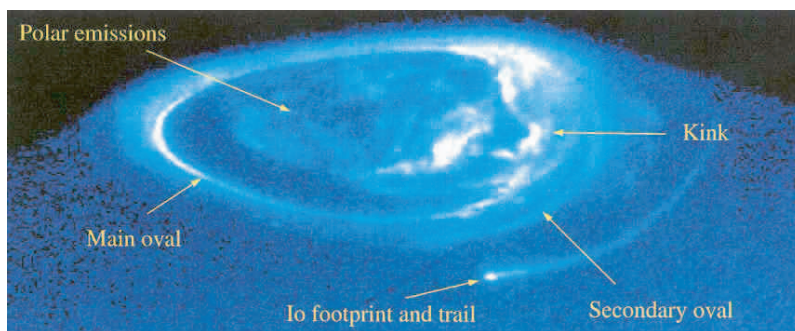


Figure 1.10: HST-STIS image of the FUV northern aurora showing the main and the secondary oval, the Io footprint, the polar emissions and the kink area (Grodent *et al.* 2003).

⁵1 kRayleigh = 10^9 photons/sec from a 1 cm^2 column of atmosphere radiated into 4π steradians. In terms of power 100 kR correspond to an input power of 10 mW/m^2 (Clarke *et al.* 2004).

1.7.2 Characteristics of the Jovian aurorae

Based on locations, physical regions and processes from which they originate and time independent variations, the Jovian aurorae have been divided into 3 regions: the satellite footprints, the main and secondary oval and the polar emissions.

The first satellite emissions identified were those associated with Io (*Connerney et al.* 1993). The emissions were seen around the location of Io's magnetic footprint, and remained fixed to magnetic field tubes connected to the moon. The interaction of Io with Jupiter's magnetic field is of great interest, since it has no counterpart at Earth. Io is a conductive body due to its ionosphere. The motion of the moon through the magnetic field lines results in a current system between Io and Jupiter's ionosphere which leads to the precipitation of charged particles causing UV and IR emissions at the Io footprint. It was also observed that the emissions are not produced exactly along the Io field line, but they are associated with the flux tube threading Io's magnetospheric wake and therefore leading Io by a few degrees relative to its orbital motion (*Clarke et al.* 2004). Study of STIS spatially resolved spectra (*Gérard et al.* 2002) determined the mean energy of the electrons creating the northern UV emissions to be in the range from 55 keV at the Io footprint to 40 keV at 20° downstream in the trail. The emissions of Europa and Ganymede were detected later by *Clarke et al.* (2002). The emissions of Ganymede's footprint are brighter than the ones from Europa's footprint, and both are generally of the order of a few tens of kR. The fact that the footprint of Ganymede is seen equatorward of the main auroral oval further constrained the location of the MAO source region to distances greater than 15 R_J .

The main auroral oval emissions are continuous emissions circumpolar to both poles at latitudes of 85°. They are observed to corotate with the planet at the SIII rotation period. The arcs of the MAO are quite narrow in width, of the order of 100 km to 500 km, and the brightness ranges from 100 kR up to MR intensities. Some of the brighter features, with intensities in the MR range, were observed in the poleward edge of the dawn local time sector, they are referred to as "dawn storms". The dawn storms were observed to be fixed in corotation and to move into the main oval, which implies a process that originates in the outer magnetosphere and propagates towards the middle magnetosphere. Based on this, *Hill* (2001) and *Cowley and Bunce* (2001) suggested that the MAO is associated with the magnetosphere-ionosphere coupling current system related to the breakdown of corotation in the middle magnetosphere. As the plasma is diffusing outwards in the equatorial plane, the angular velocity decreases due to conservation of angular momentum. At a certain point, when the angular velocity of the plasma is below that of the planet, break-down of corotation occurs and a strong current system develops. When the plasma angular velocity becomes lower than that of the neutral atmosphere ion-neutral collisions occur in the Pedersen layer of the ionosphere which produce a frictional torque transmitted to the plasma by the magnetic field, spinning it back to corotation. The associated current system is shown in figure 1.11. Equatorward directed currents are connected to outward radial currents in the equatorial plane via field-aligned (or Birkeland) currents. The torque associated with the $\mathbf{J} \times \mathbf{B}$ force of the Pedersen layer balances the frictional torque of the atmosphere. The associated opposite torque from the equatorial $\mathbf{J} \times \mathbf{B}$ force accelerates the plasma back to corotation. The system of field-aligned currents is closed by currents flowing from the equatorial plane to the ionosphere. It is the system

of upward field-aligned currents (FAC) which are carried by downward moving electrons that is associated with the MAO. The measured electron parameters indicate that in order for the electrons to carry the necessary current, a potential drop of the order of 100 keV is needed to accelerate the electrons giving the precipitation fluxes which produce the observed MAO emissions.

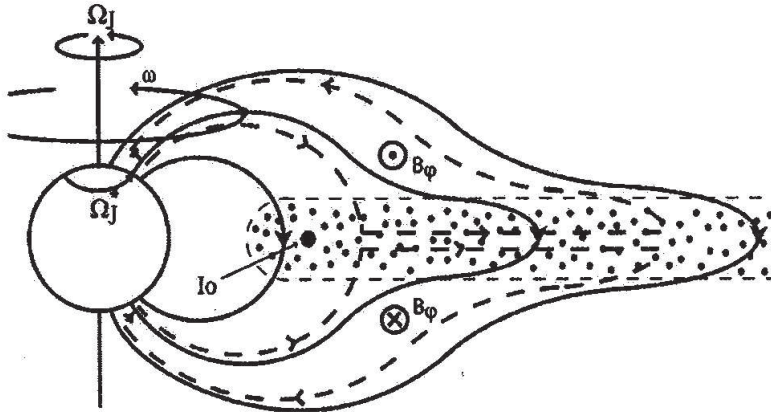


Figure 1.11: Meridian cross through the Jovian magnetosphere showing the field-aligned current system (dotted lines). The dotted region indicates the plasma. Ω_J is the angular velocity of the planet, ω is the angular velocity of a shell of field lines and Ω_P is the angular velocity of the Pedersen layer (Cowley and Bunce 2001).

In the HST images of the northern auroral oval (figure 1.10), a disturbed area known as the "kink" region is seen to corotate with Jupiter. It is assumed at present that the kink region is associated with an anomaly on the surface magnetic field.

The secondary oval was recently identified by Grodent *et al.* (2003) as a discrete belt of emissions seen equatorward of the MAO. These emissions are better seen in individual images. They are more pronounced for system III longitudes of 100° to 180° . In the other regions the emissions are harder to detect due to lower brightness or merging with the main oval. The secondary oval emissions may go up to half the brightness of the MAO emissions and in average they are comparable in brightness to the Io trail at 20° downstream, which means ~ 40 KR. A mean brightness profile through a cut of the northern auroral region of Jupiter, is shown in figure 1.12. The first peak seen is the MAO (pixels 30 to 55) and equatorward of it (pixels 55 to 85) is the secondary oval (D. Grodent, private communication), with a brightness of ~ 50 to 80 kR (The brightness values indicated are the mean brightness). Spectral analysis studies indicate that the secondary oval emissions are generated by electrons with energies from 40 to 200 keV. Because they are seen equatorward of the main auroral oval these emissions must map to regions in the equatorial plane inside $15 R_J$. Up to now the source for these emissions is not known and this work studies a possible explanation for the secondary oval.

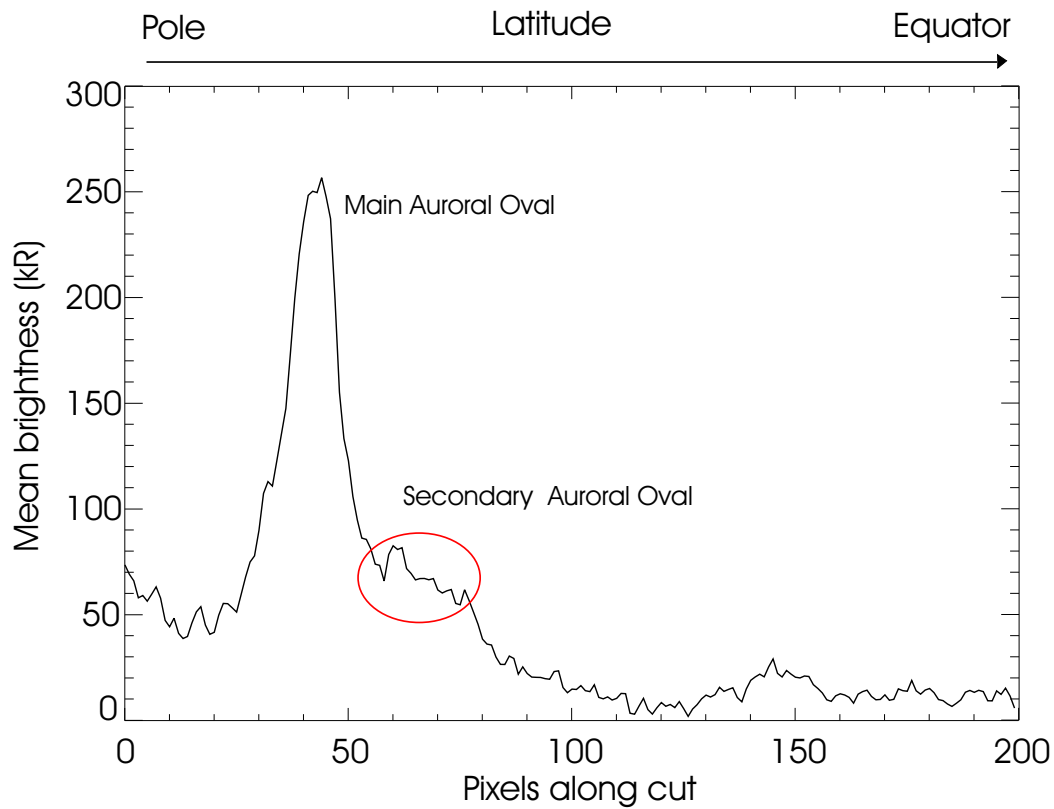


Figure 1.12: . Brightness profile through a cut of the northern auroral region of Jupiter. The x-axis shows the number of pixels starting at 0 (pole) towards the equator. The red oval indicates the location of the secondary oval. (Image courtesy of D. Grodent, Univ. Liège).

1.8 Summary

In this introductory chapter the Jovian magnetosphere was discussed and it was shown that it is a unique system. The observations made by the different missions to the planet revealed a diversity of phenomena which do not have counterparts in the Earth's magnetosphere and it became clear that an Earth-like model of a solar wind driven magnetosphere could not accurately describe the Jovian magnetosphere. The most important factors that make the Jovian magnetosphere a particular case are the presence of the moon Io and the fast rotation of the planet. Io is the most important source of plasma in the Jovian magnetosphere releasing 1 ton/s of sulphur and oxygen ions, and therefore clearly conditions the plasma transport, acceleration and diffusion processes. Of the different particle diffusion processes, the pitch angle diffusion due to whistler wave scattering has particular importance to this work since it can lead directly to auroral emissions. It was also seen that the physical processes at the origin of the secondary oval, which has been recently observed by the HST, are still unknown.

In the following chapters of this thesis the analysis of the Energetic Particles Detector data as a valuable tool to better understand the Jovian particle environment and the physical processes occurring in the magnetosphere will be discussed. The study of the energetic particles characteristics done in this thesis is presented in Chapter 3. The importance of these results to the better understanding of the Jovian aurora and the global particle transport and acceleration mechanisms is discussed in Chapter 4.

2 The Galileo Mission and instrumentation used

In this chapter the Galileo mission is described. In particular the Energetic Particles Detector (EPD), which provided the data at the basis of this work. Due to their contributions to this work the Magnetometer and Plasma Wave Spectrometer are also shortly described.

2.1 The Galileo mission

Launched on 18 of October 1989 the Galileo spacecraft mission was the result of 12 years of careful planning and development followed by 6 years of travel and culminating in nearly 8 years of orbit around Jupiter. This extraordinarily successful mission came to an end in 21 of September 2003, with Galileo disintegrating into the planet's dense atmosphere. The initial ideas for the mission came immediately after the fly-bys of Pioneer and Voyager. The previous missions collected valuable data which revealed a complex planet and magnetosphere in many ways different to what was known from Earth. But the insights provided by the fly-by missions lead the scientific community to question even further, and the need for better time and spatial coverage could only be addressed by an orbiter. The mission received its name from Galileo Galilei the "father" of modern astronomy, which made the first observations of Jupiter in 1610 using a telescope. He discovered four of the Jovian moons, Io, Europa, Ganymede and Callisto, known today as the Galilean moons.

The interplanetary trajectory of the spacecraft was called VEEGA for Venus-Earth-Earth Gravity Assist, a technique used to allow the spacecraft to get the necessary velocity to reach Jupiter traveling for 6 years and a total of 4,631,778,000 kilometers. During the interplanetary travel scientists used the experiments on board to study not only the planets Earth and Venus and the Moon, but also the asteroid belt where Galileo took a close look at two of the asteroids: Gaspra and Ida, and found the first satellite (Dactyl) orbiting an asteroid (Ida). Some interplanetary studies using the dust detector, the magnetometer plasma and particle detectors were also made.

The Galileo spacecraft consisted of two parts: an orbiter and an atmospheric probe. A sketch of the spacecraft can be seen in figure 2.1.

The Galileo orbiter combined features from the previous missions (Pioneer and Voyager) using a dual-spin design which allows one part of the spacecraft to rotate (the antennas and some instrument booms) while another part remains fixed due to a three axis stabilised structure (the instrument platform). The twelve scientific experiments on board the orbiter are the result of an international cooperation. The set of four Remote-sensing

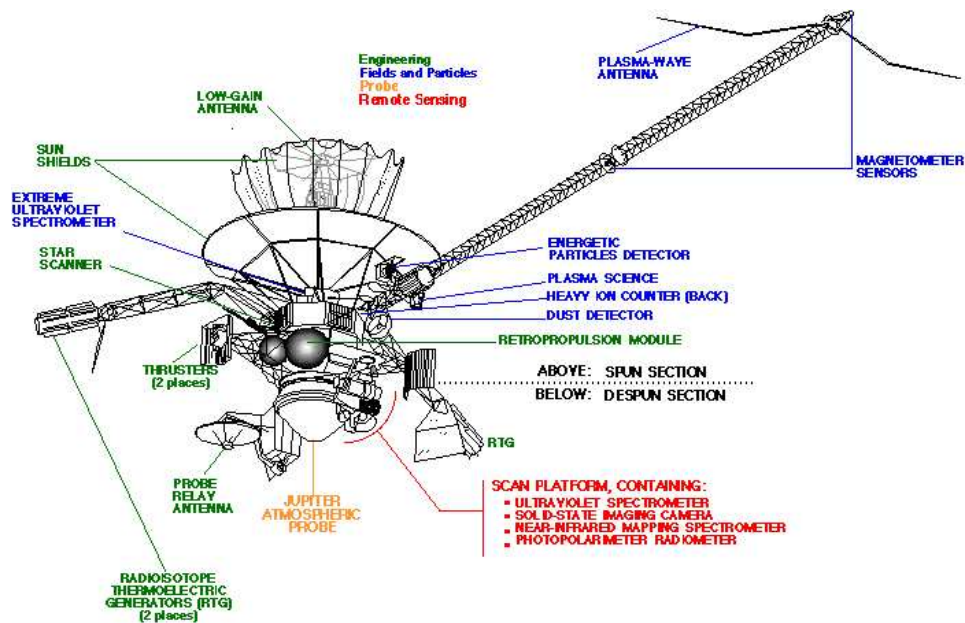


Figure 2.1: Sketch of the Galileo orbiter. Credits: JPL/NASA

instruments covered a wide range of wavelengths, it was focused on Jupiter and its moons, studied the Jovian atmosphere, the surface of the satellites, the sunlight scattered radiation among other subjects. It consisted of the following instruments:

- Photopolarimeter Radiometer (PPR)
- Near-Infrared Mapping Spectrometer (NIMS)
- Solid-State Imaging Camera (SSI)
- Ultraviolet Spectrometer and Extreme Ultraviolet Spectrometer (UVS/EUV)

An Engineering experiment, the Heavy Ion Counter, was included to provide information on the very high energy heavy ions which hit the spacecraft. For Radio Science two experiments were included (Celestial mechanics and Radio propagation) which used the radio system to detect small changes in the trajectory of the spacecraft and also monitored the Jovian neutral atmosphere and ionosphere. A set of five fields and particles instruments was used to study the Jovian magnetosphere. These are:

- Plasma Instrument (PLS)
- Dust Detector Subsystem (DDS)
- Magnetometer (MAG)
- Plasma Wave Subsystem (PWS)
- Energetic Particles Detector (EPD)

The PLS measured the energies and directions of ions and electrons and used a mass spectrometer to identify the composition of ions, the DDS was used to measure the mass, electric charge and velocity of particles with masses from 10^{-6} to 10^{-7} g. The PWS was designed to measure the properties of varying electric and magnetic fields, and to identify the waves present. The MAG was designed to measure the components of the magnetic field and the EPD measured energies and flux of electrons and ions.

This work is mainly based on the EPD data set, with significant contributions from the MAG and PWS data. The working principles and the main scientific objectives of these 3 instruments are detailed in the following section (a list of the instruments and its principle investigators is given in Appendix B).

The orbit of Galileo allowed the spacecraft to encounter the Galilean satellites in different occasions and therefore each orbit receives the name based on the satellite encountered and the number of the orbit (e.g. C3 means encounter with Callisto on orbit 3, this will be the notation used in this work). The closest approach to Jupiter occurred during the final orbit which encountered Amalthea at a distance of $2.5 R_J$ and the spacecraft covered a wide area of the magnetosphere reaching distances of $150 R_J$.

The main scientific objectives of the Galileo orbiter were divided into three major groups, the Jovian atmosphere, the Galilean satellites and the Jovian magnetosphere. Some of the most important scientific key studies were:

- Investigation of the circulation and dynamics of the Jovian atmosphere;
- Investigation of the upper atmosphere and ionosphere;
- Characterisation of morphology, geology and physical state of the Galilean satellites;
- Study of the composition and distribution of surface materials of the satellites;
- Characterisation of the gravitational and magnetic field of the Galilean satellites;
- Characterisation of the vector magnetic field;
- Study and characterisation of the particle distribution in terms of energy spectra, composition, angular distribution and dynamics.

2.2 The EPD instrument

On board the Galileo spacecraft was the Energetic Particles Detector (EPD) an instrument designed to measure the characteristics of the Jovian charged particle population, in terms of composition, intensities, energies and angular distributions. With this instrument it was possible to enlarge the energy and angular coverage, relative to previous missions, being a major contribution to the advance of our knowledge of the Jovian magnetosphere. The EPD instrument was built in a joint effort between the Max-Planck-Institut für Sonnensystemforschung (MPS) (former Max-Planck-Institut für Aeronomie, MP Ae) and the Johns Hopkins University Applied Physics Laboratory (JHU/APL). Some of the characteristics of the instrument are given in table 2.1. A complete description is given by *Williams et*

al. (1992). It consists of two double-headed detector systems, the composition measurement system (CMS), where different ions (protons, Helium, Oxygen and Sulphur) are separated in a time-of-flight detector system and a so-called $\Delta E \times E$, and the low energy magnetospheric measurement system (LEMMS) where ions and electrons are separated by an internal permanent magnet. The detectors will be discussed in more detail below. A sketch of the instrument with both detectors is shown in figure 2.2. One of the important innovations of the instrument is the capability to provide 4π steradian angular coverage. This is achieved by conjugating the rotation of the spacecraft with the rotation of the instrument, which is mounted on a turntable rotated by a stepper motor perpendicular to the s/c axis (see figure 2.3). In this way, the measurements are independent of spacecraft orientation and magnetic field direction.

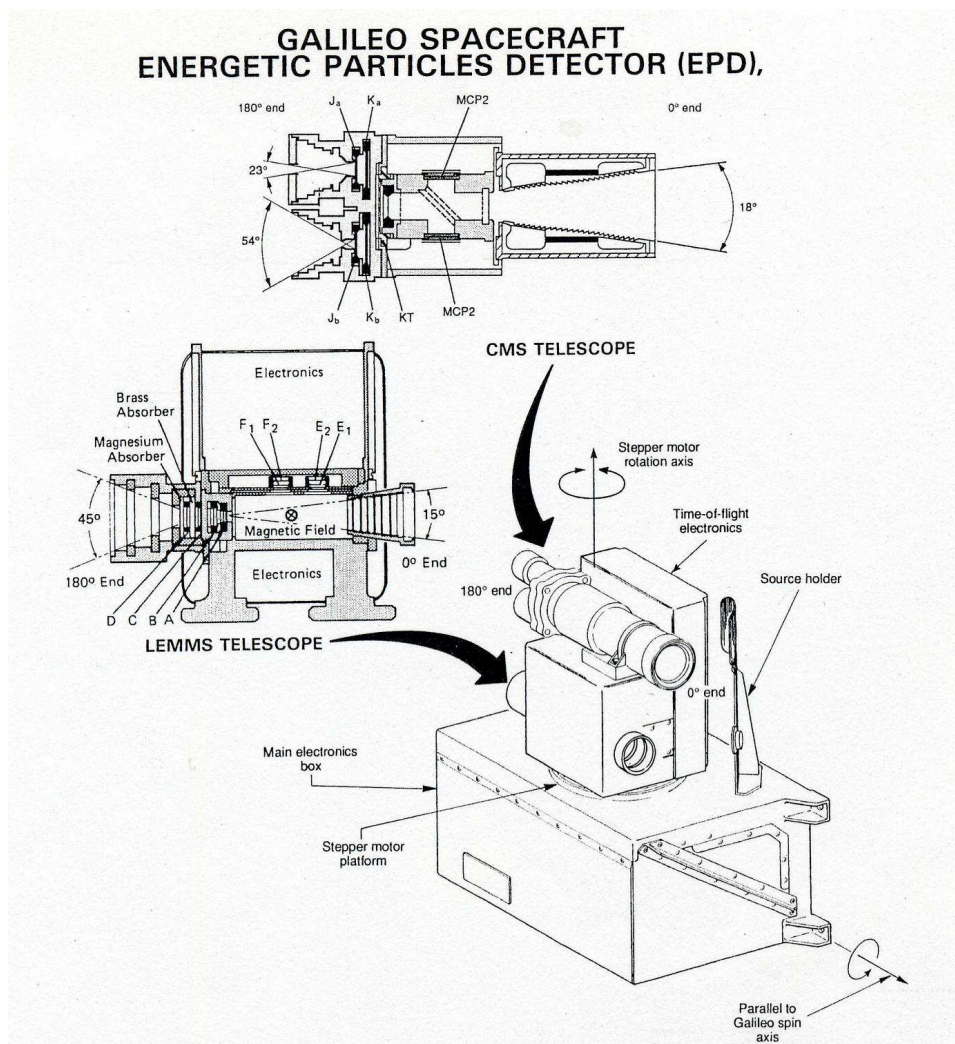


Figure 2.2: Sketch of the Energetic Particle Detector, showing the LEMMS and CMS telescopes.

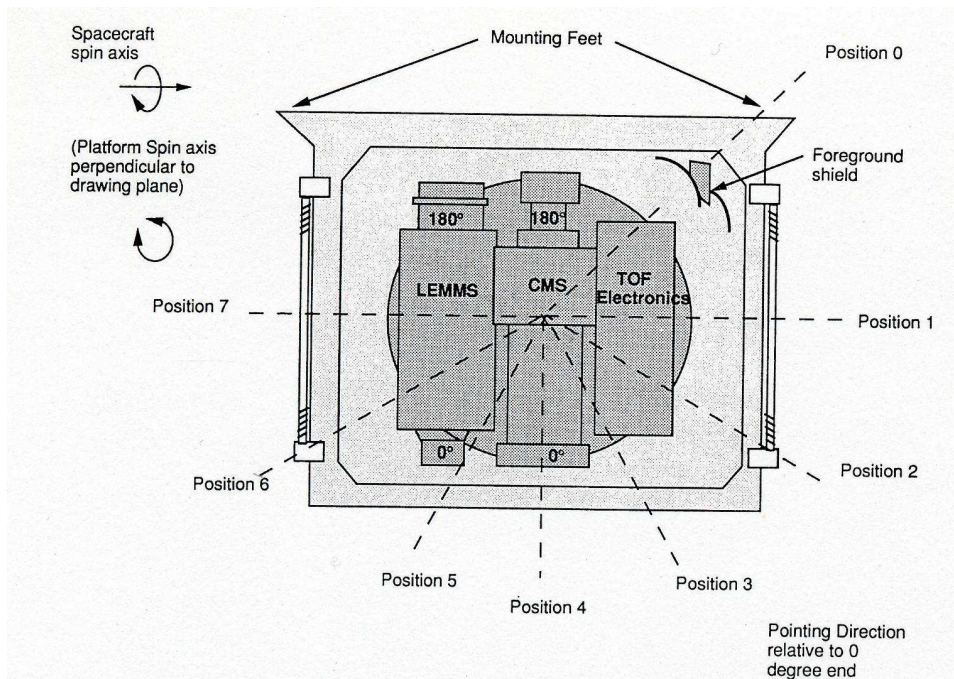


Figure 2.3: View of the EPD instrument, looking down along the stepper motor rotation axis and showing the EPD viewing positions.

The Galileo spacecraft was prepared to transmit data at two different rates. High resolution data, from a high gain antenna would be transmitted at a rate of 134 kbps, and low resolution data, from a low gain antenna, at a rate of 160 bps. Due to problems in unfolding the high gain antenna shortly after launch, only the low gain antenna could be used during the entire mission. This led to a rearrangement of the data measured by EPD which was then transmitted in two different modes, real time and record mode data. Some of the characteristics of these two modes are seen in table 2.2. The spatial, time and angular resolution obtained in each mode are a combination of the spacecraft spin and the different stepper motor positions. The motor can move through 8 positions which are 30° apart, except for position 0 that differs 45° from position 1.

The record mode data has a transmission rate of 912 bps and achieves the highest time and angular resolution. This mode was the originally planned mode. It was mainly used during the encounters with the Galilean satellites using the onboard tape recorder and transmitting the data with the low gain antenna at low bit rates. In this mode the rotation of the spacecraft is divided in 16, 32 and 64 spin sectors, and using the seven positions of the step motor a resolution of 448 data points in the unit sphere can be achieved. The maximal time resolution is achieved by dividing the *s/c* rotation period of 20 seconds by the number of sectors (16,32 or 64).

The real time data is available during most of the mission and is therefore the basis of the work developed in this thesis. In this mode the tape recorder is not used and the EPD has transmission rates of 5, 10, 15, 20, 30 or 40 bps and only 7 of the 8 motor positions are covered once every *s/c* spin. The time resolution is ~ 11 minutes and the maximal number of sectors is 16 (1 and 6 sector measurements are also available). A more detailed discussion can be found in *Lagg (1998)*. Of particular importance to this

Mass	10.5 Kg
Dimensions	19.5cm × 27 cm × 36.1 cm
Power	6 W electronics: 4 W heaters

Table 2.1: EPD Characteristics

	Record mode	Real-time mode
Bit rate (bps)	912	5-40
Time resolution	33-1.3 s	3-11 min
Sampling	52-420 samples	16 samples

Table 2.2: Record and Real time mode characteristics

work is the calculation of the pitch angle distribution from the 16 sector measurements, in which the data from 16 different directions of the unit sphere is sampled within 3 to 11 minutes. The angular resolution of each sector in this mode is 45° . Assuming that the measured fluxes represent fluxes from the sector centres, the pitch angle is calculated for each orientation during the measurement cycle. Combining several cycles and assuming stationary conditions a reasonable coverage and resolution for the pitch angle distribution can be achieved.

2.2.1 Low Energy Magnetospheric Measurement System (LEMMS)

The LEMMS is a double headed telescope consisting of eight silicon solid-state detectors, measuring electrons and ions in low to medium energies. It provides a high angular ($> 20^\circ$) and temporal (1/3 s to 4/3 s) resolution. In figure 2.4, both the electron and ion detectors of the LEMMS can be seen.

Particles entering the telescope at the 0° end, pass through a collimator and are separated using magnetic deflection. The magnetic deflection method uses the effect of the Lorentz force on the incoming particles. The electrons will be deviated by the force, in a direction perpendicular to both the magnetic field and the instantaneous velocity. This will not change the kinetic energy or speed of the particle (since the magnetic field does not do work on the particle), but can change the direction of the velocity.

By this process the electrons are deflected upwards, into the solid-state detectors E and F, being divided into 8 energy channels between 15 keV and 884 keV. The ions, due to their opposite charge and higher masses, are slightly deflected in the opposite direction and registered by detectors A and B in 8 energy channels, between 22 keV and 12 400 keV. The LEMMS ion and electron channels are summarised in tables 2.3 and 2.4. The C and D detectors at the 180° end provide measurements of ions and electrons with higher energy ranges, $\gtrsim 14.5$ MeV and $\gtrsim 51$ MeV for ions, and two integrated channels for electrons of $\gtrsim 2$ MeV and $\gtrsim 11$ MeV.

In order to convert the counts per second (cps) detected into differential flux ($\text{cm}^{-2}\text{s}^{-1}\text{sr}^{-1}\text{keV}^{-1}$), it is necessary to have a precise knowledge of the geometric factor of the detectors. Simulations were done by *Lagg* (1998), which allowed to determine the geometric factor for both electrons and protons as a function of energy. In combination with

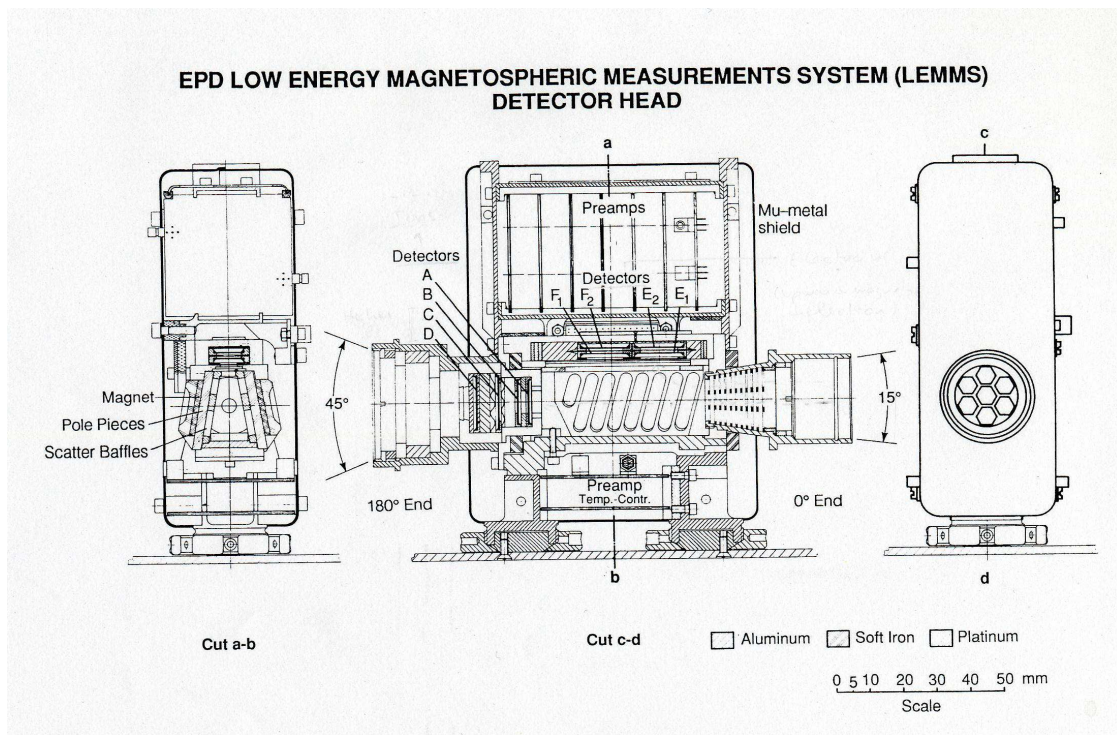


Figure 2.4: Cross-section of the LEMMS telescope. Detectors A and B measure ions, detectors E and F measure electrons and detectors C and D measure high energy electrons and ions.

the knowledge that the fluxes can be described by a power law distribution $J(E) \propto E^{-\gamma}$ a calculation was made of the geometric factor per energy channel. In this way the differential flux of the LEMMS electron channels is calculated, as the number of particles hitting the detectors per cm^2 , per steradian, per second and per energy/nucleon.

Low-Energy Ion Telescope: Detectors A and B

The low energy ion population ($\gtrsim 22$ keV) of the Jovian magnetosphere is measured by detectors A and B. Ions entering the collimator pass through eleven baffle plates defining seven hexagonal entrance aperture channels which converge towards detector A. In the field region the ions are little deflected and its counts are registered by detector A.

Detectors A and B have areas of 25 mm^2 and 35 mm^2 , with a surface barrier of 102μ and 984μ thickness, respectively.

The ions ($Z \gtrsim 1$) are divided into 8 differential rate channels in the energy range from 22 keV to 3 200 keV (see table 2.3). Higher energies and $Z \gtrsim 2$ channels are obtained by using coincidence logic between A and B.

A thick platinum-iridium shield of $\gtrsim 12 \text{ g cm}^{-2}$ thickness and coincidence/anticoincidence conditions minimise the background contamination.

Low-Energy electrons: Detectors E1, E2, F1, F2

In the LEMMS telescope an inhomogeneous magnetic field is generated by a permanent magnet with a maximum centre line strength of 650 G. The entering electrons are de-

Channel	Energy Range (keV)
A0	22-42
A1	42-65
A2	65-120
A3	120-280
A4	280-515
A5	515-825
A6	825-1680
A7	1680-3200

Table 2.3: Energy range of the LEMMS ions channels

Channel	Energy Range (keV)
E0	15-29
E1	29-42
E2	42-55
E3	55-93
F0	93-188
F1	174-304
F2	304-527
F3	527-884

Table 2.4: Energy range of the LEMMS electrons channels

flected into detectors E1 (for $\gtrsim 15$ keV to 200 keV) and F1 (~ 100 keV to > 1000 keV).

Detectors E1 and F1 have an area of 45 mm^2 and a surface barrier of 303μ and 1097μ thickness, respectively. Detectors E2 and F2 (of 300μ thickness and equal area) operate in anticoincidence to reduce background effects on the surrounding platinum-iridium shielding of $\gtrsim 6 \text{ gcm}^{-2}$.

The electrons measured in E1 and F1 are divided into 8 rate channels, in the energy range from 15 keV to 884 keV, as indicated in table 2.4. Channel F0 provides the sum of the electrons between 100 keV and 200 keV, which are seen by both detectors.

An additional correction is considered for the lower energy channels, which due to the high count rate close to the planet, are eventually saturated. This correction is based on laboratory calibration measurements where the input rate is measured versus the output rate of the particles at the detector (r vs. r correction).

High Energy Electrons and Ions: Detectors C and D

Detectors C and D have $\sim 100 \text{ mm}^2$ and a thickness of $\sim 300 \mu$. They measure electrons and ions in the highest energy range detected by LEMMS.

The detectors have two thresholds, of $> 2 \text{ MeV}$ and $> 11 \text{ MeV}$ for electrons, and of 14.5 MeV and 51 MeV for ions (in detectors D and C respectively).

2.2.2 The Composition Measurement System (CMS)

The CMS measures the ion composition in the Jovian magnetosphere from energies of $10 \gtrsim \text{keV nuc}^{-1}$ to $> 10 \text{ MeV nuc}^{-1}$. Two different energetic particle telescopes incorporate the CMS. The time-of-flight (TOF) and a pair of $\Delta E \times E$ solid state detectors. The telescopes are oriented in different directions, the TOF looks on the 0° end while the $\Delta E \times E$, which covers higher energies, looks in the 180° direction. Electrons are prevented from entering the system by a magnet present in the collimator.

In the TOF telescope the ions will hit a parylene foil releasing the starting electrons which are detected at the Start-MCP (microchannel plate) using an electrostatic mirror. The electrons are then accelerated by an electric field and are stopped in the K_T detector. In this detector their energy is measured and more electrons are emitted which are stopped in the Stop-MCP. From the energy measured in the K_T detector and from the time difference between the start and stop signals, the mass of the ions can be obtained. In the $\Delta E \times E$ detector system, two set of detectors are present. One measures the dissipated energy and the other the remaining total energy. Knowing this values as well as the thickness of the detector and the speed of the particle allows to determine their atomic number (Lagg 1998).

The CMS channels have a time resolution of $4/3 \text{ s}$ except for some of the channels which are read every $8/3 \text{ s}$. A detail of the detector can be seen in figure 2.5.

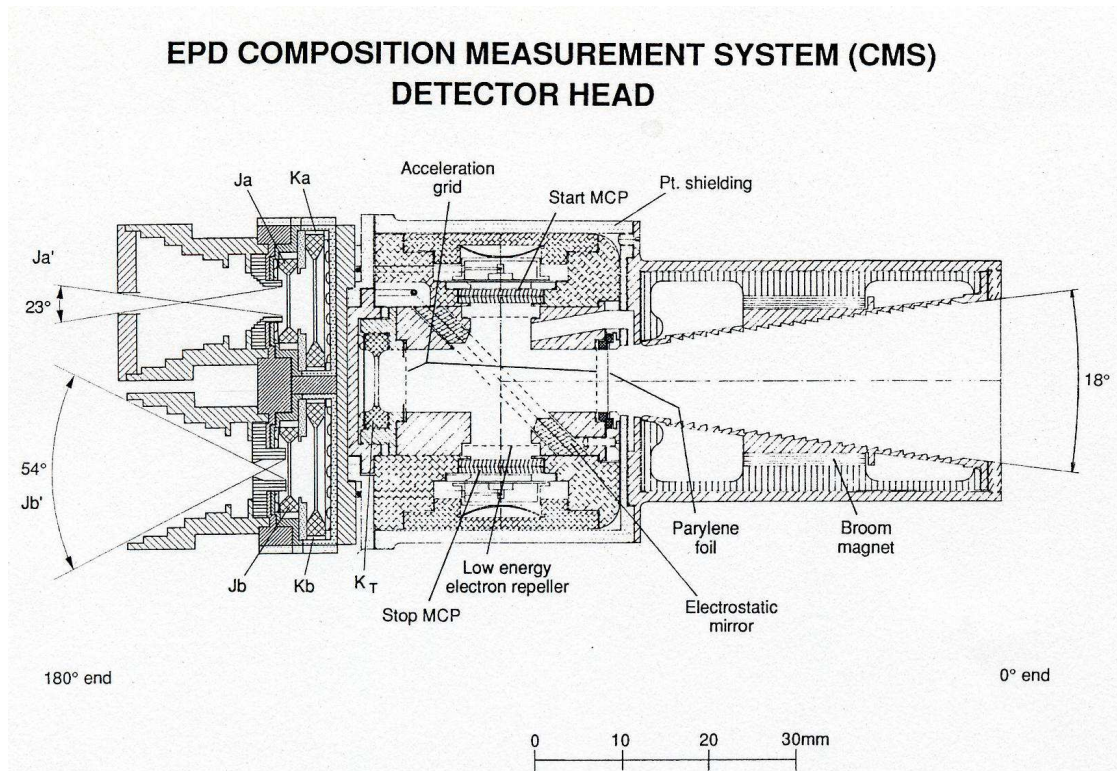


Figure 2.5: Detail of the CMS detector.

In the CMS ions are separated into different species and energy ranges. The TOF gives measurements for Protons divided into three channels between 80 keV and 1250

keV, Helium is divided into two channels (27 keV/nuc and 1000 keV/nuc), three Oxygen channels (26 keV/nuc and 562 keV/nuc), three Sulfur channels (16 keV/nuc and 310 keV/nuc) and one heavy nuclei channel (20 keV/nuc to 200 keV/nuc). The $\Delta E \times E$ detectors give measurements in higher energy ranges, Helium is divided in three channels (19 keV/nuc to 1400 keV/nuc), four oxygen channels (16 keV to 10 700 keV), two intermediate nuclei (1000 keV/nuc to 11 700 keV/nuc) and four heavy nuclei (22 keV/nuc to 15 000 keV/nuc).

2.3 The Magnetometer

The magnetometer (MAG) on board Galileo gives high resolution measurements of the Jovian magnetic field in a broad range, covering low values typical for the Solar Wind (~ 0.1 nT to 1 nT) to very high values expected closer to the planet ($\sim 6 \times 10^3$ nT), allowing for analysis of the configuration and dynamics of the Jovian magnetosphere.

The time resolution of the retrieved data varies. For very high time resolution the data is recorded on the tape recorder every 0.33 s/vector, and transmitted afterwards at lower rates. When the data are directly transmitted, one magnetic field vector is sent every 24 s.

The instrument consists of two triaxial fluxgate magnetometers mounted on a long boom at 11.03 m and 6.87 m from the S/C spin axis. This allows to isolate the sensors from the magnetic fields generated by the S/C. A full description of the instrument can be found in *Kivelson et al.* (1992).

One of the important functions of the magnetometer is to provide the reference direction which together with the energetic particle measurement gives the possibility to construct the pitch angle distribution of the charged particles, essential in the development of this work.

2.4 The Plasma Wave Spectrometer (PWS)

With the Plasma Wave Spectrometer plasma waves and radio emissions in the Jovian magnetosphere can be studied. This is of great importance in determining the dynamics of the Jovian magnetosphere since wave particle interactions cause pitch angle scattering and loss of energetic particles. The close flybys of the Galilean moons in particular of Io also allows to better understand plasma energisation and the consequent plasma wave phenomena.

The PWS instrument provides spectrograms in the frequency range from 5.6 Hz to 5.65 kHz, on a variable time scale between 30 minutes and 24 hours.

The instrument consists of an electric dipole antenna (mounted at the end of the magnetometer boom) and two search coil magnetic antennas (mounted on the high gain antenna feed). The instrument is fully described in *Gurnett et al.* (1992).

2.5 The coordinate system

The most relevant coordinate system used in this work is the Jovian System III (1965).

In this system z is the rotation axis and x defines $\lambda_{III}=0^\circ$. This is a left handed rotation system, with longitude being measured clockwise from the zero longitude meridian.

Another relevant system is the Jovian Magnetic system III. It is based on the magnetic axis of Jupiter, which is tilted 9.6° in relation to Jupiter's rotation axis. The z axis is the magnetic dipole axis and the x axis is given by $\lambda_{III}=201.7^\circ$. This can be better seen in figure 2.6, which shows the coordinates for the Jovian SIII (A), and the Jovian magnetic system III (B).

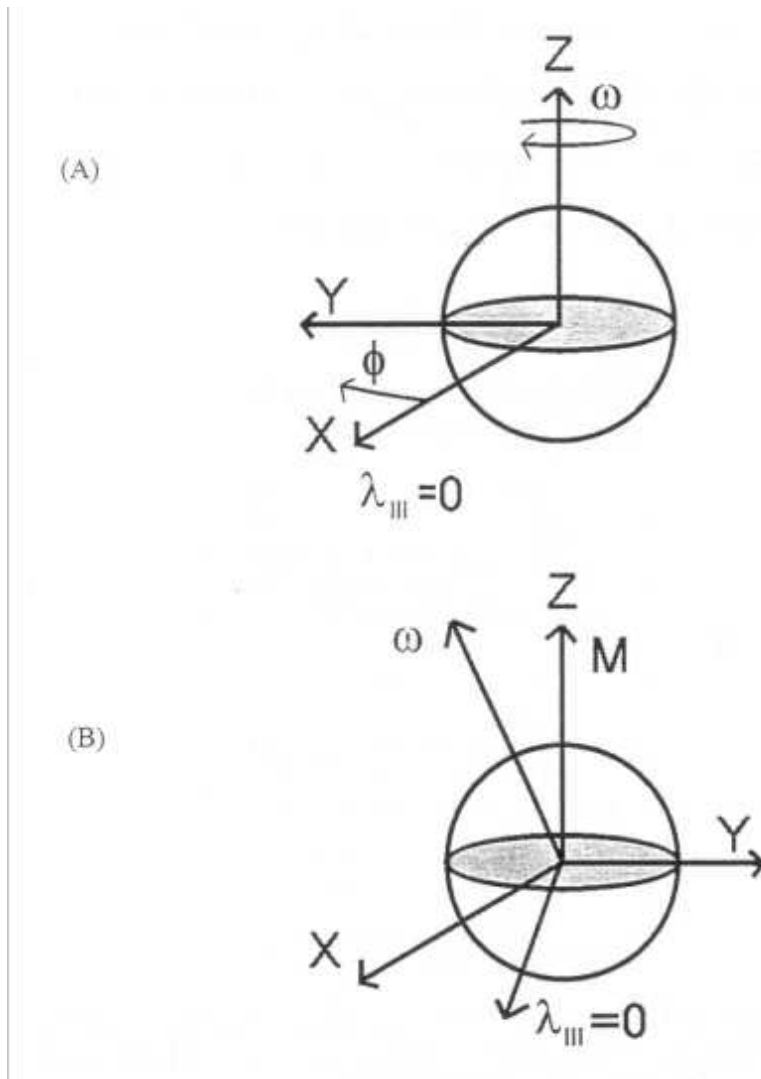


Figure 2.6: Jupiter coordinate Systems. (A)- Jovian System III, the z axis is the rotation axis; (B)- Jovian magnetic system III, the z axis is the magnetic dipole axis.

3 Energetic particle and magnetic field observations

The orbits of the Galileo spacecraft covered a wide range of the Jovian magnetosphere as seen in figure 3.1, and crossed a variety of regions, starting at the orbit of Io ($6 R_J$) in the inner magnetosphere, through the current sheet region and magnetotail, up to distances of $150 R_J$. The excellent coverage in radial distances is complemented by a reasonable coverage of the different local time sectors. In this work the region of the magnetosphere within $40 R_J$ of Jupiter was studied, based on 33 of the Galileo orbits. It is a region of particular interest where the characteristics of the overall morphology of the Jovian magnetosphere distinctively change. It is in this region that the magnetic field configuration changes from a close to dipolar in the inner part to the characteristic current sheet topology in the middle magnetosphere.

How do the particles react to the change in magnetic field configuration? Is there a correlation? Do the fluxes of the particles, their angular distribution or energy spectrum vary significantly throughout the regions, and how? Do ions and electrons exhibit similar behaviour? What are the characteristic scales for particle changes?

Some of these questions were addressed by previous spacecraft. During the fly-bys of Pioneer and Voyager, a change in the particle characteristics as the spacecraft moved from the middle to the inner magnetosphere was observed. An increase in the fluxes of both medium energetic electrons and ions, and also a hardening of their energy spectra close to the planet was reported by *Krimigis et al.* (1981). Other results indicated that the variations of the spectral index for high-energy oxygen (4.2 MeV to 14 MeV) did not show large variations in the region from $10 R_J$ to $25 R_J$ (*Vogt et al.* 1979). An important result was the observation of bi-directional pitch angle distributions, for both electrons and protons, in the regions from $10 R_J$ to $20 R_J$, while closer to the planet the pitch angle distributions have a maximum at 90° as reported by *Goertz and Thomsen* (1979). At this time bi-directional distributions were not established beyond $25 R_J$. Later Ulysses measurements on high southern latitudes in the dusk magnetosphere, identified field-aligned electron beams at distances from $14 R_J$ to $80 R_J$, in the energy range from 100 keV to 380 keV (*Lanzerotti et al.* 1992, *Seidel et al.* 1997).

In the work of *Goertz and Thomsen* (1979), the authors presented possible explanations for the change in the pitch angle distributions. Adiabatic radial outward diffusion would change an injected isotropic distribution at $12 R_J$ to a more bi-directional distribution along the field. Another possibility is the existence of a loss process acting preferentially at large pitch angle particles, leading to a more bi-directional distribution. But the most appealing idea, was the existence of a local source of small pitch angle parti-

cles in the middle magnetosphere. The distribution was also interpreted in terms of the Nishida recirculation model, which invokes conservation of the first and second adiabatic invariants as the particles diffuse inwards, and therefore increase their pitch angle. This model was described in detail in Chapter 1.

Since the previous missions only provided snapshots of the Jovian magnetosphere, it was only possible to have a localised knowledge of the particle characteristics and spatial or temporal variations were impossible to disentangle. Questions still remained about the global dynamics, are these variations persistent features, do they occur for all local time sectors and in which radial ranges? Are there local time or longitude asymmetries present?

With the excellent coverage of Galileo these questions can be answered in a more detailed and precise way. The clues provided by the fly-by missions can now be confirmed or questioned, and a more complete and detailed picture will emerge. The work presented in this thesis is the first comprehensive topological study of changes in the energetic particle characteristics from the inner to the middle magnetosphere. The study was made for both electrons and ions and considered the variations in the particles flux, energy-time spectrograms, energy spectral index, pitch angle distribution and magnetic field as seen by the Energetic Particles Detector (EPD) and magnetometer (MAG) onboard Galileo.

In the following sections the characteristic energetic particle parameters for one of the orbits analysed will be discussed in detail.

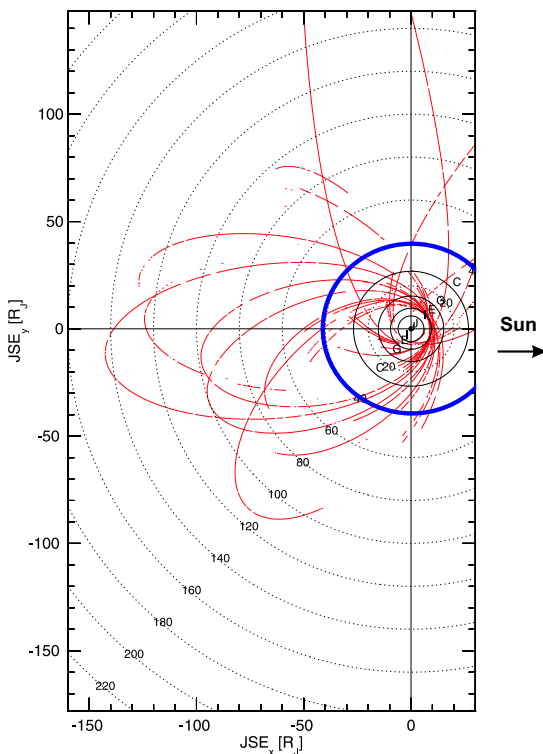


Figure 3.1: Galileo's orbits in the $x - y$ plane of the JSE coordinate system. The incomplete lines indicate the data gaps in the EPD coverage. The blue circle encloses the region within $40 R_J$, being studied in this work.

3.1 Energetic particle and magnetic field characteristics in the Jovian magnetosphere inside 40 R_J - A case study

3.1.1 Particle Flux and Energy-time spectrogram

For a detailed discussion orbit C10 was selected, mainly because of a nearly complete data coverage in the relevant region. The orbital segment shown in figure 3.2 covers 9 days in 1997 (days 257 to 266). The radial range extends to 40 R_J , which for this orbit corresponds to a local time range from 03:30h inbound to 21:30h outbound. The spacecraft approached the planet from the pre-dawn sector and proceeded to the dusk sector, with the closest approach to Jupiter occurring at a radial distance of 9 R_J and a local time of 12:50 h.

First the 1 hour averaged differential fluxes of ions and electrons, from all the energy channels of the LEMMS detector, and the correspondent energy-time spectrograms were analysed. The energy ranges of the different channels are indicated in Tables 2.3 and 2.4.

Two regimes can be identified due to their distinctively different properties. An outer regime (OR), furthest from the planet, and an inner regime (IR) close to the planet which are connected by a transition region (TR). These regions are indicated by the labels and by the colored bars on top of the figure, with the yellow bar for the outer regime, the red bar for the transition region and the blue bar for the inner regime. The overlapping regions indicate the uncertainty in localising the boundaries.

(1) In the outer regime, the flux shows large amplitude oscillations, which are caused by the tilted plasma/current sheet rotating past the spacecraft. This is the "core plasma sheet" regime. During a maximum of the particle intensity the spacecraft is closest to the centre of the current sheet where the particles are concentrated, during minimum the spacecraft is far away from the current sheet centre, in the lobes of the magnetosphere. Since Galileo was close to the equatorial plane of the planet the peaks occurred twice per planetary rotation at intervals of approximately 5 hours. Five hours maximum are seen in the dawn and the dusk. The minimum are more pronounced at dawn than dusk, indicative of a thinner current sheet in the dawn sector opposed to a thick current sheet in the dusk sector. The oscillations are also clearly visible in the energy-time spectrograms.

(2) In the inner "dipolar" regime, the maximum in the oscillations remain, but the minimum are less pronounced. Close to the planet the particle fluxes have increased by more than one order of magnitude, reaching a maximum of $10^4 \text{ cm}^{-2}\text{s}^{-1}\text{sr}^{-1}\text{keV}^{-1}$ for ions and $10^5 \text{ cm}^{-2}\text{s}^{-1}\text{sr}^{-1}\text{keV}^{-1}$ for electrons, at lower energies.

(3) The transition region from the "core plasma sheet" to the "dipolar" region is characterised by a fading of the oscillations and by the simultaneous increase in the intensities. The transition occurs approximately over a 14 R_J range for the inbound pass (dawn sector, from 10 R_J to 24 R_J) and for a 10 R_J range in the outbound pass (dusk sector, from 10 R_J to 20 R_J).

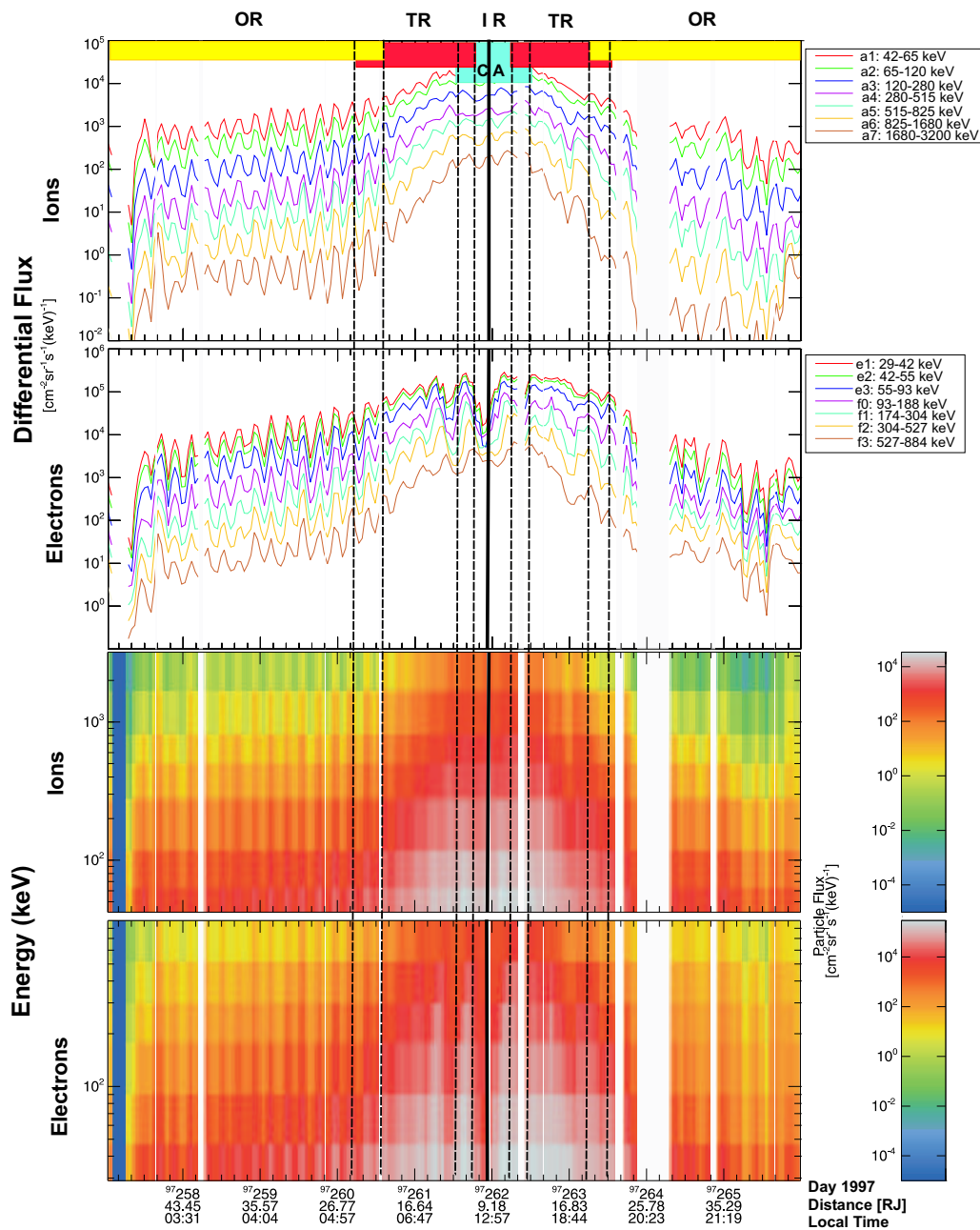


Figure 3.2: Characteristic differential particle flux and energy-time spectrograms during the C10 orbit in September to November 1997, days 257 to 266. The closest approach (CA) to the planet occurs at around $9 R_J$. The first two panels show the ion flux in the energy ranges from 42 keV to 3200 keV and the electron flux in the energy range 29 keV to 884 keV. The last two panels show the energy-time spectrograms for ions and electrons, in the same energy range. The colour code indicates the measured differential particle flux. Time, distance to the planet and local time are indicated at the bottom. Labels and colour bars indicate the different regions: OR (yellow) - Outer regime; TR (red) - Transition region; IR (blue) - Inner regime. The vertical dashed lines indicate the boundaries between the regions.

3.1.2 Magnetic field

The use of the terms "dipolar" for the inner regime and "core plasma sheet" for the outer regime are better understood by analysing the magnetic field data. Figure 3.3 shows the different magnetic field components (B_ϕ , B_θ and B_r), the total magnetic field (B_{total}) and the ratio of the radial (B_r) and north-south (B_θ) components for the section of the C10 orbit considered in the particle analysis. For reference the particle boundaries are indicated by the vertical dashed lines. The characteristic oscillation, due to the tilt of the current sheet is visible as well as the crossings of the current sheet, when the radial component reverses sign.

For a more complete analysis, the ratio of the radial (B_r) and north-south (B_θ) components explicitly shows the change in the magnetic field topology. In the dipolar region, the ratio is small, indicating that the north-south component is dominant. In the core plasma region, the ratio significantly increases, since the north-south component decreases considerably. The transition is gradual and occurs over an extended radial range, which extends up to the outer boundary, as given by the particle observations. Only at radial distances beyond $25 R_J$ does the current sheet signature become evident, as indicated by the spike-like increases or decreases.

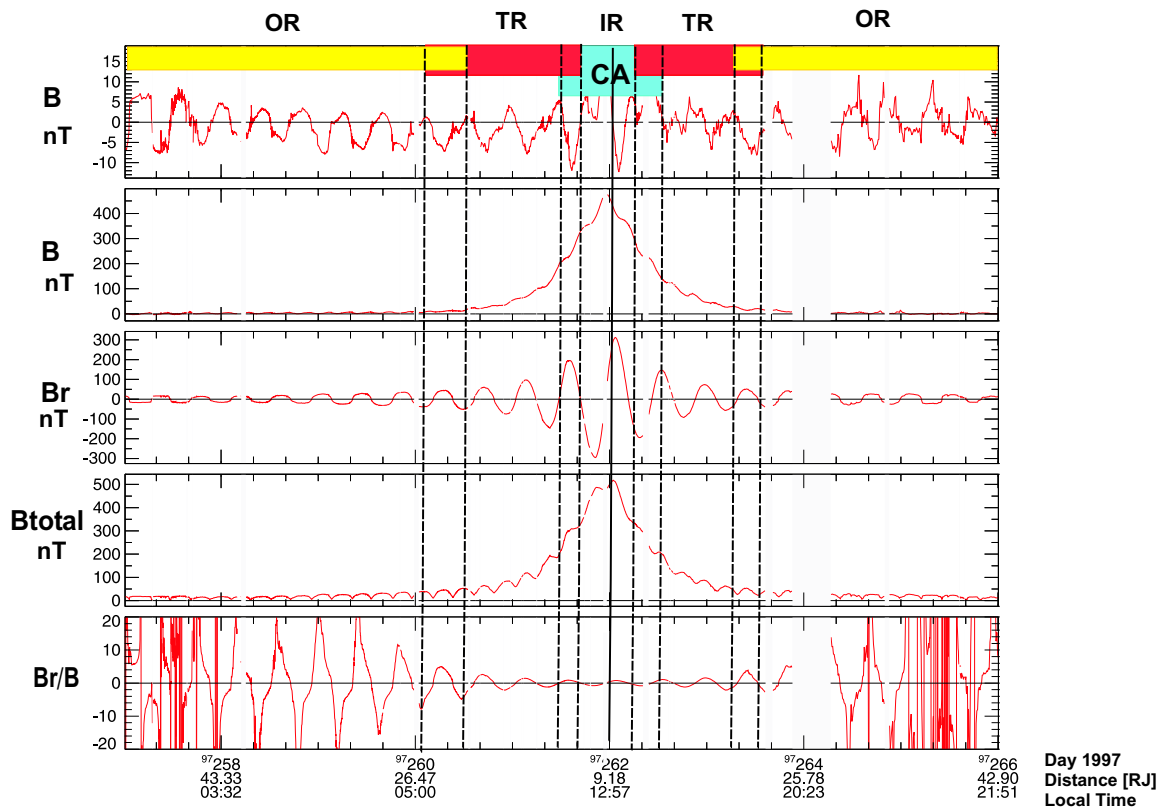


Figure 3.3: Characteristic magnetic field behaviour in the $40 R_J$ range of the C10 orbit. The first 4 panels show the magnetic field components and the total magnetic field (B_θ , B_r and B_{total} respectively). The last panel shows the ratio of the radial and the north-south components. Vertical dashed lines indicate the particle boundaries.

Figure 3.4 compares the evolution of the electron pitch angle distribution with that of the ratio of the radial and north-south components of the magnetic field. It shows that the pitch angle boundary (PAD) is not collocated with the onset of the current sheet produced distortion in the magnetic field.

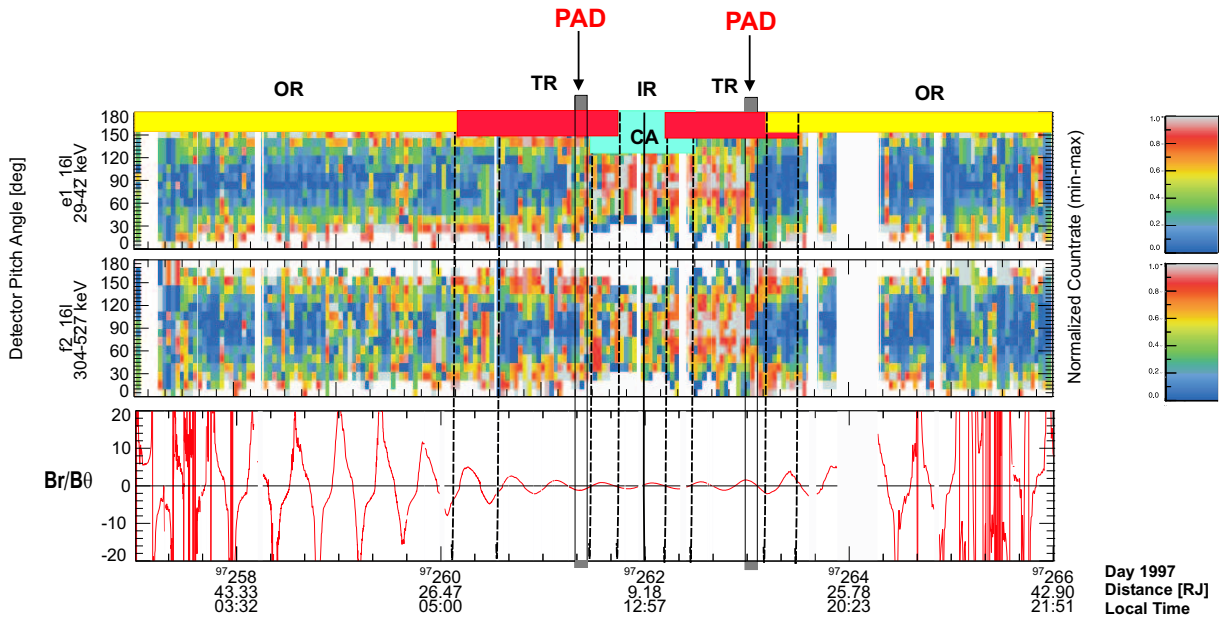


Figure 3.4: Electron pitch angle distribution of two energy ranges (29-42 keV and 304-527 keV). The colour code indicates the particle flux. The lower panel shows the ratio of the radial and the north-south components. Vertical dashed lines, indicate the particle boundaries. Labels and color bars identify the different regions.

3.1.3 Energy Spectral Index

The spectral index γ of the particles is determined by assuming a power law for the energy distribution in the EPD energy range : $J \propto E^{-\gamma}$, with J being the particle flux and E the energy. In the analysis γ was derived separately for electrons, and each of the ion species. The derivation of the spectral index is done by considering the fluxes of two adjacent energy channels, as seen in figure 3.5. Knowing the variations in intensity and energy (ΔJ and ΔE), the spectral index γ as the slope of the spectra, can be calculated. In this work the spectral index for protons (in the energy range 80 keV/nuc to 540 keV/nuc), sulphur (16 keV/nuc to 62 keV/nuc), oxygen (26 keV/nuc to 112 keV/nuc) and electrons (174 keV to 527 keV) were studied. The results are averaged over 10 hours which eliminates the variations due to the planetary rotation. The results are shown in figure 3.6.

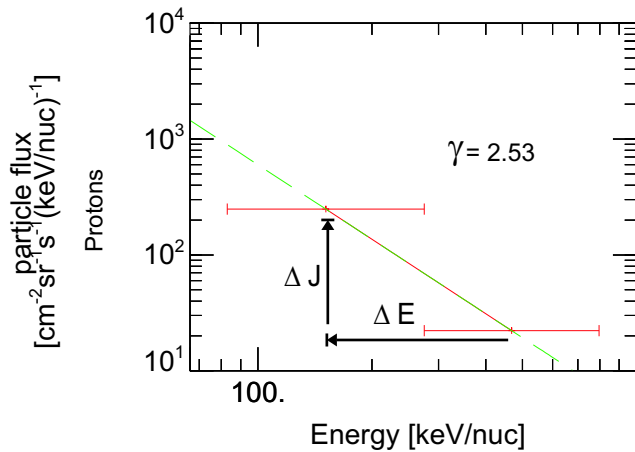


Figure 3.5: Energy Spectra of two adjacent proton channels, tp1 and tp2. The spectral index (γ) is given by the slope of the spectra.

The changes in spectral slope are particularly pronounced for protons, sulphur and oxygen, which show similar profiles. They are seen on all the orbits. The two different regimes are clearly visible and are identified by the color bars and labels as in figure 3.2. For this particular example the following characteristics are observed:

(1) In the outer regime the spectral index of protons and sulphur shows small variations in the dawn sector, between 1.8 to 2.7 and 2.1 to 3.1, respectively. The higher values of the spectral index indicate a soft spectra, with a higher fraction of low energy particles present. In the dusk sector the variations are slightly larger, with the spectral index reaching higher values, indicating that the fraction of low energy particles present in this area is higher. The spectral index for oxygen also shows a bigger variation on the dusk sector, between 2.5 to 3.9, while in the dawn sector a nearly constant level of 2.5 is present with the exception of a transient increase in the spectral index between days 259-260. The spectral index for electrons shows the same trend as those for the ions species, although more variations occur throughout this region, for both dawn and dusk. The outer boundary is located at $24 R_J$ inbound and $20 R_J$ outbound.

(2) In the inner regime, the spectral index is at a much lower level, with γ between 1.2 and 1.5, for protons, sulphur and oxygen. A low value of the spectral index indicates a hard spectra, with a higher fraction of high energy particles present. In this example the inner boundary is roughly located at $10 R_J$ for the inbound pass (dawn sector), and at $11 R_J$ for the outbound pass (dusk sector).

(3) The transition region between these two regimes, shows the hardening of the spectral index as the spacecraft moves closer to the planet which portrays the increase in the fraction of high energy particles present.

While the small variations of the spectral index within the different regions is specific of the orbit, in general the time profiles for the other orbits considered in this work, are similar and exhibit the same trend. The outer regions have high spectral index at an approximately constant level between 2 and 3, which decreases in the inner region to a nearly constant level of the order of 1.5.

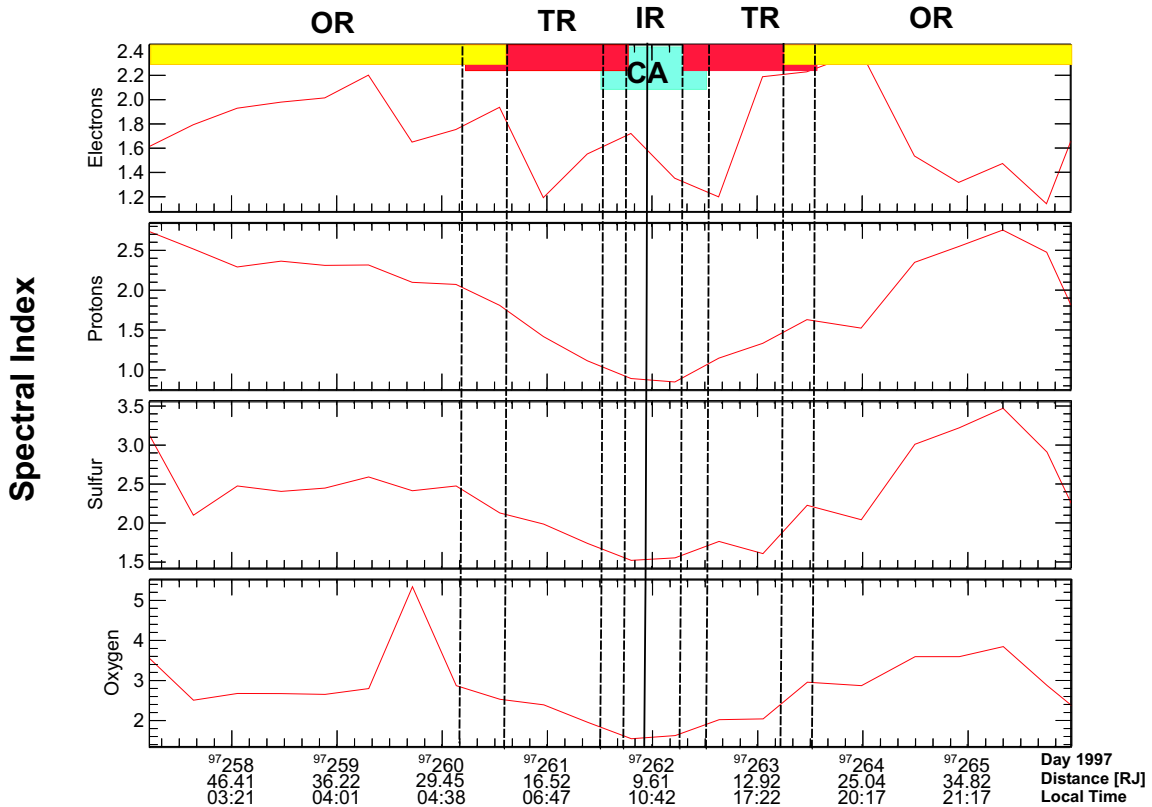


Figure 3.6: Characteristic spectral index profiles for electrons (174 keV to 527 keV), protons (80 keV to 540 keV), sulphur (16 keV/nuc to 62 keV/nuc) and oxygen (26 keV/nuc to 112 keV/nuc). Average over 10 h. The dipolar-like region is indicated by the blue bar and the core plasma sheet region is indicated by the yellow bar. The transition between the two regions is shown by the red bar.

The hardening of the energy spectra is further illustrated in figure 3.7. The energy spectra of protons (left panel) and sulphur (right panel) from the outer region (in yellow) and from the inner region (in blue) with the respective fits are shown. The fluxes decrease from the inner to the outer region as expected, but as can be seen this decrease is more pronounced for the high energy particles, which results in the softening of the spectra.

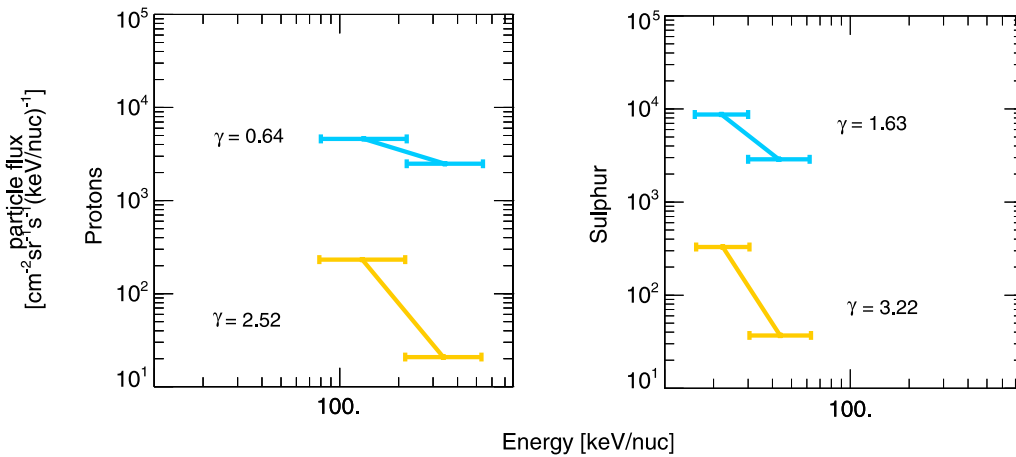


Figure 3.7: Energy spectra of protons (left panel) and sulphur (right panel) for two distinct regions of the magnetosphere, during the outbound pass of the C10 orbit. The yellow line indicates the outer region (at 35 R_J and a local time of 21:20h) and the blue line refers to the inner region (at 9 R_J and a local time of 13:10h).

3.1.4 Pitch angle distribution

Figure 3.8 shows the pitch angle distribution for electrons in two energy intervals (29 keV to 42 keV and 304 keV to 527 keV). In this work the 16 sector measurements of the real-time mode (previously described in Chapter 2) are studied. The data are averaged over 1 hour. The distribution is normalized to the maximum and minimum values in the selected time period, with the color code indicating the normalized electron fluxes. The different regions as observed by the variations in intensities and spectral index of both ions and electrons are indicated by the color bars at the top and the vertical lines.

The electron pitch angle distribution (PAD) shows a well defined boundary between a trapped particle (or pancake) distribution, which maximises at 90° and a more bi-directional distribution which maximises at pitch angles greater and respectively smaller than 90° , for both energy channels. In figure 3.8 this boundary is identified by the grey bar and labeled PAD. In this particular case the PAD boundaries are localised at 11 R_J inbound and 16 R_J outbound. Figure 3.8 also confirms that the boundary in the electron pitch angle distribution occurs for a wide range of electron energies and is roughly collocated with the inner boundaries determined from the spectral index and intensities variation. In the electron pitch angle distribution there is no clear outer boundary visible, with the distribution remaining field-aligned through the outer region.

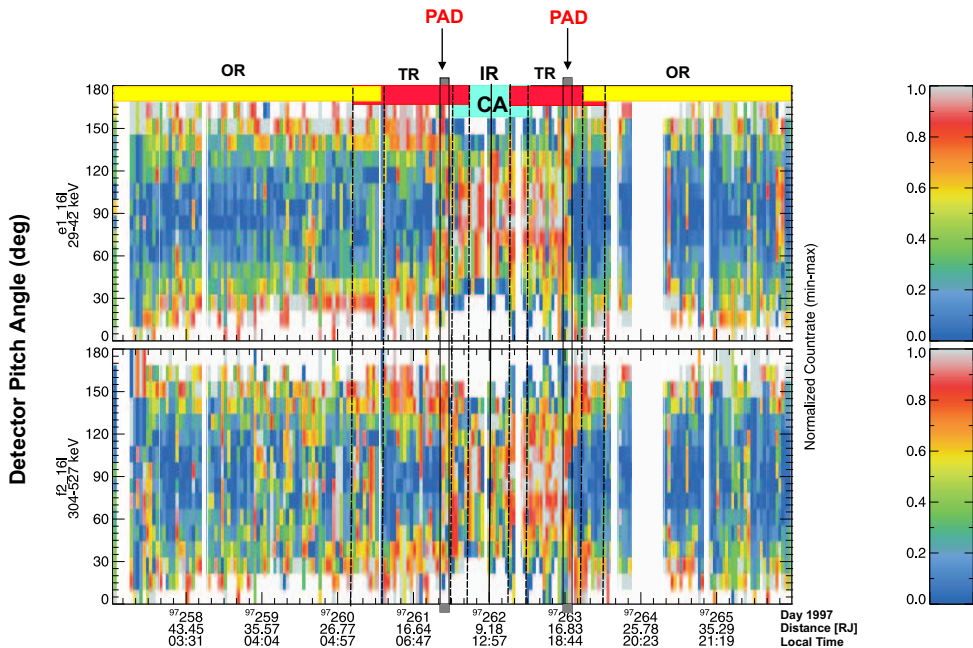


Figure 3.8: Normalised electron pitch angle distribution for two energy ranges (29-42 keV and 304-527 keV). The colour code indicates the particle flux. The average is 1h. The vertical lines and color bars indicate the different regions from the spectral index and particle intensity variations. The grey bars indicate the pitch angle distribution boundary.

This transition is further illustrated in figure 3.9, where two pitch angle distributions representative of the core plasma region and the dipolar region are shown. In the dipolar region, at a radial distance of $11.4 R_J$ the pitch angle of the electrons maximises at 90° and in the core plasma region, at a radial distance of $29.7 R_J$ the distribution indicates that the flux maximises close to the parallel or anti-parallel direction to the magnetic field (field-aligned electron fluxes). Although a clear distinction between a butterfly distribution which maximises at intermediate pitch angles (e.g. at 45° or 135°) and a bi-directional distribution is not possible based on the low resolution real time data, studies based on intervals with high resolution data indicate that the distributions are clearly bi-directional and therefore it is inferred that the observed distributions are in fact field-aligned distributions. The analysis of high resolution data (referred to as record mode data), which were only available for short periods of time during encounters with the moons, will be addressed in section 3.2.

Pitch angle distributions of ions and protons are shown in figure 3.10. The figure shows the pitch angle distribution of two ion (a1: 42-65 keV and a2: 65-120 keV) and two proton channels (tp1: 80-220 keV/nuc and tp2: 220-540 keV/nuc). It is evident that the ion pitch angle distributions do not show so clearly the transition from a pancake to a bi-directional distribution. An interesting phenomena is observed for the low energy channels which show a depletion of particles with 90° at distances of $9 R_J$, while the proton fluxes at higher energies (higher than 220 keV) show a maximum for 90° pitch angle. This effect was studied by *Lagg et al.* (2003), which suggested that the existence of a neutral gas torus surrounding Jupiter in the vicinity of Europa's orbit would cause charge exchange collisions responsible for the observed depletion.

3.1 Energetic particle and magnetic field characteristics in the Jovian magnetosphere inside $40 R_J$ - A case study

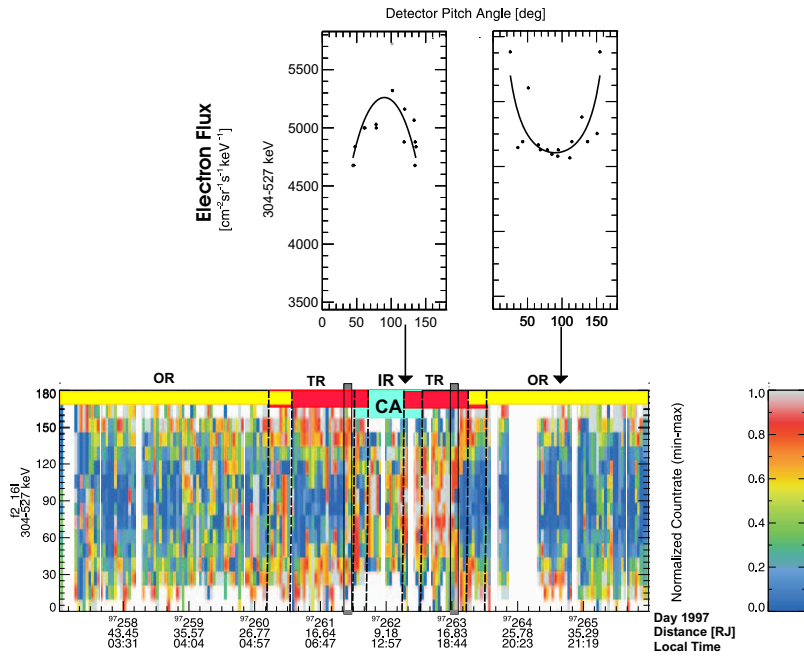


Figure 3.9: Electron pitch angle distribution in two different regions of the magnetosphere (upper panels), with respect to the normalized PAD of electrons in the same energy range 304 keV to 527 keV (Lower panel). The left panel refers to the dipolar region (at $11.4 R_J$ and a local time 16:25h); The right panel indicates the plasma sheet region (at $29.7 R_J$ and a local time of 20:50h). The colour bars and labels identify the different regions.

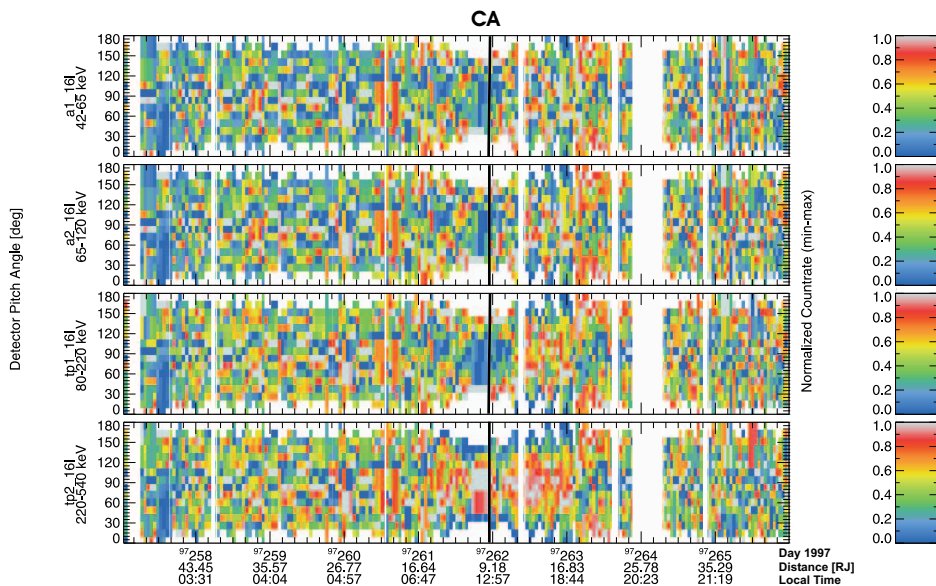


Figure 3.10: Characteristic normalised ion and proton pitch angle distributions. The energy ranges are: a1: 42-65 keV; a2: 65-120 keV; tp1: 80-220 keV/nuc and tp2: 220-540 keV/nuc. The colour code indicates the particle flux. The average is 1h.

3.1.5 Further examples

Another example of the global changes of the energetic particle characteristics for the G7 orbit, days 1997 090 to 1997 098, is presented. Figure 3.11 shows energetic particle observations and magnetic field measurements for this time period, covering distances closer than $40 R_J$ to the planet around perijove. The spacecraft approached the planet from the dawn sector and left through the dusk sector, with the closest approach occurring at around $10 R_J$ at postnoon. The first four panels show energetic ion parameters (ion intensity of four selected channels, energy time spectrograms, using 1-h averages, energy spectral slope γ for protons, averaged over 10 h; and normalised PAD for a selected proton channel). The next four panels show electron parameters in the same format. The magnetic field parameters are shown in the last three panels. They display the total magnetic field, the ratio between the radial and the north-south component, and the radial component of the field (in red) compared with the O6 internal field model (in blue) (for a description of the model see Appendix D) as well as the residual field (in black). The two regimes (dipolar and core plasma regime) previously identified are clearly visible in this example and are identified by the color bars at the top of the spectral index panel. In yellow is the core plasma region, in red the transition region and in blue the dipolar region. The dotted lines indicate the boundaries between the different regimes and the grey bars mark the PAD boundary for the electrons. In this particular example the inner boundary of the transition region is located at about $11 R_J$ on the inbound pass (dawn sector) and at $12 R_J$ on the outbound pass (dusk sector), the outer boundary at about $21 R_J$ inbound and $18 R_J$ outbound. The PAD boundaries as given by the electron pitch angle distribution are located at $12 R_J$ inbound and $15.6 R_J$ outbound.

The magnetic field data clearly shows that in the inner region the internal dipole field dominates, since the residual between the measured data and the modelled values is small. Further out the ratio between the radial and north-south components of the field is changing, showing that the magnetic field topology is changing, with the current sheet becoming more important. The transition from the dipolar region to the core plasma sheet region is gradual and occurs over a radial range extending up to the outer boundary. From this example it becomes clear that the PAD boundary is the most distinct and pronounced boundary in the energetic particle characteristics, in this region of the magnetosphere.

To further illustrate the distinctiveness and persistency of the electron pitch angle change, electron pitch angle distributions of one energy channel (29 keV to 42 keV) are presented for five orbits. Figure 3.12 shows, from top to bottom, the electron pitch angle distribution inside the $40 R_J$ range of the orbits G7, G8, C21 and G28. It is obvious that the pitch angle boundary is seen on the different orbits and for different local times. Orbits C21 and G28 show a data gap which does not allow to precisely locate the PAD boundary. The PAD boundary on orbit G28 could not be determined because the distribution on the dawn side does not show a clear transition to a bi-directional distribution.

The change in the electron pitch angle distribution is the most pronounced and distinct boundary observed in the Galileo measurements in the $40 R_J$ radial range of the Jovian magnetosphere. The processes at this boundary as well as possible consequences for the dynamics of the magnetosphere and relation to auroral features are further investigated in Chapter 4.

3.1 Energetic particle and magnetic field characteristics in the Jovian magnetosphere inside 40 R_J - A case study

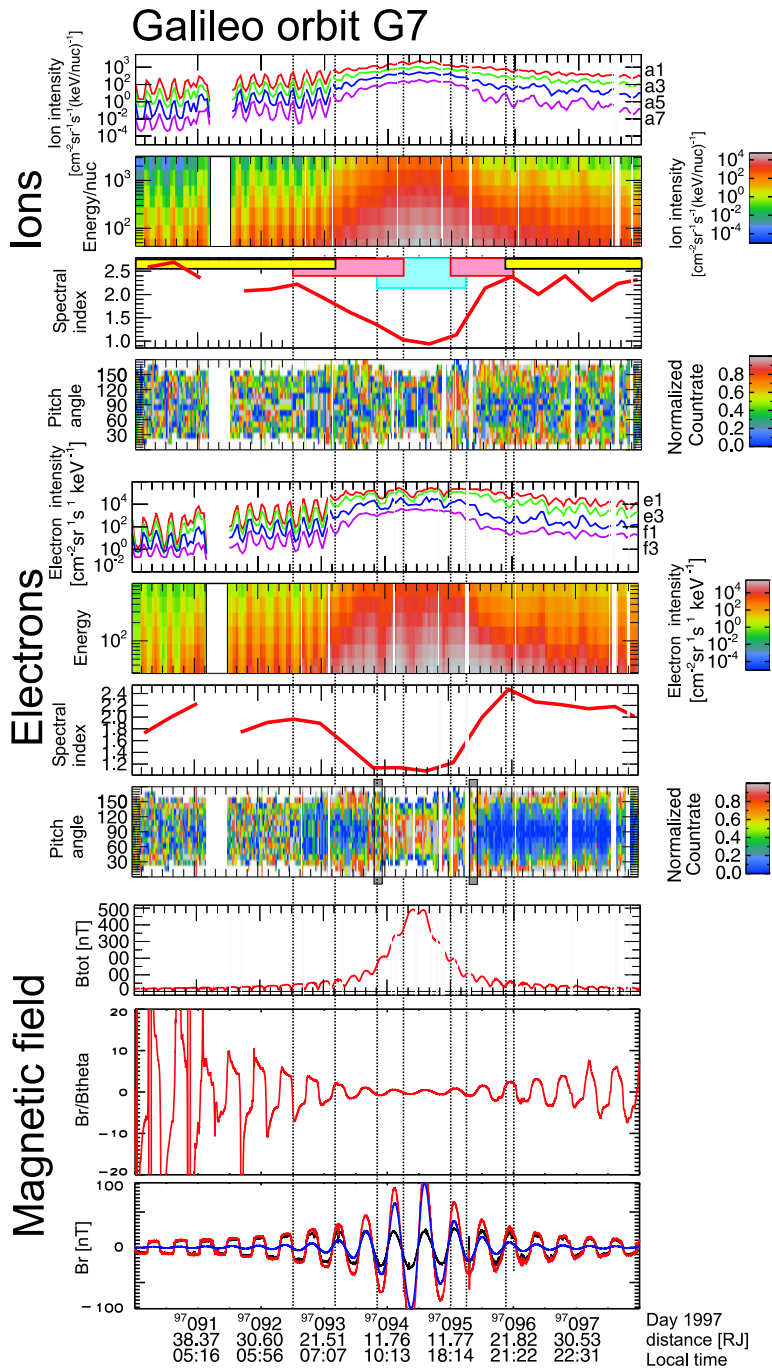


Figure 3.11: Characteristic parameters of the energetic particles and magnetic field components during orbit G7 in April 1997, days 90 to 98. The closest approach to the planet occurs at around 10 R_J at postnoon. The first 4 panels show energetic ion parameters (ion intensity at four selected energy channels, energy-time spectrograms, 1-h averages, energy spectra slope for protons, calculated from 10-h averages, and normalised pitch angle distribution for a proton channel in the energy range 80-220 keV, 30-min averages). The next four panels show electron parameters in the same format (with the electron PAD in the energy range 304-527 keV). The total magnetic field magnitude, the ratio between radial and north-south components, and the measured radial component (red) compared with the O6 internal field model (blue) and the residual (black) are shown at the bottom panels. Time, distance to the planet and local time are indicated at the bottom. Bars and vertical lines indicate various particle regimes and the boundaries. Adapted from *Tomás et al.* (2004a).

3 Energetic particle and magnetic field observations

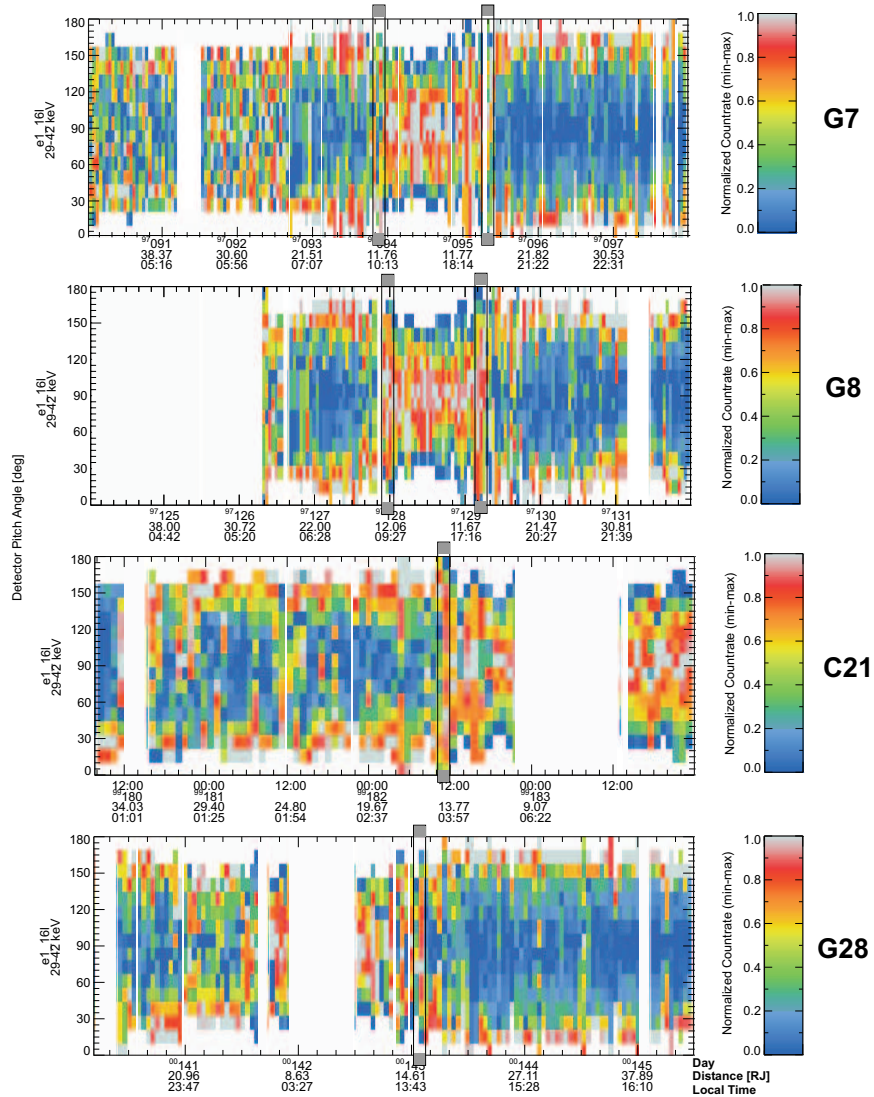


Figure 3.12: Normalised pitch angle distribution of electrons in the energy range 29-42 keV, for 4 different orbits: G7(days 1997 090 to 1997 098), G8 (days 1997 124 to 1997 132), C21 (days 1999 160 to 1999 131) and G28 (days 2000 141 to 2000 145) orbits (from top to bottom) inside $40 R_J$. The colour code gives the particle flux. The average is 1h. Vertical lines and color bars indicate the different regions from the spectral index and particle intensity variations. The grey bars mark the pitch angle distribution boundary.

3.1.6 Location of the boundaries

Using a variety of particle parameters it was possible to identify the location of two boundaries in local time and radial distance on the majority of the 33 orbits where particle parameters change. In figure 3.13 the projection of the particle boundaries into the $x - y$ plane of the JSE coordinate system are shown. In this coordinate system Jupiter is in the centre, x points towards the sun and y towards dusk. The crosses denote the inner boundary (in red) and outer boundary (in blue) of the transition region derived by changes in the ions spectral index. The green triangles denote the sharp boundary in the electron pitch angle distribution. The best coverage for the outer boundary is obtained between 5:00 and 8:00 LT on the dawn sector and 18:00 to 21:00 LT on the dusk sector. For other local time sectors the coverage is sparse.

For most of the orbits the electron pitch angle boundary is closely collocated with the inner boundary of the transition region as observed by the ion spectral index change. The outer boundary is located between $20 R_J$ and $30 R_J$ on the dawn side and between $18 R_J$ and $25 R_J$ on the dusk side. The few boundary locations at other local times are consistent with the location at dawn and dusk. The inner boundary is well covered through essentially all local times, except for the pre-midnight sector. It is located at around $10 R_J$ with a clear tendency for smaller distances around noon compared to dawn and dusk. An asymmetry between dawn and dusk is not obvious.

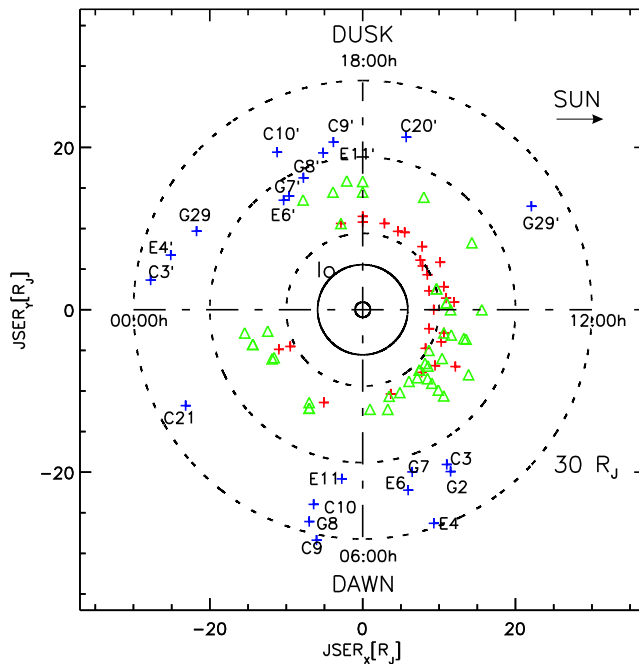


Figure 3.13: Equatorial map of the transition region. The outer boundary, given by the ions spectral index is indicated by the blue +; the inner boundary is indicated by the red + (given by the ions spectral index). Green \triangle show the location of the electron PAD boundary. The dotted circles indicate the distance in Jovian radii (10 , 20 and $30 R_J$) and the solid line indicates the orbit of Io. The labels indicate the correspondent orbits with primed labels referring to post perijove passages.

3.2 Complementary analysis

As previously discussed in the Chapter 2, the high gain antenna which would have allowed to obtain the high resolution data, throughout the entire mission, failed to deploy. The only possibility to obtain high resolution (record mode) data, was to use the tape on board before being sent to Earth. This procedure was used for short periods of time and primarily during encounters with the Galilean moons. A list of the orbits and respective dates with record mode data is given in Appendix C.

The use of the high resolution data provided a better angular resolution, with 448 data points on the unit sphere, compared to 16 points for the real time data. In this way it is possible to distinguish between a butterfly and a bi-directional distribution and to estimate the loss cone near the location of the electron pitch angle boundary whenever record mode data were available. Of particular interest to this work are the Ganymede orbits, due to their close location to the electron pitch angle boundary around $15 R_J$. With the discovery of an intrinsic magnetic field at Ganymede (*Kivelson et al.* 1996), changes in the particle behaviour and therefore the pitch angle distributions, were expected as consequence of the interaction with Ganymede's magnetosphere. Changes due to this interaction have to be disentangled from the global pitch angle distribution change occurring in this region.

Observations in the vicinity of Ganymede during the G28 orbit have clearly indicated that close to the moon the electrons are trapped and then change into field-aligned electron distributions. Figure 3.14, shows the record mode data for two electron channels (in the energy range 29-42 keV and 304-527 keV). The pitch angle distributions in the near of Ganymede have been discussed by *Williams et al.* (2001). Also clearly visible in figures 3.14 and 3.15 is the existence of bi-directional distributions in regions outside of Ganymede's magnetosphere. The magnetosphere of Ganymede is considered to have a diameter of $\sim 4 R_G$ ¹. The analysis of the record mode data related to Ganymede encounters complemented with the Ulysses high latitude measurements (*Krupp et al.* 1997, *Seidel et al.* 1997, *Lanzerotti et al.* 1992) reveals that the electron distributions are indeed bi-directional and not butterfly. It can also be excluded that the electron PAD changes observed are a result of particle interaction with Ganymede since they are observed far away from the moon encounters and produce PADs persisting for extended time intervals/spatial ranges on both sides of the transition.

Furthermore, an example of the high resolution record mode electron pitch angle distributions on orbit C9 (one of the encounters with the moon Callisto at $26 R_J$) shows that the distribution remains bi-directional further out (see figure 3.16).

¹ $1 R_G = 2634 \text{ Km} \sim 0.0368 R_J$

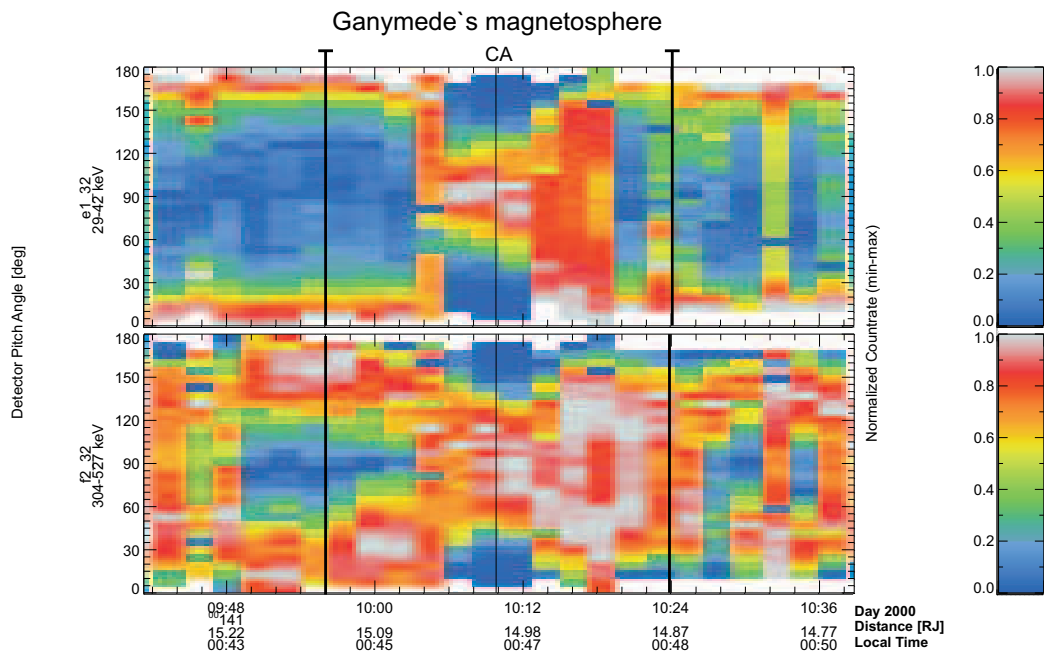


Figure 3.14: High resolution normalised electron pitch angle distributions for the energy range e1: 29-42 keV, and f2: 304-527 keV, during the encounter with Ganymede in orbit G28, day 2000 141. The black lines indicate the extent of Ganymede's magnetosphere.

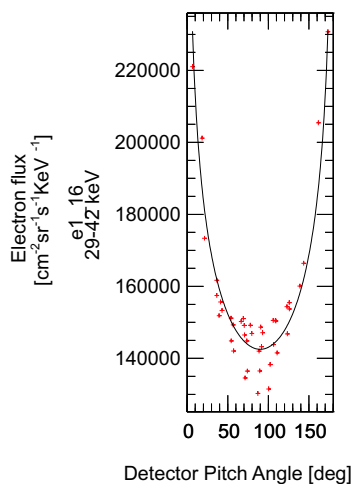


Figure 3.15: High resolution electron pitch angle distribution for the energy range 29-42 keV during the encounter with Ganymede in orbit G28, day 2000 141, at a local time 00:40 h and a radial distance of 15.25 R_J.

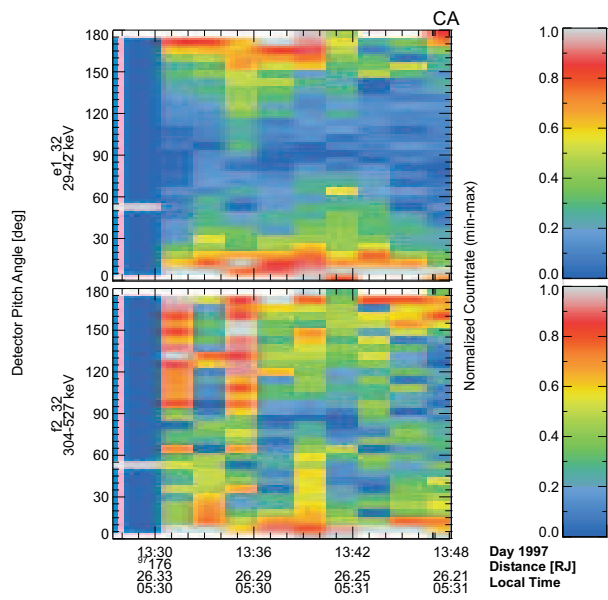


Figure 3.16: High resolution normalised electron pitch angle distributions during the encounter with Callisto in orbit C9, day 1997 176.

4 Origin of the PAD boundary and relation to auroral emissions

In this Chapter the relation between the electron pitch angle boundary observed in the Energetic Particles Detector data and the secondary auroral oval emissions observed by the Hubble Space Telescope will be discussed. First, magnetic field lines are traced from the equatorial plane to the ionosphere, in order to correlate particle signatures with auroral emissions. Then the electron pitch angle scattering by whistler waves generated at the PAD boundary is discussed, as the physical process causing the emission of the secondary oval.

4.1 Tracing of magnetic field lines - From the equatorial plane to the ionosphere

In the previous chapter the energetic particle characteristics in the inner part of the magnetosphere inside $40 R_J$ were studied. It was seen that two distinct regions can be identified. The distinction was based in particular, on the variation of the particles energy spectral index and electron pitch angle distributions. The most prominent and well defined boundary is produced by the distinct change in the electron pitch angles from a pancake or trapped distribution (maximum fluxes at 90°) to a bi-directional distribution which maximises at pitch angles away from 90° . The transition occurs abruptly within a fraction of R_J and often within one 11-min measurement interval of the EPD instrument. It is persistently observed between $10 R_J$ and $17 R_J$, in the equatorial plane, at all local times covered by the Galileo orbits.

The change in the electron pitch angle distribution to a predominantly field-aligned one most probably reflects an enhanced ionospheric precipitation flux. For this reason it is important to link the Galileo EPD measurements in the equatorial plane with the HST observations of the auroral regions of the planet. This is achieved by using two magnetic field models, the VIP4 and the Khurana model, which allow the tracing of the magnetic field lines from the equatorial plane in the magnetosphere to the Jovian ionosphere.

The VIP4 model was initially developed by *Connerney et al.* (1981) and improved later by *Connerney et al.* (1998). It uses the Goddard Space Flight Center (GSFC) O4 model (*Acuña and Ness 1976*) for describing the internal field and models the current sheet by a finite thickness annulus. The internal field model GSFC O4 is based on magnetic field measurements by the flux gate magnetometer experiment on Pioneer 11 and makes use of spherical harmonics analysis in its description. The magnetic field is con-

sidered to be the gradient of a scalar potential which combines both internal and external sources. The coordinate system used is the magnetic equatorial cylindrical system with $\hat{\rho}$ and $\hat{\phi}$ in the equatorial plane and \hat{z} parallel to the dipole axis. In the current sheet region the model assumes that only azimuthal currents are present, which means that the vector potential only has a component in $\hat{\phi}$. The current sheet geometry is chosen to be that of a ring-shaped current sheet starting at $R_0 = 5 R_J$ and ending at $R_1 = 50 R_J$, with a half thickness of $D = 2.5 R_J$.

One of the big advances of the model was the enlargement of the auroral zone which at the time caused some questions as to the interpretation of the auroral emission sources. This problem was better constrained in subsequent work by *Connerney et al.* (1998) which constitutes the current VIP4 model, in use in this work. The model uses the observations of the Io footprint (both H_3^+ and ultraviolet emissions) and magnetic field in-situ measurements to improve the previous version. The resulting magnetic field which combines the O4 internal field model plus a current sheet (described above) and observational constraints is used to better explain a variety of phenomena related to the magnetospheric region up to $30 R_J$. The VIP4 model is currently considered to be the state of the art in magnetic field models (up to $30 R_J$) and field line mapping from the equatorial plane to Jupiter's ionosphere. The Khurana model for the Jovian magnetic field developed by *Khurana* (1997) uses the GSFC O6 model for the internal field, and an Euler potential formulation for the external field. The O6 internal field model described by *Connerney* (1992) uses the same spherical harmonics analysis previously used in the GSFC O4 model to describe the magnetic field due to the internal field of the planet. In this model both Pioneer 11 (1974) and Voyager 1 (1979) measurements are considered. The parameters are comparable to those of the O4 model with the largest differences in the octupole terms. The overall result is the derivation of a more "Earth-like" model than the one obtained by the O4 model. In order to accurately describe the external field in the Jovian magnetosphere the Khurana model considers the complex structure of the Jovian current sheet and the plasma outflow from Io which generates radial and field-aligned currents. The Khurana model provides a description of the magnetosphere also for distances greater than the $30 R_J$ of the VIP4 model, but it does not accurately map the auroral ovals in the southern hemisphere. However it incorporates a local time dependence. A detailed description of both models can be found in Appendix D.

The tracing of the magnetic field lines, with the Khurana model, is done by considering the intersection of the magnetic field line with the equatorial plane, given by radial distance, local time and system III longitude. The tracing allows to obtain the correspondent coordinates (longitude and latitude) in the Jovian ionosphere. To obtain a first estimate of the accuracy of the model, the resulting ionospheric footprints of Io were plotted and compared with the HST observations.

The results can be seen in figure 4.1 for the northern hemisphere (left panel) and for the southern hemisphere (right panel). For reference the footprints of field lines intersecting the equatorial plane at $30 R_J$ are also included. The HST ovals seen in the figures are the result of an extended series of FUV images obtained in the years 2000 and 2001 which provide the best measurements for a representative positioning of the Jovian aurora (*Grodent et al.* 2003). The Io reference oval intercepts the footprint of Io and its trailing tail, and the main reference oval refers to the alignment of the brightest emission. As discussed in section 1.7 (Chapter 1) the secondary oval is observed equatorward of the

main auroral oval and its emissions have approximately half the brightness of the MAO emissions. The secondary oval emissions and their precise location are less well established in the southern hemisphere, and therefore are not indicated for this hemisphere. It is visible from the figures that the Khurana model shows a good agreement with the HST observations in the northern hemisphere, but a bigger deviation from the Io reference oval for the south hemisphere is clearly seen.

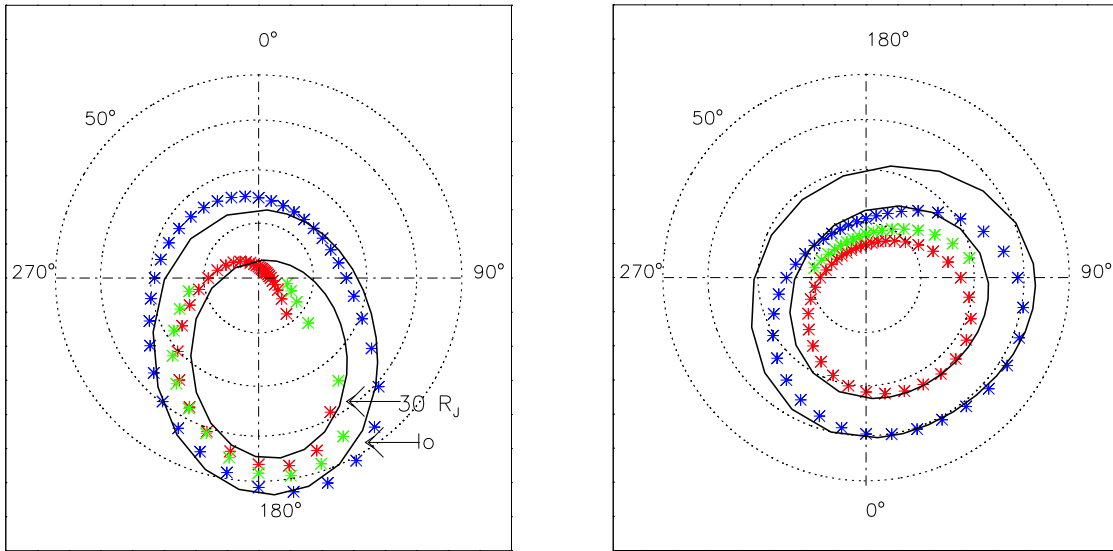


Figure 4.1: Polar view of the Jovian auroral zone. The left panel shows the northern hemisphere and the right panel the southern hemisphere. * indicate the HST observations: blue - Io footprint, red - main auroral oval, green - secondary oval. The black lines indicate the footprints of 30 and 6 R_J (Io), obtained with the Khurana model. The dotted lines indicate the latitude (80° , 70° , 60° and 50°).

The tracing of the magnetic field lines with the VIP4 model is done by considering the intersection of the magnetic field line with the equatorial plane dependent on radial distance and system III longitude only. The model assumes symmetry in terms of local time, and is valid for radial distances up to 30 R_J . As with the previous model, figure 4.2 shows the comparison between the HST observations and the footprint of Io (6 R_J) for the northern hemisphere (left panel) and southern hemisphere (right panel). For reference the footprints of 25 R_J (this distance was preferred instead of 30 R_J since this is the limiting distance for the validity of the model) are shown. The VIP4 model shows a good agreement with the HST observations for both hemispheres.

Figure 4.3 compares the footprints which correspond to 30 R_J equatorial distance and Io for the Khurana model (red) and the VIP4 model (blue). The deviations between the models are strong in the region from 0° to 135° . This region includes the feature known as the kink area. The kink area, as described in section 1.7, is a disturbance observed in the northern auroral emissions due to a surface anomaly.

Figure 4.4 shows the comparison between the footprints of both models for distances of 20 R_J and 15 R_J (Ganymede's orbit). It shows that for these radial distances both models give footprints which are hardly distinguishable from each other, over a wide range of longitudes. However there are again significant differences for the sector between

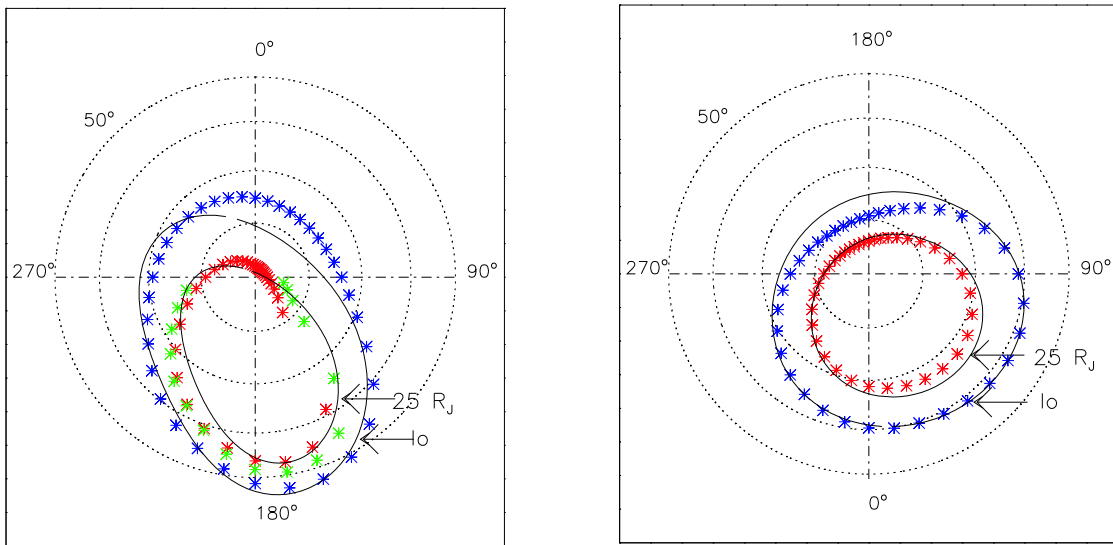


Figure 4.2: Polar view of the Jovian auroral zone. The left panel shows the northern hemisphere and the right panel the southern hemisphere. * indicate the HST observations: blue - Io footprint, red - main auroral oval, green - secondary oval. The black lines indicate the footprints of 25 and 6 R_J (Io), obtained with the VIP4 model. The dotted lines indicate the latitude (80° , 70° , 60° and 50°).

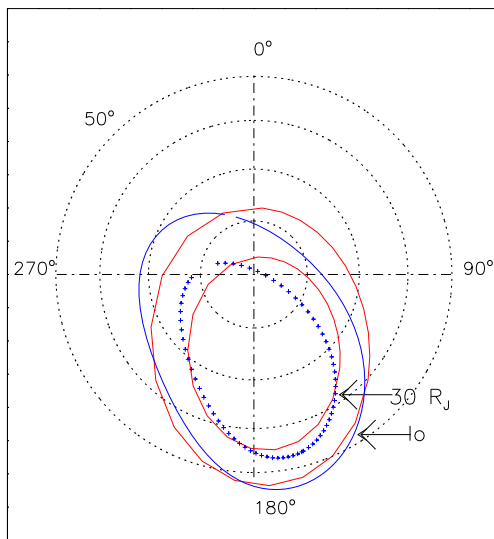


Figure 4.3: Polar view of the Jovian north auroral zone. The footprints of 30 R_J and Io are shown in red for the Khurana model and in blue for the VIP4 model. The dotted lines indicate the latitude (80° , 70° , 60° and 50°).

0° to 135° .

After comparing both models it is seen that the VIP4 model and the Khurana model show a good ability to map the Io auroral emissions for the northern hemisphere. How-

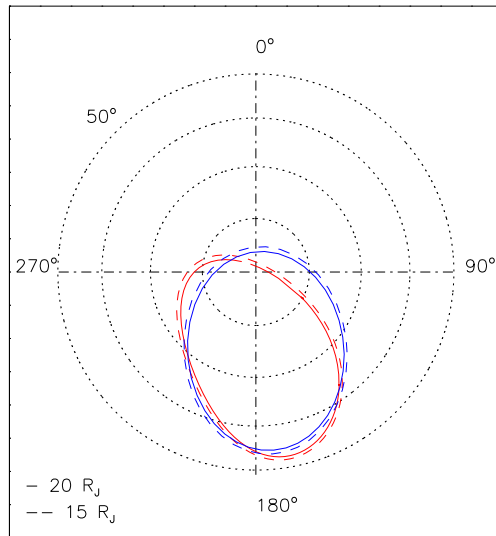


Figure 4.4: Polar view of the Jovian north auroral zone. The solid line indicates the footprint of $20 R_J$ and the dashed line indicates the footprint of Ganymede. Red shows the Khurana model and blue the VIP4 model. The dotted lines indicate the latitude (80° , 70° , 60° and 50°).

ever, the Khurana model shows a bigger deviation in the southern hemisphere. Although the VIP4 model is valid for a smaller range of radial distances than the Khurana model, the electron pitch angle boundary which is the major focus of this work, is well within this range and therefore the VIP4 model was preferred in the continuation of the work.

4.2 The pitch angle boundary and the secondary oval

As shown in figure 4.4 the region between $20 R_J$ and $15 R_J$ at the equator maps to a very small area in the ionosphere and other constraints are necessary when associating these regions of the equatorial plane with auroral emissions. An observational constraint was obtained by *Clarke et al.* (2002) using Hubble Space Telescope observations of the satellites footprints (see figure 4.5). They clearly showed that the main auroral oval is located poleward of the Ganymede's footprint and thus maps to distances greater than $15 R_J$. With this constraint, the electron pitch angle distribution (PAD) boundary (located between $10 R_J$ to $17 R_J$) must be related to features occurring equatorward of the main auroral oval (MAO).

The VIP4 model was used to trace each identified PAD boundary from its location in the equatorial plane to the ionosphere. As can be seen in figure 4.6, the ionospheric footprints of the PAD boundary in general, are closely colocated with the secondary oval (the coordinates of the secondary oval are given in table 4.2). The best agreement is seen in the region from 160° to 190° , which is within the region where the secondary oval is most clearly seen in the HST images (*Grodent et al.* 2003). Table 4.1 summarises the

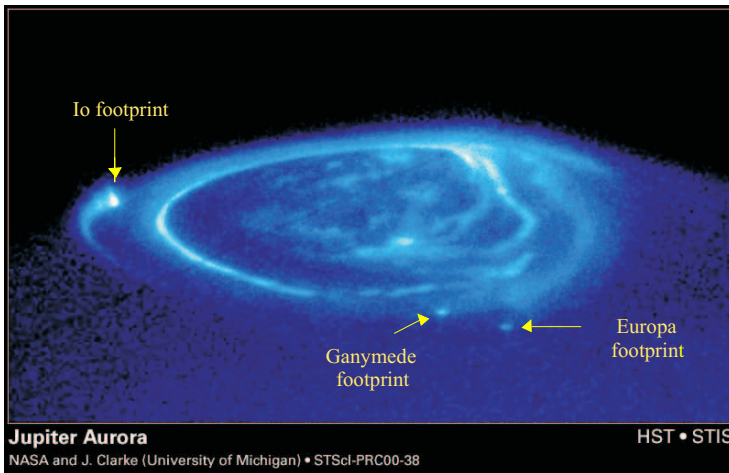


Figure 4.5: Hubble Space Telescope observations of the auroral emissions on the northern hemisphere. The footprints of Io, Ganymede and Europa are seen. Ganymede is clearly visible equatorwards of the main auroral oval (Clarke *et al.* 2004).

location of the PAD boundary in the equatorial plane, in terms of radial distance and system III longitude and the corresponding footprint coordinates (latitude and longitude) in the northern hemispheres as given by the VIP4 model.

In some of the other regions the PAD boundary footprints clearly deviate from the secondary oval. These regions correspond to areas where the secondary oval is harder to detect due to lower brightness or because of merging with the main auroral oval. These are also the regions where the VIP4 model is least reliable, as shown based on the Io footprint mapping.

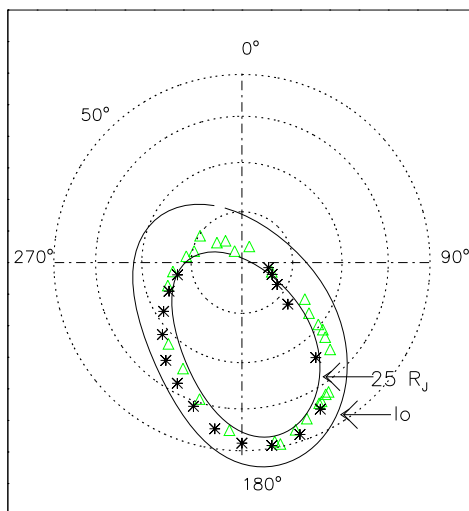


Figure 4.6: Polar view of the Jovian north auroral zone. The solid lines show the footprint of $2.5 R_J$ and Io, given by the VIP4 model. The triangles indicate the ionospheric footprints of the pitch angle boundary and the stars indicate the HST secondary oval. The dotted lines indicate the latitude (80° , 70° , 60° and 50°).

Distance R_J	LT hours	SIII deg	Latitude deg	Longitude deg
14.0	11.0	255.0	66.96	210.96
11.5	12.0	356.0	84.88	320.97
10.0	13.0	107.0	59.65	144.13
12.0	10.0	47.6	75.87	118.26
12.8	9.0	350.0	83.89	306.52
11.0	11.0	67.5	69.59	127.54
11.0	9.4	266.0	68.92	224.27
10.5	9.4	10.2	86.72	26.28
11.0	8.7	109.1	59.60	145.52
10.5	9.0	340.0	80.43	300.75
11.3	7.7	165.7	53.88	167.12
12.3	6.3	63.2	70.96	126.89
14.0	4.0	237.8	62.86	198.51
13.0	1.8	117.0	58.81	149.33
15.0	1.1	53.7	73.77	124.92
15.7	0.7	308.9	76.25	263.17
12.0	18.6	115.0	58.88	148.24
11.0	19.0	72.0	68.30	129.69
10.0	17.5	80.0	65.92	132.37
15.5	20.0	360.0	87.47	325.71
15.0	19.0	298.5	74.71	253.99
13.7	16.3	170.2	54.71	168.81
16.0	18.5	332.0	80.36	282.58
14.5	18.0	210.8	57.81	184.60
15.8	18.0	133.4	57.20	155.82
16.0	16.0	23.0	83.91	105.93
16.5	14.0	324.7	78.97	276.05
15.6	12.0	147.9	55.90	160.89

Table 4.1: Location of the PAD boundary in the Jovian equatorial plane in terms of radial distance (R_J), local time (h) and system III longitude ($^\circ$). The corresponding coordinates, latitude and longitude (in degrees), in the northern hemisphere, are given by the VIP4 model.

Latitude deg	Longitude deg
100	84.69
110	83.71
120	82.01
130	78.17
140	66.86
156	57.58
160	54.59
170	53.95
180	55.11
190	57.68
200	61.02
210	63.80
220	66.14
230	69.23
240	71.99
250	74.63
260	77.08

Table 4.2: Coordinates of the secondary oval, latitude and longitude (in degrees), in the northern hemisphere as observed by the HST (D. Grodent, private communication).

Figure 4.7 summarises the relation between the location of particle measurements in the equatorial plane of the magnetosphere and the northern hemisphere auroral emissions. It shows a sketch of a meridional cut of the Jovian magnetosphere. At the bottom of the figure the distances in the equatorial plane for Io ($6 R_J$), the PAD boundary identified in this work (from $10 R_J$ to $17 R_J$) and the region of break-down of corotation (for $R > 25 R_J$), are indicated. On the top of the figure the corresponding signatures in the ionosphere are shown (equatorward to the left, poleward to the right): Io footprint, secondary oval and main auroral oval. Also indicated are the location of Ganymede in the equatorial plane (at $15 R_J$) and the corresponding footprint emissions. Field lines threading the PAD boundary region from $10 R_J$ to $17 R_J$ (indicated in red) map to the secondary oval auroral emissions.

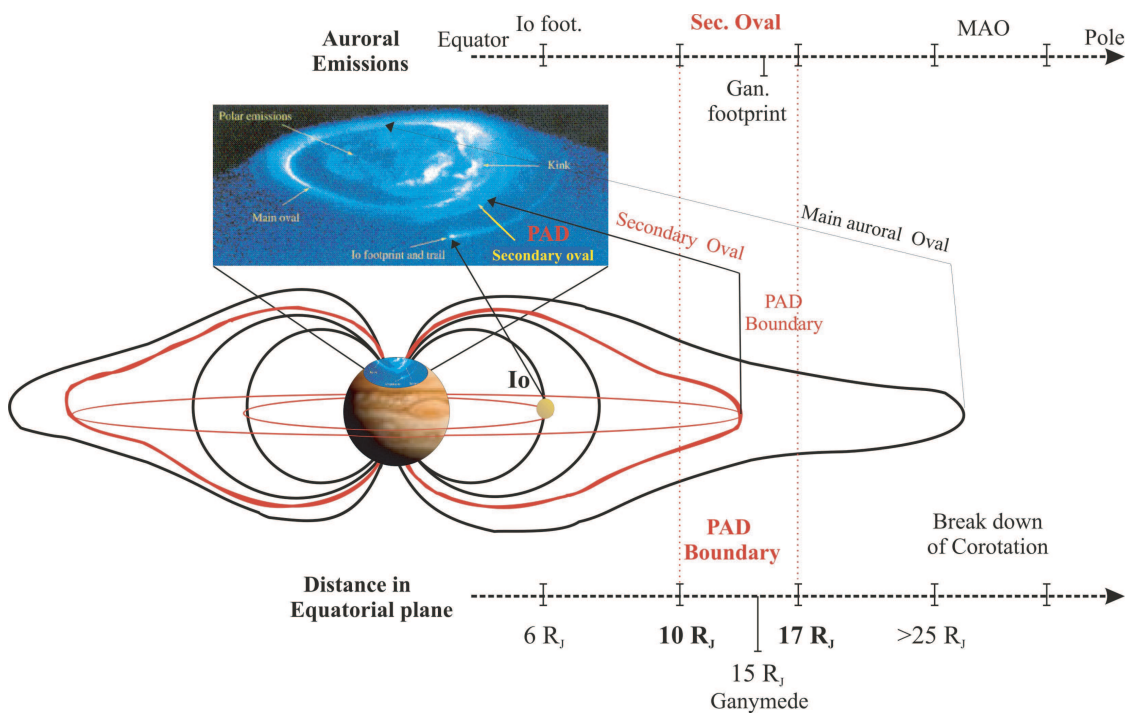


Figure 4.7: Sketch of the Jovian magnetosphere and the auroral emissions in the northern hemisphere. At the bottom of the figure the distance in the equatorial plane (in R_J) indicates: Io, PAD boundary, region of break down of corotation. At the top of the figure the correspondent features in the northern hemisphere auroral emissions are indicated (from equator towards pole): Io's footprint, Secondary oval and Main auroral oval. The region within the red dotted lines corresponds to the PAD boundary in the equatorial plane. HST observations by *Grodent et al.* (2003).

4.3 Simulation of electron pitch angle distribution changes

In Chapter 3 it was shown that the most distinct and sharp boundary in the energetic particle distribution measured by EPD is given by a change in the electron pitch angle

distribution, from a bi-directional to a pancake distribution. This boundary occurs at radial distances from $10 R_J$ to $17 R_J$.

In the previous section it was shown that the footprints of the electron pitch angle boundary are colocated with the secondary oval observed by the HST, suggesting a connection of the electron pitch angle change in the equatorial plane with this auroral feature. Now the question to be addressed is the origin of the PAD boundary, what are the possible mechanisms causing such a distinct and localised boundary? Conservation of the first and second adiabatic invariants would increase the pitch angle of the electrons as they diffuse inwards, into regions of higher magnetic fields. Could adiabatic processes in itself, be responsible for the change in the electron pitch angle distribution?

In this chapter an answer to this question is discussed, by simulating the evolution of an electron distribution, initially at a radial distance of $9 R_J$, in the equatorial plane. By conservation of the first and second adiabatic invariants this distribution is then moved outwards, and the final electron distribution at different radial distances is calculated, taking into account the magnetic field changes as described by the VIP4 model. This approach simulates how the pitch angle, energy and flux of the electrons are changing due to adiabatic processes. The simulation starts at radial distances close to the planet, since a better record mode data set at $9 R_J$ is available and a robust initial distribution is established. The direction in which the simulation is performed does not matter, since the process is fully reversible. This simulation is only a first step in the study of adiabatic processes in the Jovian magnetosphere and their effect on the electron distribution.

The initial electron distribution

In order to establish an initial electron distribution at $9 R_J$ the available record mode data for this region of the magnetosphere was analysed, which corresponds to the close encounters with the moon Europa (only distributions sufficiently far from the moon, i. e. without influence from the moon, were considered). The record mode data is of particular importance due to the very good pitch angle coverage and excellent angular resolution.

Two examples of the electron pitch angle distribution at $9.12 R_J$ on the E11 orbit (upper panel) and at $9.7 R_J$ on the E26 orbit (lower panel) are shown in figure 4.8. The left panels show the pitch angle distribution for the e1 channel (29 keV to 42 keV) and the right panels show the distribution for the f2 channel (304 keV to 527 keV). The fit to the data is obtained by using a loss-cone function:

$$j(\alpha) = f * (\sin(\alpha)^b + c) \quad (4.1)$$

In this particular examples for the E11 orbit (upper panel) the fit is given by:

- e1 channel: $30766 * (\sin(\alpha)^{0.94} + 0.35)$
- f2 channel: $558 * (\sin(\alpha)^{0.43} + 3.31)$

and for the E26 orbit (lower panel):

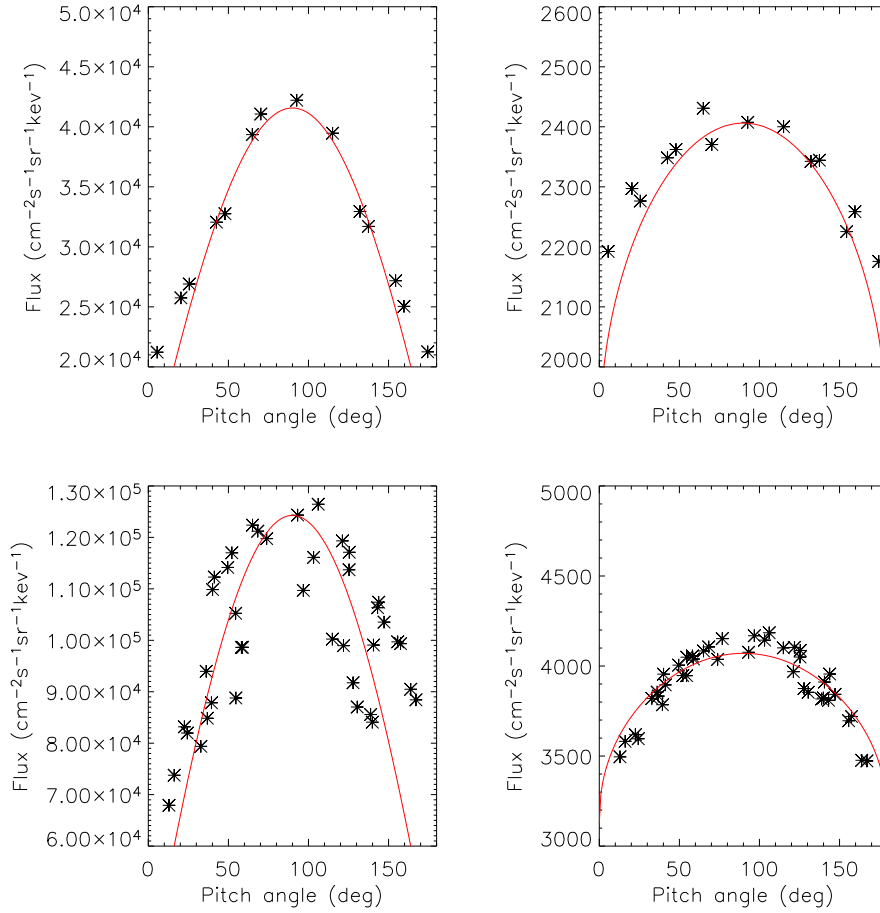


Figure 4.8: Electron pitch angle distribution. The upper panel shows the distribution at $9.12 R_J$ (local time: 11:33 h) on the E11 orbit. The lower panel shows the distribution at $9.7 R_J$ (local time: 02:46 h) on the E26 orbit. Measurements (stars) in the e1 channel (29 keV to 42 keV) are shown in the left, in the f2 channel (304 keV to 527 keV) on the right. The red line indicates the respective fit.

- e1 channel: $119988 * (\sin(\alpha)^{0.94} + 0.35)$
- f2 channel: $945 * (\sin(\alpha)^{0.43} + 3.31)$

For this fit b and c are fixed to the values obtained from the E11 spectra. In the two examples shown, as well as for the other Europa orbits, only the f factor varies considerably, b and c can be kept constant. This means that the differences from orbit to orbit are mainly due to changes in the flux level and not due to changes in the shape of the pitch angle distribution. The difference in the flux levels reflects local time, magnetic latitude and temporal variations. Since the main interest is in comparing the simulated and measured evolution of the profile of the pitch angle distribution with radial distance, an orbit with good coverage of the transition region was chosen. This is only possible using real time data (for reasons discussed in Chapter 2). The G7 orbit is taken as a representative orbit, which exemplifies the pitch angle distribution observed by EPD. For this particular case, and for a radial distance of $9 R_J$ the fit functions are given by:

- For the e1 channel: $j_{e1}(\alpha) = 8.0 \times 10^4 * (\sin(\alpha)^{0.94} + 0.35)$
- For the f2 channel: $j_{f2}(\alpha) = 1.3 \times 10^3 * (\sin(\alpha)^{0.43} + 3.31)$

For both functions ($j_{e1}(\alpha)$ and $j_{f2}(\alpha)$) the b and c parameters, as obtained from the fit to the high resolution data, were taken. The f parameters have been adjusted to this specific orbit. In order to obtain an electron distribution covering different energy ranges, an interpolation is made to the flux functions j_{e1} and j_{f2} , which results in a function $j_i(\alpha_i, E_i)$ (where index i is used to identify quantities of the initial distribution), α_i can vary between 0° and 90° , and E_i between 29 keV and 527 keV. An example of the initial electron distribution in the energy range 50 keV to 60 keV is shown in figure 4.9. In this example the step in pitch angle is 0.05° and in energy 0.3 keV. The distribution is assumed to be symmetric in pitch angle, therefore only the range from 0° to 90° is shown.

Having obtained the initial electron distribution for any given value of α_i and E_i , it is possible to calculate the first and second adiabatic invariants (μ and k , respectively). In addition the phase space density $f = j_i/p^2$, which gives the number of particles per unit volume of momentum space, is also calculated. In the simulation, and according to the Liouville theorem, conservation of the phase space density can be assumed, since loss and transport mechanisms are neglected (they would result from a violation of one of the adiabatic invariants). This allows to retrieve the flux of the particles at a final position.

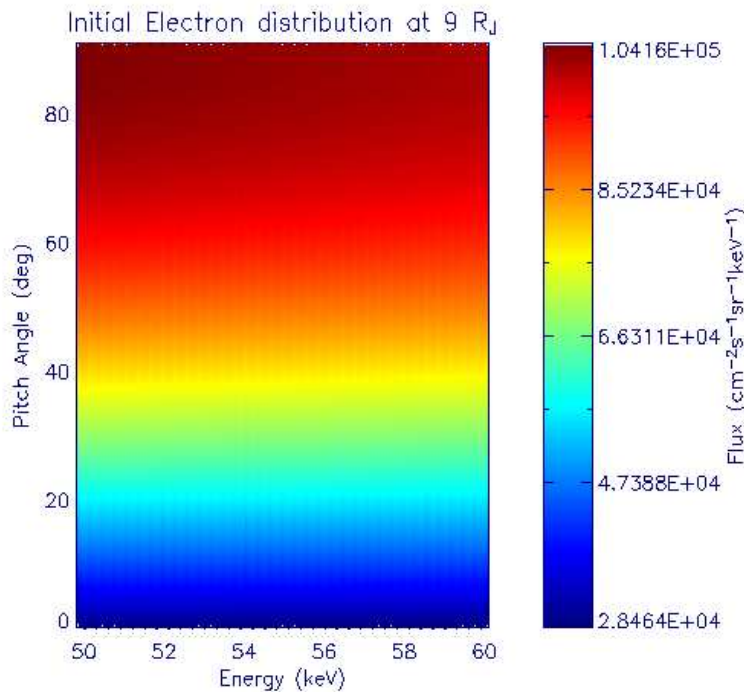


Figure 4.9: Initial electron distribution at a radial distance of 9 R_J.

Calculation of the first and second adiabatic invariant, and of the phase space density

The first adiabatic invariant is given as:

$$\mu = \frac{E_i \sin(\alpha_i)^2}{B_i^{eq}} \quad (4.2)$$

To derive the invariant the values of the initial energy E_i , pitch angle α_i and the equatorial magnetic field B_i^{eq} are considered. The equatorial magnetic field is determined using the VIP4 model.

The second adiabatic invariant is given as:

$$k = \int_{S_m}^{S'_m} \sqrt{\left[1 - \frac{B_i(s)}{B_m}\right]} ds \quad (4.3)$$

To calculate the second adiabatic invariant, the values of the magnetic field along the field line crossing the initial position $B_i(s)$, as well as the magnetic field at the mirror point $B_m = B_i^{eq} / \sin(\alpha_i)^2$ are considered. Knowing B_m the coordinates of the mirror points (S_m, S'_m) , as given by the VIP4 model, can be determined.

The phase space density is given as:

$$f = \frac{j_i}{2m_e E_i} \quad (4.4)$$

To calculate the phase space density the values of the initial flux j_i and the initial energy are taken. The electron mass m_e is $0.511 \text{ MeV}/c^2$.

Obtaining the final distribution

The scheme in figure 4.10 illustrates how the final distribution is obtained. Given a particle with known initial pitch angle and energy (α_i, E_i) , the respective flux, $j_i(\alpha_i, E_i)$ is determined. The first and second adiabatic invariants as well as the phase space density are then calculated. Moving the particle to a final position means a different field line and therefore different magnetic field values $(B_f^{eq}, B_f(s))$, knowing these values and conserving μ , k and f the pitch angle, energy and flux of the particle at the final position (α_f, E_f, j_f) can be retrieved.

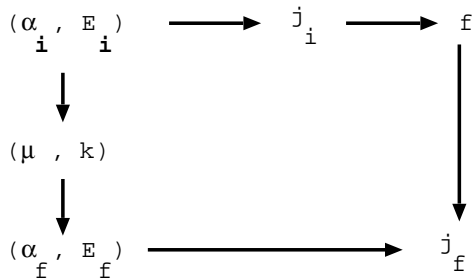


Figure 4.10: Obtaining the final distribution.

Comparison with the measured electron distribution

The simulated and measured electron distribution were compared, by considering the variation of the pitch angle with radial distance for a normalised distribution. This gives a global view of the pitch angle changes but contains no information as to the flux variation. A qualitative study comparing the non-normalised simulated electron distribution at specific positions and the EPD measurements at the same radial distance was also made, which gives information on the flux variations at specific positions. The measured and simulated distributions were compared, in the energy range from 29 keV to 42 keV.

The simulated normalised distribution is obtained in the radial distance range from $9.2 R_J$ to $18 R_J$, at intervals of $0.2 R_J$. For each position the initial energy range is chosen such that the final energy is in the range from 29 keV to 42 keV. The flux is then normalised to the maximum and minimum at each energy step. Two examples of the simulated normalised distribution at a radial distance of $9.4 R_J$ and $15.2 R_J$ are shown in figure 4.11. The radial profile is obtained by taking the normalised distribution at the geometric average of the energy interval. This is a qualitative profile, which illustrates the evolution of the pitch angle, without giving any information on the quantitative variation of the flux level with distance. The comparison with the measured normalised pitch angle distribution during the outbound passage of the G7 orbit, covering the radial range from $9 R_J$ to $40 R_J$, is shown in figure 4.12. In both distributions a change from a maximum flux at 90° to a maximum flux at lower values (closer to 0° or 180°) can be observed.

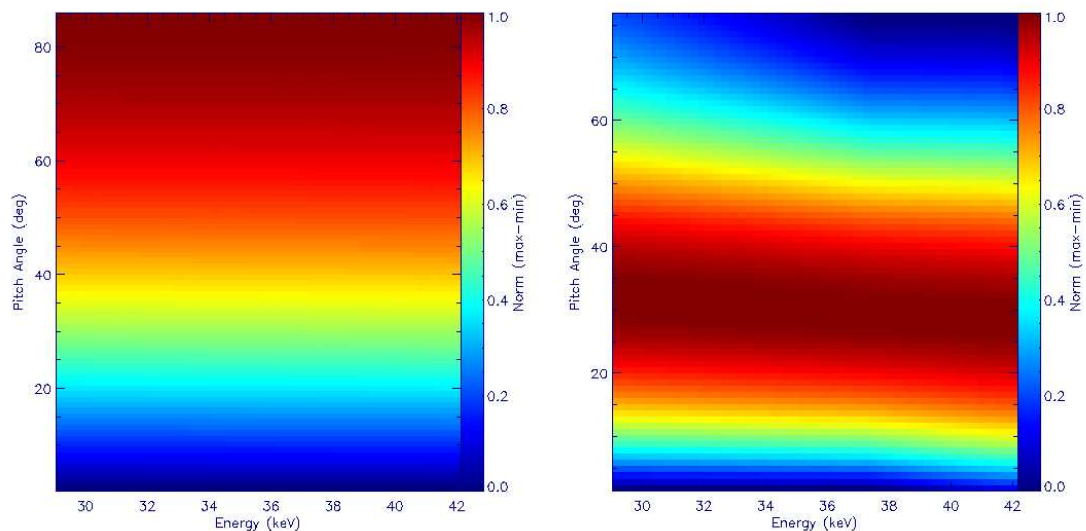


Figure 4.11: Normalised pitch angle distribution. The left panel shows the results at a radial distance of $9.4 R_J$ and the right panel shows the results for a radial distance of $15.2 R_J$. The simulations are shown for an energy range of 29 keV to 42 keV, which corresponds to the e1 channel.

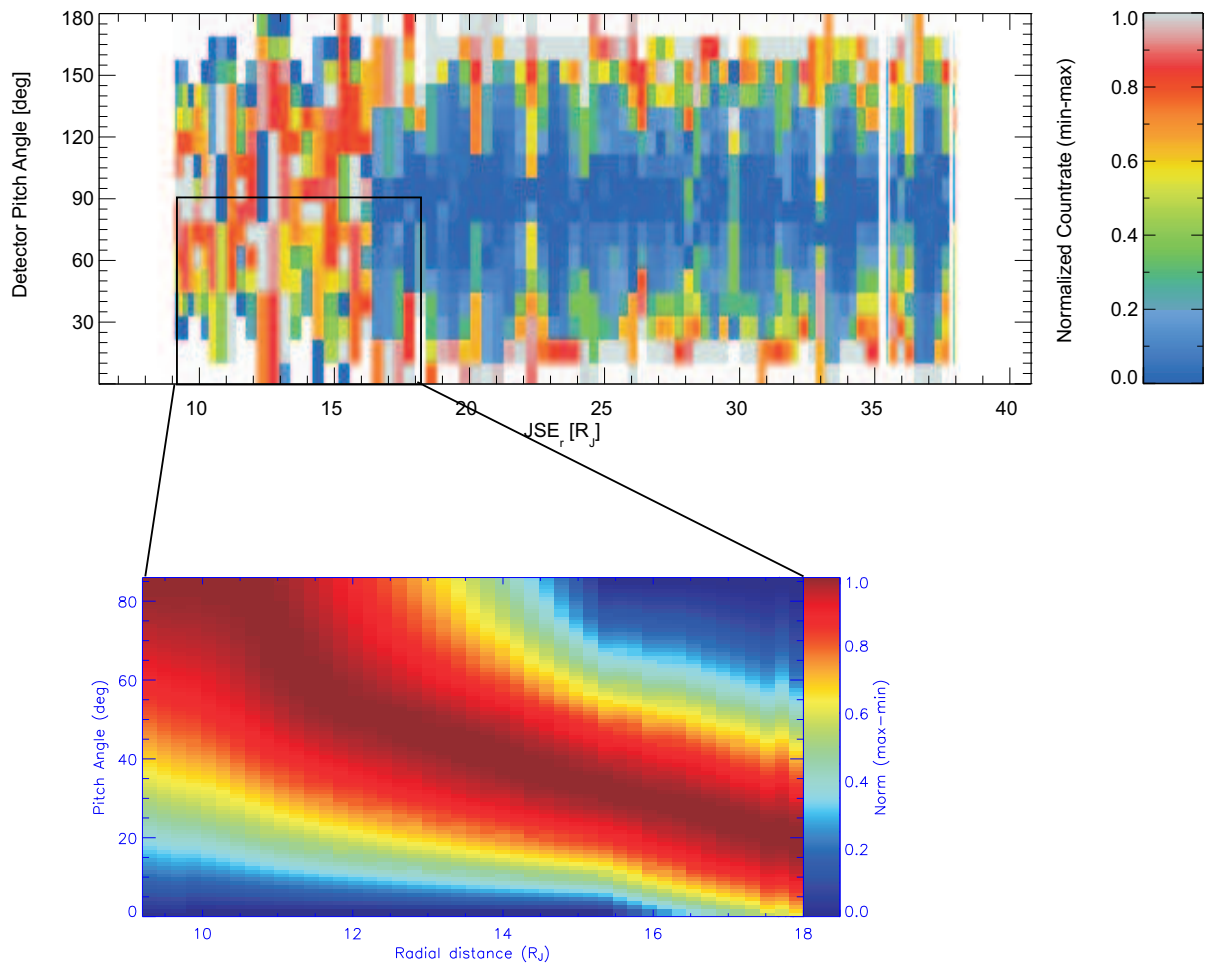


Figure 4.12: Normalised pitch angle distribution. The upper panel shows the measured normalised distribution during the outbound passage of the G7 orbit, for the e1 channel (29 keV to 42 keV). In the lower panel the simulated normalised pitch angle distribution is shown in the radial range from $10 R_J$ to $18 R_J$. In both cases the colour code indicates the particle flux, normalised to the maximum and minimum of each bin.

The non-normalised simulated and measured electron distribution at different radial distances were also compared. The variation of the flux level is not accurately portrayed in the simulation, with the simulated flux values being one to two orders of magnitude lower than the measured ones. This means that to obtain the observed flux levels at $9 R_J$ one has to start with a distribution at $\sim 18 R_J$ of one to two orders of magnitude lower fluxes than the observed ones. In other words, starting with flux levels like observed at larger radial distances would result in much higher flux levels close to the planet.

The discrepancies of the flux can be explained by the assumption of conservation of phase space density. This implies that no diffusion processes are taken into account as the particles move outwards. From calculation of the phase space densities of ions, in the inner Jovian magnetosphere (*Paranicas et al.* 1990), it is known that the phase space density is not conserved. It increases with increasing radial distance, indicating inward radial transport. The variation of the phase space density is given by the diffusion equation,

$$\frac{\partial F}{\partial t} = J(L) \frac{\partial}{\partial L} \left(\frac{D_{LL}}{J(L)} \frac{\partial}{\partial L} (F) \right) + Q - S \quad (4.5)$$

where F is the phase space density, L is the radial distance, D_{LL} is the diffusion coefficient, Q is the source term, S the loss term and $J(L)$ the appropriate Jacobian. It was concluded that the diffusion loss rate of the ions exceeds the strong diffusion limit (*Paranicas et al.* 1990).

One can expect a similar process to occur for electrons, meaning that the phase space density is not conserved, which would significantly change the calculated fluxes. A full derivation of the electron phase space densities in the Jovian magnetosphere is not available at the moment and will be a necessary and important step in the future development of this simulation. Nevertheless important qualitative results concerning the evolution of a pitch angle distribution by conservation of the first and second adiabatic invariants, were obtained using the simulation. It can be seen that the adiabatic processes lead the distribution from a pancake to a bi-directional distribution within the same radial range as observed by measurements. The further development of the simulation, including the calculated electron phase space densities and the diffusion coefficient was beyond the scope of this thesis but will be part of future work on this subject.

4.4 Pitch angle scattering by whistler waves

One of the processes which can explain the enhanced precipitation is the scattering of particles by whistler waves, which can drive the distribution to the strong pitch angle diffusion limit (*Kennel and Petschek* 1966). This process was discussed in detail in section 1.5 of Chapter 1.

Estimation of the critical flux

With the aim of establishing if the pancake distribution as observed at the PAD boundary has free energy to generate whistler waves, the critical flux was calculated. The radial distances considered cover the PAD boundary region between $10 R_J$ and $17 R_J$, and the EPD electron channels are taken in the energy range from 55 keV to 304 keV. The estimation of the critical flux J_c was done as indicated in section 1.5 of Chapter 1. For each channel the critical flux was calculated considering an average energy per channel.

The critical flux was then compared with the electron flux measured by the EPD instrument, for all the orbits where the PAD boundary was established. Figure 4.13 gives an example of the measured flux and the critical flux for the outbound pass of the G2 orbit. The behaviour observed in this example is the same for all the evaluated orbits, with the measured flux (varying in an average range from $10^4 \text{ cm}^{-2} \text{ sr}^{-1} \text{ s}^{-1} \text{ keV}^{-1}$ to $10^5 \text{ cm}^{-2} \text{ sr}^{-1} \text{ s}^{-1} \text{ keV}^{-1}$) being always higher than the critical flux (average range from $10^3 \text{ cm}^{-2} \text{ sr}^{-1} \text{ s}^{-1} \text{ keV}^{-1}$ to $10^4 \text{ cm}^{-2} \text{ sr}^{-1} \text{ s}^{-1} \text{ keV}^{-1}$), indicating that the production of waves in this region of the magnetosphere is possible.

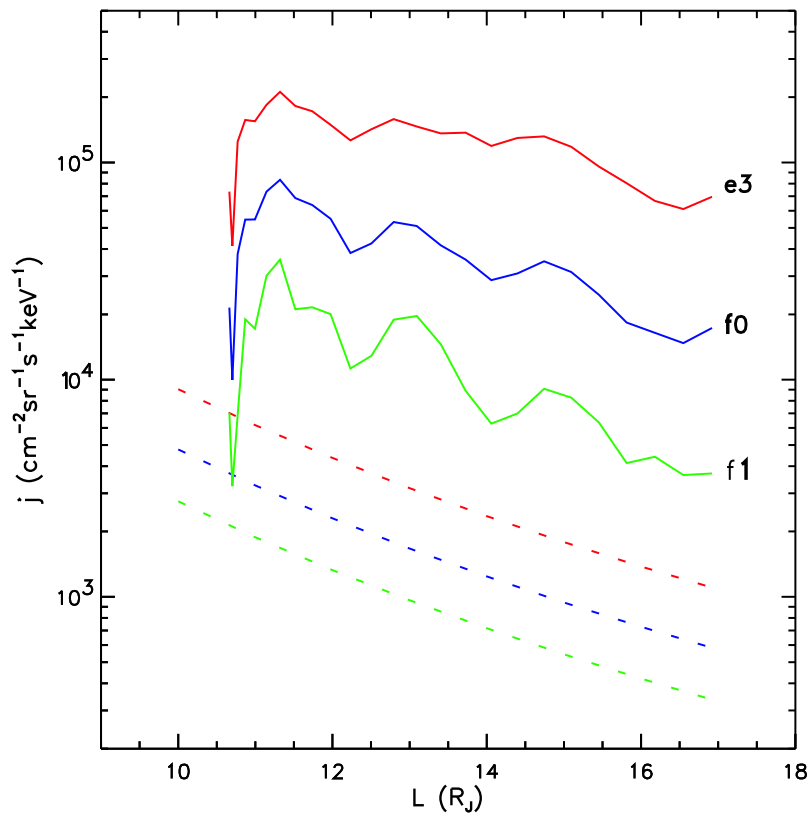


Figure 4.13: Critical flux compared with the measured flux for the outbound pass of the G2 orbit at radial distances 10-17 R_J . The solid lines indicate the measured flux, and the dotted lines indicate the critical flux. In red is the energy channel e3: 55 keV to 93 keV; Blue is the energy channel f0: 93 keV to 188 keV and in green is the energy channel f1: 174 keV to 304 keV.

The wave data

The presence of whistler waves in the PAD boundary region can be confirmed by analysing the frequency-time spectrograms obtained by the PWS instrument on board Galileo. A brief description of the instrument is given in section 2.4 on Chapter 2.

The frequency-time spectrograms used here show the intensity of the electric field component of the waves. The example in figure 4.14 shows the frequency-time spectrogram for days 1997 176 to 1997 180 on orbit C9, for a time period of 2 days around the PAD boundary, for both inbound and outbound pass.

The intensity of the waves is given in terms of spectral density (which is related to the electric field component of the waves) for frequencies in the range from 10 Hz to a few 10^6 Hz. The frequency range covers several different emission types. In the higher frequency range, from a few hundred kHz to the 5.6 MHz limit, are hectometric emissions. In the range from 100 to a few 100 kHz there is a narrow band emission, which is close to the electron plasma frequency (fpe). At specific frequencies, from a few kHz to ~ 100 kHz, are electron cyclotron harmonic frequencies (fce). Below both fpe and fce are a set of broadband emissions of high intensity, generally below 1 kHz. They are whistler mode emissions known as hiss. These emissions are considered in this work to cause the pitch

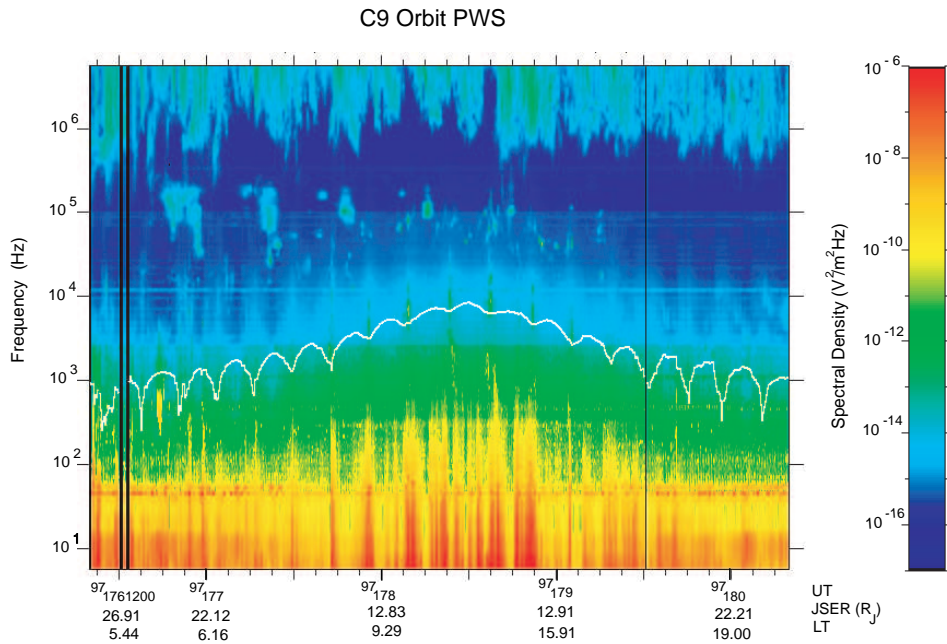


Figure 4.14: Frequency-time spectrogram showing the intensity of the electric field component of waves during days 1997 176 to 1997 180, in the radial range from 26.91 R_J inbound to 22.21 R_J outbound, and a local time of 5.4 h to 19.0 h (inbound and outbound respectively). Data courtesy of W. S. Kurth, Univ. of Iowa, USA.

angle scattering associated with the sharp pitch angle transition. Analysing the frequency-time spectrograms for the same orbits as previously done for the EPD data provided some insight as to the behaviour of the whistler waves near the electron PAD boundary region. Generally the intensity of the whistler waves at the region of the PAD boundary is high, with spectral densities in the range from 10^{-10} $V^2/m^2/Hz$ to 10^{-6} $V^2/m^2/Hz$. During most of the orbits there is also an enhancement of the wave intensity around the PAD boundary.

Only those segments of the Galileo orbits far enough away from Ganymede were analysed, to exclude effects from the moon itself. One of the clearest examples is seen in figure 4.15 which shows in detail the electron PAD (in the energy range 304 keV to 527 keV) and the frequency-time spectrogram for the outbound passage of the G7 orbit. A strong sporadic enhancement in the wave intensity is seen which is due to the Ganymede encounter, but a second enhancement is also clearly visible. The onset of the enhancement is collocated with the PAD boundary. With the information obtained from the analysis of the frequency-time spectrograms the study of the PAD boundary can be further advanced by estimating the pitch angle diffusion coefficient.

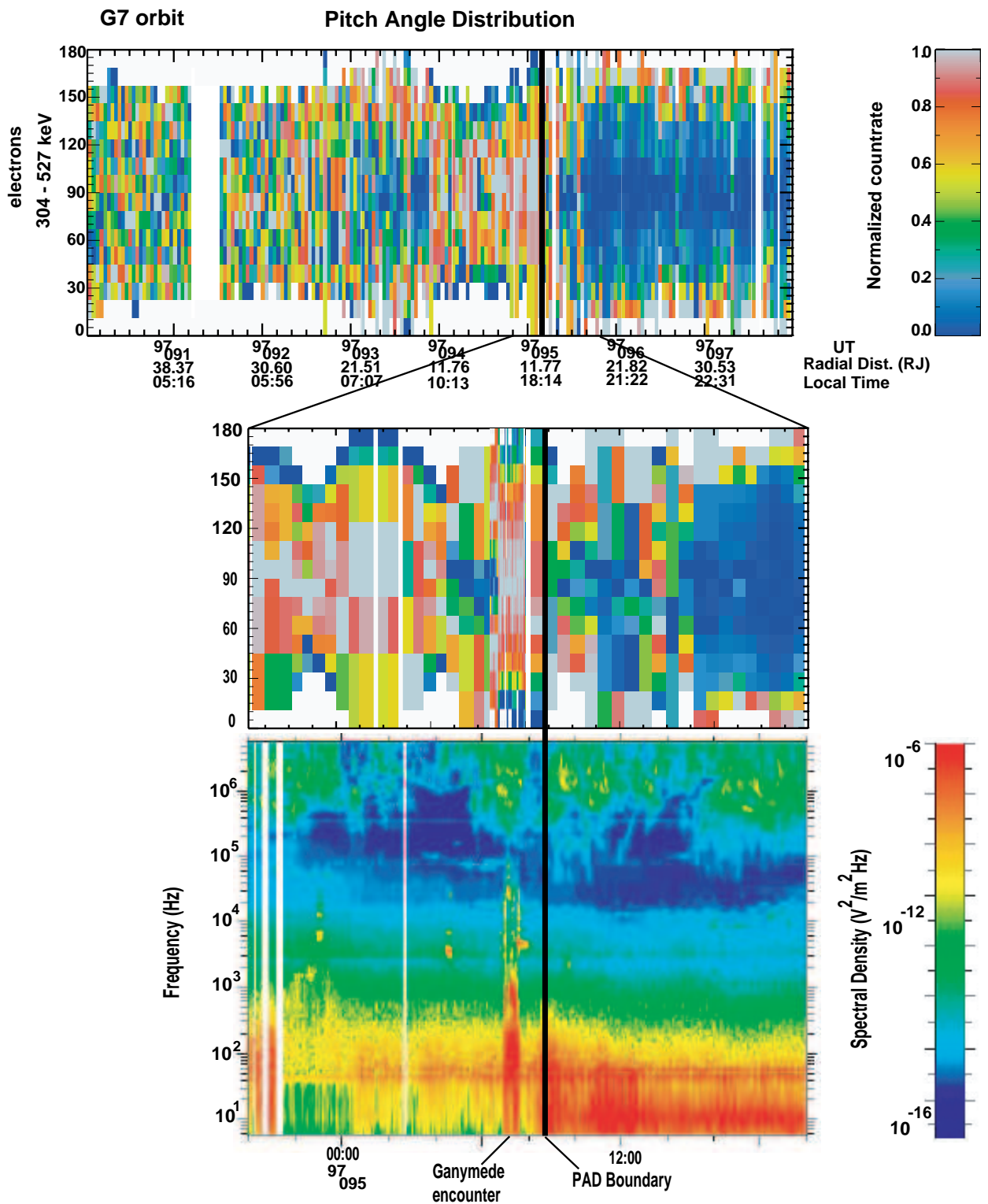


Figure 4.15: Top: Pitch Angle distribution of electrons (304 keV to 527 keV) during the G7 orbit (days 1997 90 to 98), in a range of $40 R_J$ around the planet. Bottom: Frequency-time spectrogram showing the intensity of the electric field component of waves for the time period corresponding to the pitch angle boundary on the dusk side, days 1997 094,2000 UT to 1997 095,2000 UT (black line). Adopted from *Tomás et al.* (2004b).

	Minimum	Maximum
Spectral density - S (V^2/m^2Hz)	10^{-10}	10^{-6}
Electron gyrofrequency - f_c (Hz)	2000	12 000
Wave frequency - f (Hz)	10	100
ϵ	0.1	1
Radial distance - L (R_J)	10	17

Table 4.3: Considered range of the parameters for the estimation of the pitch angle diffusion coefficient.

Estimation of the pitch angle diffusion coefficient

In order to verify the strong diffusion limit the pitch angle diffusion coefficient was estimated and compared with the theoretical limit of strong diffusion (considering the scattering of particles across the dimension of the loss cone). The strong diffusion limit is given by equation 4.6, according to *Thorne and Tsurutani (1979)*.

$$D_{SD} = \left(\frac{v}{4R_J} \right) \frac{1}{L^4} \quad (4.6)$$

This expression is valid for a dipolar field approximation. This is considered to be an acceptable approximation for the PAD boundary since the correspondent radial distances are within a few Jovian radii of the dipolar region. The pitch angle diffusion coefficient is given by equation 1.16, as previously indicated in Section 1.5 of Chapter 1. The range of values considered in the estimation can be seen in Table 4.3.

Figure 4.16 gives an example of the ratio between the pitch angle diffusion coefficient and the strong diffusion limit. In this particular case the strong diffusion limit was calculated, for electrons with an average energy of 230 keV (corresponding to the geometric average of the energy channel from 174 keV to 304 keV). The pitch angle diffusion coefficient was estimated considering $\epsilon = 0.1$, $f_c = 2000$ Hz, and varying f and S as indicated in the figure. Depending on the different choice of parameters it was found that the pitch angle diffusion coefficient is one to two orders of magnitude higher than the strong diffusion limit. It can be concluded that the conditions for strong pitch angle scattering are satisfied.

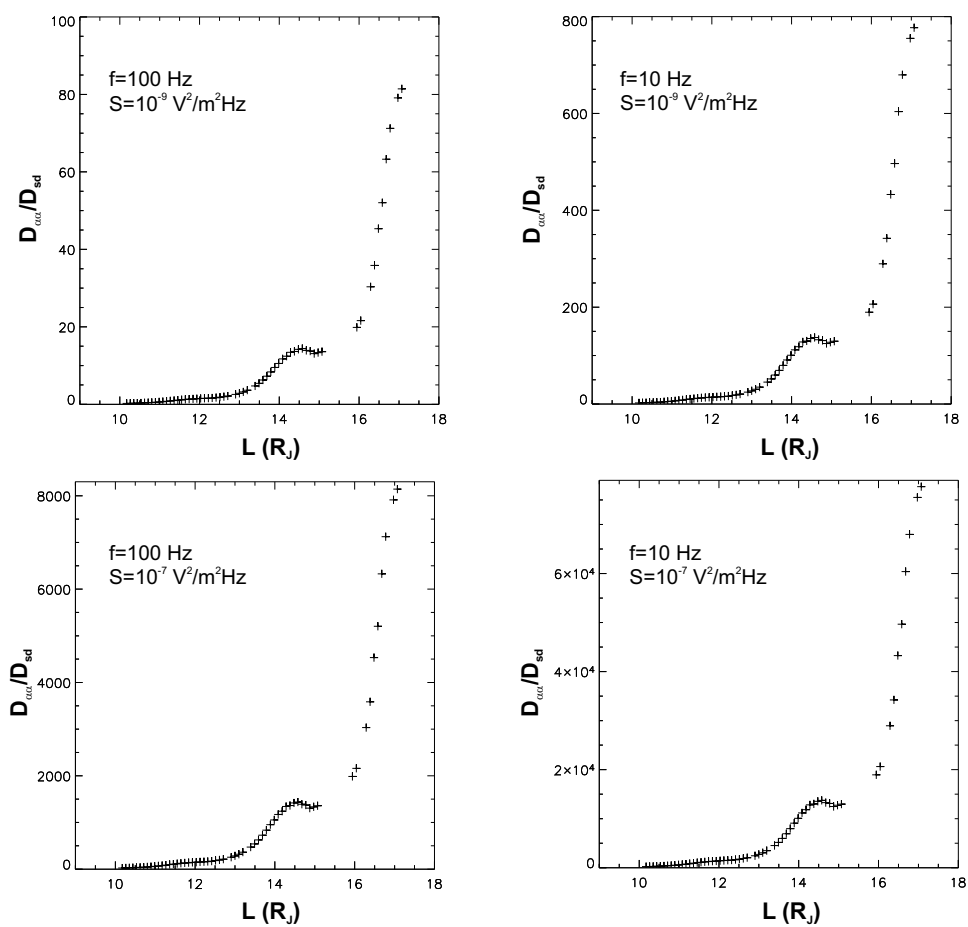


Figure 4.16: Ratio between the pitch angle diffusion coefficient and the strong diffusion limit for electrons with an average energy of 230 keV. The parameters for the calculation of the pitch angle diffusion coefficient are indicated in the text.

4.5 Precipitation energy flux

As mentioned at the beginning of this chapter the change in the electron pitch angle distribution from a bi-directional to a pancake distribution could lead to an enhancement of the ionospheric precipitation flux due to excitation of whistler waves which generate strong scattering. Furthermore, as discussed in section 4.1, the PAD boundary maps to the HST secondary oval. To further establish the PAD boundary as the source region for the secondary oval, the precipitation energy flux carried by the energetic electron population measured by the EPD instrument at the PAD boundary was estimated.

In the PAD boundary region the electron PAD changes from a distribution without to a distribution with free energy for whistler wave generation. Furthermore in section 4.4 it was shown that the measured electron flux exceeds the critical flux limit for the production of whistler waves at the PAD boundary. Thus, it can be assumed that enhanced scattering by whistler waves leads to enhanced precipitation. Furthermore, the presence of whistler waves was confirmed by analysing the frequency-time spectrograms obtained by the PWS instrument on board Galileo. Based on the measured wave parameters, it was possible to estimate the pitch angle diffusion coefficient and to verify that the assumption of strong diffusion is justified for the calculation of the precipitation energy flux.

The precipitation energy flux can be derived from the energetic electron population at the plasma sheet centre. For the EPD energy range a power law distribution can be assumed for the electron energy spectrum, such that: $j \propto E^{-\gamma}$, where j is the electron flux, E the electron energy and γ the spectral index (see section 3.1 in Chapter 3).

The precipitation energy flux, is given by (according to (Thorne 1983)):

$$\varepsilon = 4\pi \int_{E_{min}}^{E_{max}} E j(r, E) dE \quad (4.7)$$

Two energy ranges were considered, from $E_{min}=55$ keV to $E_{max}=188$ keV and from $E_{min}=55$ keV to $E_{max}=304$ keV, since they cover the energy range of the electrons believed to be responsible for the secondary oval emissions (D. Grodent, Private communication). The integration is made over the unit sphere and not only over the loss cone, since strong diffusion was assumed, which means that the flux equally precipitates in both hemispheres (as discussed below). It therefore represents the maximum precipitation flux.

In the case of strong diffusion the scattering occurs rapidly and the flux precipitates into both hemispheres with equal probability, since the differences between the north and south nominal loss cones (defined in Appendix A) are negligible. If the scattering of particles is not as efficient as for strong diffusion, the process is slower and the particles will bounce between mirror points until they are lost and the precipitation flux can differ with the particles preferentially precipitating into the hemisphere with the bigger loss cone. In order to verify the extent of this effect and how it would affect the calculation of the precipitation flux, the loss cones for both hemispheres were estimated. The measured magnetic field at the PAD boundary and the magnetic field in the ionosphere where the related field lines map to (considering the VIP4 model) were taken. It was found that for 33 % of the points the nominal loss cone values do not differ significantly. In those cases where the difference was comparatively larger, there was no significant preference of one of the two hemispheres with respect to the precipitation flux. Thus, the flux being calculated represents the maximum electron precipitation energy flux that can reach the

ionosphere, with equal probability for both hemispheres.

The estimated precipitation energy fluxes for both energy intervals, and the corresponding coordinates of the PAD boundary location are shown in Table 4.4. The precipitation flux has been converted into brightness¹ to compare with the HST measurements. Given the uncertainty in placing the PAD boundary and the error inherent to the fit calculation of the spectrum, the error in the calculation of the precipitation fluxes is of the order of 25%. The estimated values are in the brightness ranges between 32 kR and 115 kR, for the energy interval 55 keV to 188 keV and from 60 kR to 320 kR (for the energy interval 55 kR to 304 keV). These values are comparable to the brightness ranges observed in the secondary oval, which are on average similar to the Io trail emissions of about 40 kR (Gérard *et al.* 2002). The calculated precipitation flux is above the average value of 40 kR, in particular for the extended energy range. However, the derived values correspond to the case of strong diffusion and therefore represent an upper limit. Thus the derived values for the precipitation flux and the brightness values of the secondary oval are in reasonable agreement.

This fact further supports our assumption that the PAD boundary is related to the discrete emissions of the secondary oval, and not to diffuse emissions, as previously suggested by *Bhattacharya et al.* (2001). They have analysed EPD data in the region from $10 R_J$ to $25 R_J$ for electrons in the energy range from 15 keV to 884 keV and found precipitation fluxes above ~ 100 kR. In their work they investigate the possibility that the broad region of diffuse emissions adjacent to the main auroral oval (which seems to be the result of a gradual process) is caused by strongly scattered electrons. By considering only the PAD boundary which is spatially confined to a $1 R_J$ to $2 R_J$ wide region within the distance range of $10 R_J$ to $17 R_J$, and the electron energies (~ 100 keV) believed to be responsible by the secondary oval emissions, this work constrains the physical processes at the origin of the discrete secondary oval.

An analysis of the variation of the precipitation flux with system III longitude in the ionosphere was done in expectation of future work on local time variation of auroral emissions, to allow the comparison with brightness profiles of the secondary oval (these profiles are not yet available). Figure 4.17 shows the precipitation flux for both north (top panel) and south (bottom panel) hemispheres. A study of the dependence of the precipitation flux or local magnetic field strength at the ionospheric footpoint did not reveal a correlation due to lack of measurement points.

¹ 1 ergscm^{-2} corresponds to 10 kR (*Grodent et al.* 2001)

Distance R_J	LT hours	SIII deg	pflux1 kR	pflux2 kR
14.0	11.0	255.0	38	59
11.5	12.0	356.0	63	150
10.0	13.0	107.0	65	118
12.0	10.0	47.6	76	105
12.8	9.0	350.0	36	63
11.0	11.0	67.5	87	196
11.0	9.4	266.0	108	276
10.5	9.4	10.2	67	115
11.0	8.7	109.1	85	168
10.5	9.0	340.0	74	202
11.3	7.7	165.7	115	319
12.3	6.3	63.2	32	68
14.0	4.0	237.8	56	106
13.0	1.8	117.0	85	201
15.0	1.1	53.7	62	121
15.7	0.7	308.9	71	141
12.0	18.6	115.0	69	78
11.0	19.0	72.0	79	217
10.0	17.5	80.0	86	207
15.5	20.0	360.0	64	128
15.0	19.0	298.5	79	163
13.7	16.3	170.2	46	72
16.0	18.5	332.0	59	105
14.5	18.0	210.8	70	125
15.8	18.0	133.4	78	159
16.0	16.0	23.0	66	127
16.5	14.0	324.7	46	86
15.6	12.0	147.9	67	135

Table 4.4: Location of the PAD boundary in the Jovian equatorial plane in terms of radial distance (R_J), local time (h) and system III longitude ($^\circ$), and the estimated precipitation fluxes originating from this region using different energy intervals (pflux1 for the energy interval [55,188] keV; pflux2 for [55,304] keV)

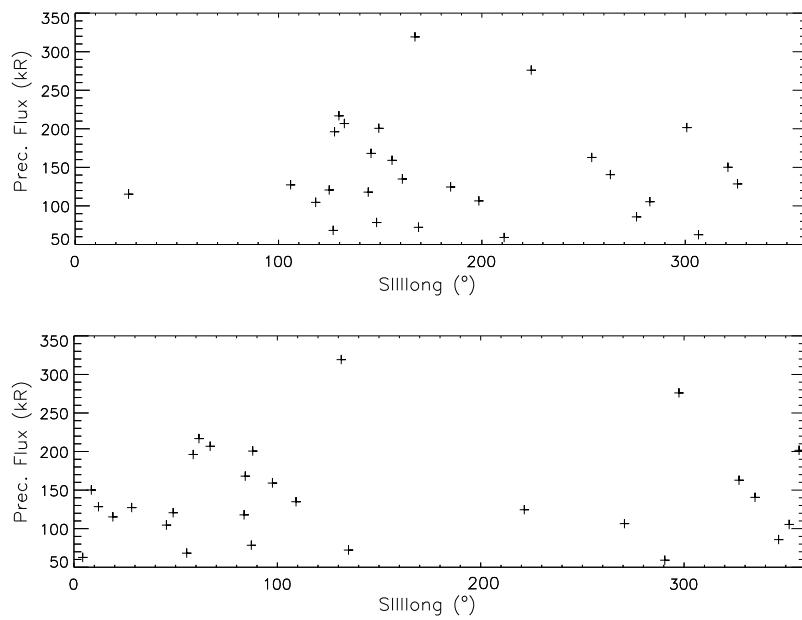


Figure 4.17: Longitudinal dependence of the precipitation energy flux for the north and south hemisphere (top and bottom panel respectively).

4.6 The PAD boundary and the Nishida model

The evolution of the pitch angle distribution is in principal inherent in the circulation model for the Jovian energetic population, the Nishida model, which was explained in section 1.5 of Chapter 1. The model suggests a process of transporting particles outward from the radiation belts without significant loss of energy, and subsequent inward transport with major acceleration. This process has been divided in four steps. The PAD boundary identified in this study would be related with step 1 and 2 of the process.

In the first step of the model the energetic particles are radially diffused inwards, conserving the first and second adiabatic invariants. In this process they are accelerated and their pitch angle increases towards 90° . In section 4.3 the electron pitch angle distribution in radial distances from $10 R_J$ to $18 R_J$ assuming conservation of the first and second adiabatic invariants have been simulated. The bi-directional pitch angle distribution indeed changes to a pancake distribution which is in agreement with step 1 of the Nishida model.

A pancake distribution is a necessary condition for whistler wave generation. In section 4.4 it was furthermore shown that the free energy present in the electron pitch angle distribution is indeed sufficient to cause whistler wave instability as predicted by *Kennel and Petschek* (1966). Whistler waves lead to particle scattering and enhancement of the precipitation flux (step 2 of the Nishida model). The presence of whistler waves in the PAD boundary region was confirmed by the PWS on board Galileo. With the observed wave parameters it was possible to calculate the pitch angle diffusion coefficient and to verify that the conditions for strong pitch angle scattering are satisfied. Under this assumption the energy precipitation flux of electrons from the PAD boundary region was calculated (see section 4.5). It was verified that the estimated values are comparable to the brightness ranges observed in the secondary oval. Thus, this work confirms essential assumptions of the Nishida model.

The simulation has shown that the inward diffusion of particles in the Jovian magnetosphere leads to a change from a bi-directional to a pancake distribution. However, in contrast to the Nishida model, where the PAD change occurs gradually over the whole transport region from the outer to the inner magnetosphere, the simulation showed that the transition occurs abruptly within a few R_J , in the region where the magnetic field changes from a current sheet topology to a dipolar one. Since the PAD change occurs abruptly a strongly localized onset of whistler waves and enhanced particle scattering results. This gives rise to a discrete auroral emission belt.

The Nishida model involves a variety of complex processes which have raised some questions concerning the validity of the model. One of the controversial points is the prediction of the model of outward transport of particles at low altitudes. This aspect of the model was investigated by *Sentman et al.* (1975) using Pioneer 11 data. The authors estimated the streaming index for both protons and electrons. The streaming index S (see equation 4.8) is a measure of the net relative flux through a unit area perpendicular to the magnetic field and it indicates the direction of the flux. S is positive for fluxes in the direction of positive \mathbf{B} , with α being the pitch angle and $f(\alpha)$ the pitch angle distribution in this study. *Sentman et al.* (1975) found that while for the northern hemisphere both electron and proton fluxes were directed outwards, for protons in the southern hemisphere the flux was directed inwards, thus the model prediction was not fully verified.

$$S = \frac{\int f(\alpha) \cos \alpha d\alpha}{\int f(\alpha) |\cos \alpha| d\alpha} \quad (4.8)$$

To address this concern the streaming index was calculated using the more recent data set obtained by the EPAC instrument on board Ulysses, during the Jupiter encounter in 1992. The analysis was done using the data for high latitudes in the northern and southern hemisphere. The streaming index for protons in the energy range from 630 keV to 770 keV can be seen in figure 4.18. They were found to be positive in the northern hemisphere (left panel) and negative in the southern hemisphere (right panel) which indicates that the flux is directed outwards in both cases, contrarily to the previous indications by *Sentman et al. (1975)* and corroborating the recirculation model predictions.

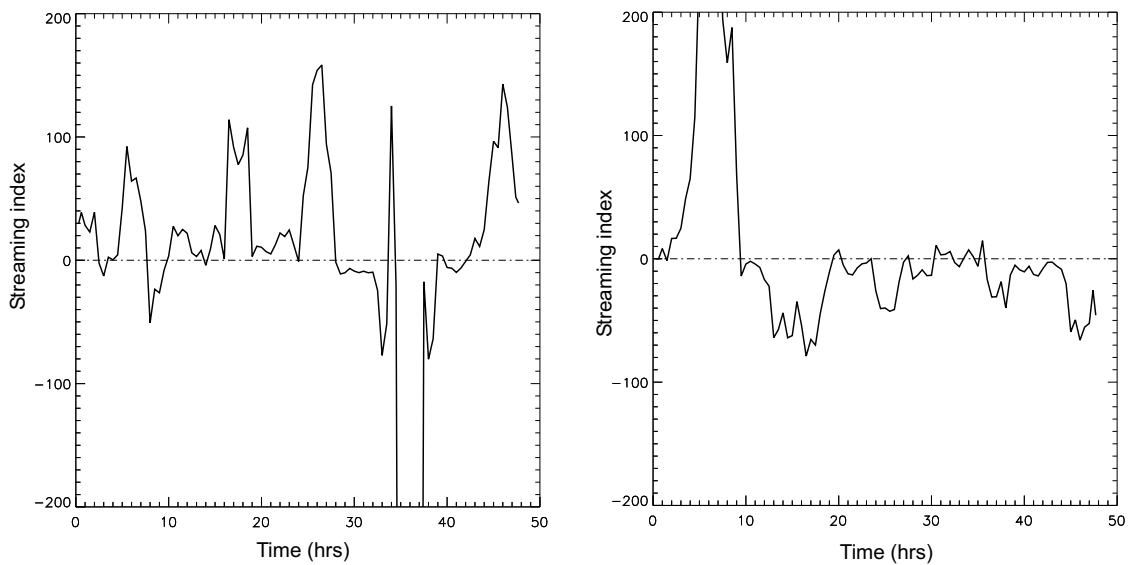


Figure 4.18: Streaming index for protons in the energy range 630 keV to 770 keV (based on Ulysses EPAC measurements). Left panel: northern hemisphere, days 36 to 38 in 1992. Right panel: southern hemisphere, days 40 to 42 in 1992.

Another prediction of the recirculation model is the injection of high energy particles into the outer region of the magnetosphere. This means that the spectral index of the particles should show a harder spectra for high energy particles in the outer part of the magnetosphere. Using the EPD data it was possible to verify this aspect of the model by calculating the ratios of the spectral index for low (29 keV to 93 keV) and high energies (174 keV to 527 keV) in the region of the magnetosphere up to $\sim 60 R_J$. Figure 4.19 shows examples of the calculated ratio for four different orbits (C3, G7, C9 and G28). It was found that in the outer regions of the magnetosphere the spectral index for low energy particles is larger than the spectral index for high energy particles. This means that the energy spectrum is harder for high energy particles, indicating that there is a larger fraction of high energy particles present in this region of the magnetosphere. This behaviour was found on all studied orbits. It is in agreement with the predictions of the recirculation model that high energy particles are injected into the outer magnetosphere.

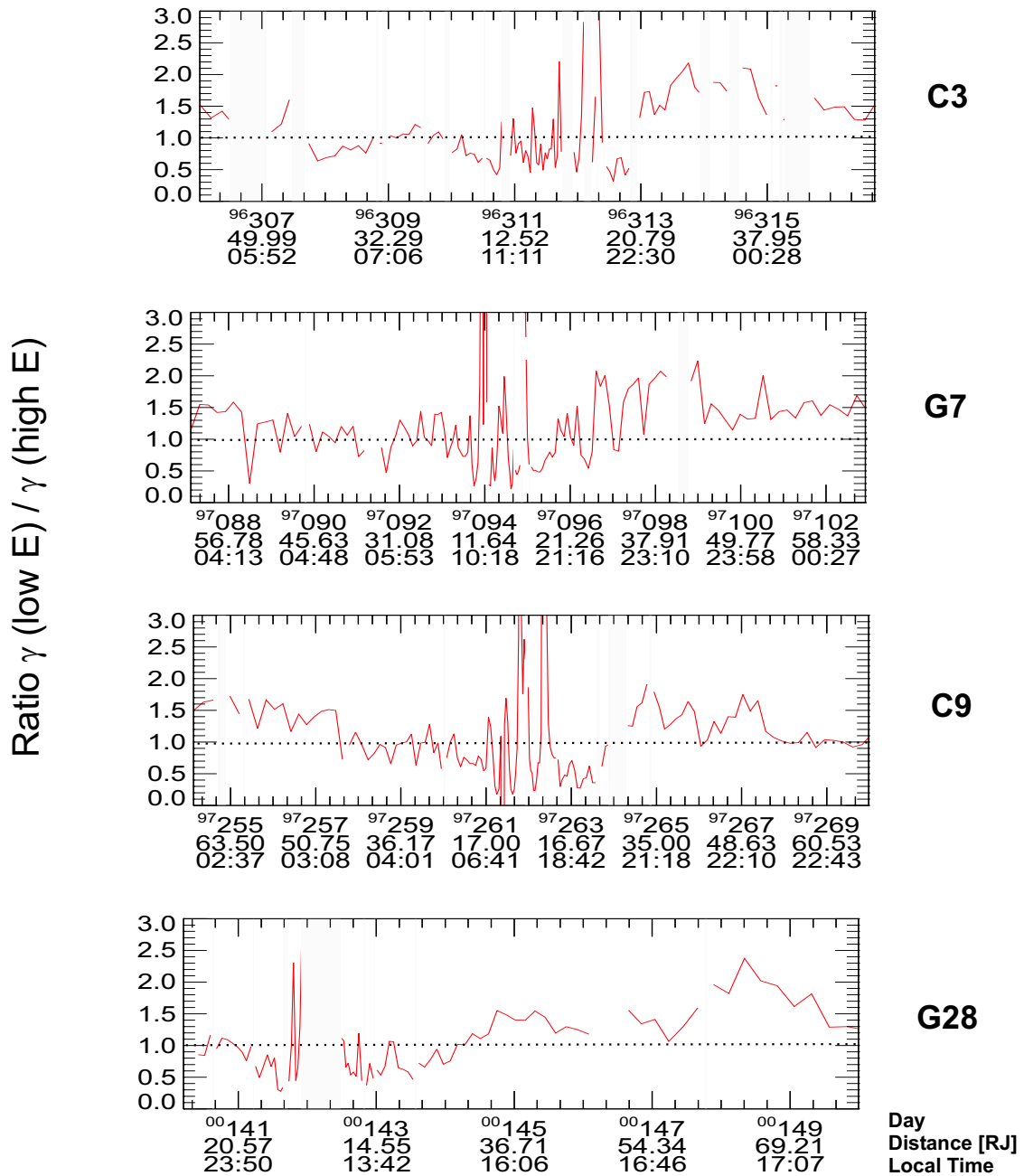


Figure 4.19: Ratio of the spectral index for low (29 keV to 93 keV) and high energies (174 keV to 527 keV) for orbits: C3 (days 1996 306 to 1996 317); G7 (days 1997 088 to 1997 102); C9 (days 1997 255 to 1997 269) and G28 (days 2000 141 to 2000 149). Indicated in the bottom of each panel are day of the year, radial distance (in R_J) and local time (in hrs).

5 Summary and conclusions

Based on 33 orbits of the Galileo spacecraft the properties of the energetic charged population in the inner part of the Jovian magnetosphere were investigated. The extended coverage of the Jovian magnetosphere provided by Galileo, made it possible to perform a comprehensive topological study of the particle population, in terms of radial distance, local time, and System III dependence.

The focus of this thesis was on the region where the overall morphology of the Jovian magnetosphere alters its characteristics distinctively. This region is located at distances from $10 R_J$ to $30 R_J$ away from the planet. From all the particle parameters which were analysed, the most distinct changes occur in the energy spectra of ions and the pitch angle distribution of electrons. The spectrum of protons, and other ions species changes from a hard spectrum, at distances smaller than $10 R_J$, to a softer spectrum outside of $20 R_J$, indicating that a smaller fraction of high energy particles is present. This change reflects the magnetic field transition from a close to dipolar configuration, where the particles, even the energetic ones, are stably trapped, to a current sheet/magnetotail configuration, where the more energetic particles are preferentially lost.

The electron pitch angle distribution (PAD) develops from a pancake to a field-aligned distribution. This change is typically observed for radial distances of $10 R_J$ to $17 R_J$ from the planet. But on each individual orbit it occurs within the 11-min measurement interval of the energetic particle detector, thus establishing a well defined boundary.

In the second part of this work a possible explanation for the distinct pitch angle boundary and the relation to the secondary auroral oval was discussed. The secondary oval is a discrete belt of auroral emissions observed equatorward of the main auroral oval. The pronounced change from a pancake distribution towards smaller pitch angles reflects an enhanced ionospheric precipitation flux, which means that observable effects, in the form of auroral emissions, could be associated with the PAD boundary. This was confirmed by using magnetic field models to trace the field lines threading the PAD boundary (between $10 R_J$ and $17 R_J$) in the equatorial plane, into the ionosphere. The results show a good correlation with the secondary oval.

To study the physical processes causing the change from a bi-directional to a pancake distribution, a simulation of the electron pitch angle evolution with radial distance assuming conservation of the first and second adiabatic invariants was developed. The simulation showed that conserving the first and second adiabatic invariants, leads an electron population with a bi-directional PAD in the current sheet region into a pancake distribution in the dipolar region.

The scattering of particles by whistler waves was considered as the most likely mechanism for the enhancement of the precipitation flux. To verify the conditions for the existence of whistler waves in the region of the magnetosphere where the PAD boundary

occurs, the critical flux for wave instability was calculated and compared with the measured electron flux in the PAD boundary region. It was shown that the free energy present in the electron distribution is sufficient to cause whistler wave instability.

The presence of whistler waves was confirmed by the plasma wave instrument on board Galileo. Using the measured wave parameters the pitch angle diffusion coefficient was estimated and compared with the strong diffusion coefficient. It was shown that the conditions for strong diffusion are satisfied. The calculation of the energy precipitation flux in the PAD boundary region, with strong diffusion, gives a brightness range of 32 kR to 320 kR, which is comparable to the brightness values of the secondary auroral oval emissions. Furthermore, since the PAD boundary occurs over a narrow range in the equatorial plane (as observed in the measurements and in the simulation), it is likely to be associated with a narrow discrete belt of auroral emissions.

By showing that the observed electron pitch angle distribution is obtained by conservation of the first and second adiabatic invariants, and that the presence of whistler waves leads to scattering and precipitation of particles, this thesis has also confirmed an essential part of the Nishida model as a global model for particle transport and acceleration in the Jovian magnetosphere.

The work done in this thesis established for the first time the electron PAD boundary as a persistent feature of the Jovian magnetosphere occurring in a relatively narrow distance range. It showed the importance of the electron pitch angle changes in the equatorial plane for the global transport of particles in the Jovian magnetosphere and source region of the secondary auroral oval emissions.

A Charged particle motion in a magnetosphere

The charged particle population, electrons and ions, in the Jovian magnetosphere is influenced by the electric (\mathbf{E}) and magnetic (\mathbf{B}) fields. The motion of charged particles in electromagnetic field is governed by the Maxwell equations and the Lorentz force, according to *Roederer (1970), Walt (1994)*:

$$\nabla \cdot \mathbf{E} = \frac{\rho}{\varepsilon_0} \quad (\text{A.1})$$

$$\nabla \times \mathbf{B} = \mu_0 \mathbf{J} + \mu_0 \varepsilon_0 \frac{\partial \mathbf{E}}{\partial t} \quad (\text{A.2})$$

$$\nabla \times \mathbf{E} = -\frac{\partial \mathbf{B}}{\partial t} \quad (\text{A.3})$$

$$\nabla \cdot \mathbf{B} = 0 \quad (\text{A.4})$$

where ρ is the charge density, \mathbf{J} is the current density and ε_0, μ_0 are the electric permittivity and the magnetic permeability respectively.

The Lorentz force (in the non-relativistic form) is:

$$\mathbf{E} = \frac{d\mathbf{p}}{dt} = (q\mathbf{E} + \mathbf{v} \times \mathbf{B}) \quad (\text{A.5})$$

with \mathbf{p} the momentum of the particle, \mathbf{v} the velocity and q the charge. Separating the particle motion into two components, parallel and perpendicular to the magnetic field (according to *Walt (1994)*) the equation A.5 can be rewritten:

$$\begin{aligned} \left(\frac{d\mathbf{p}}{dt}\right)_{\parallel} &= q\mathbf{E}_{\parallel} \\ \left(\frac{d\mathbf{p}}{dt}\right)_{\perp} &= q(\mathbf{E}_{\perp} + \mathbf{v} \times \mathbf{B}) \end{aligned} \quad (\text{A.6})$$

Assuming a uniform magnetic field \mathbf{B} constant, and $\mathbf{E} = 0$ and , the above equations become:

$$\begin{aligned} \left(\frac{dp}{dt}\right)_{\parallel} &= 0 \\ \left(\frac{dp}{dt}\right)_{\perp} &= q(\mathbf{v} \times \mathbf{B}) \end{aligned} \quad (\text{A.7})$$

This indicates that p_{\parallel} is constant, which means that the particle is moving parallel to the magnetic field at constant speed. Since the centrifugal force must balance the Lorentz force:

$$m \frac{v_{\perp}^2}{\rho_c} = q v_{\perp} B \quad (\text{A.8})$$

This equation allows to determine the radius of the particle trajectory, known as gyroradius, cyclotron or Larmor radius (ρ_c), $\rho_c = \frac{m v_{\perp}}{q B}$. The gyrofrequency is given by: $\Omega = \frac{q B}{m}$.

The motion of the particle is the result of a circular motion superimposed on a parallel motion to the magnetic field, which results in a helicoidal movement. The angle between the particle velocity and the magnetic field is called the pitch angle:

$$\alpha = \arctan \left(\frac{v_{\perp}}{v_{\parallel}} \right)$$

A.1 The guiding center approximation

When the magnetic fields are not homogeneous, which is the case in planetary magnetospheres, the solution to the Lorentz equation is not easily reached, and numerical approximations and/or a simplified description are considered. One of these descriptions is the guiding center approximation.

As it was shown the Lorentz force leads to a helicoidal motion of the particle around the magnetic field, with a certain frequency Ω and a certain radius ρ_c ¹. In the guiding center approximation, a frame of reference is considered where the motion of the particle around the field line is circular. The centre of this trajectory is called the guiding centre.

In this way one considers the motion of the particle around the guiding centre and the motion of the guiding centre itself. The position of a particle is given by: $\mathbf{r} = \mathbf{R} + \boldsymbol{\rho}$. In order to find the equations of motion of the guiding centre, one expands the magnetic field in the vicinity of \mathbf{R} in a Taylor series:

$$\mathbf{B}(\mathbf{r}) = \mathbf{B}(\mathbf{R}) + \boldsymbol{\rho} \cdot \nabla \mathbf{B}(\mathbf{R}) + \dots \quad (\text{A.9})$$

where $\boldsymbol{\rho} \cdot \nabla \mathbf{B} = \left(\rho_x \frac{\partial}{\partial x} + \rho_y \frac{\partial}{\partial y} + \rho_z \frac{\partial}{\partial z} \right) \mathbf{B}$

Since we are considering $\mathbf{E} = 0$ the equation of motion becomes:

$$m(\ddot{\mathbf{R}} + \ddot{\boldsymbol{\rho}}) = q(\dot{\mathbf{R}} + \dot{\boldsymbol{\rho}}) \times [\mathbf{B}(\mathbf{R}) + \boldsymbol{\rho} \cdot \nabla \mathbf{B}(\mathbf{R}) + \dots] \quad (\text{A.10})$$

It is assumed that $\rho \left(\frac{|\nabla \mathbf{B}|}{B} \right) \ll 1$ which allows to neglect the higher order terms of \mathbf{B} . In the appropriate coordinate system indicated in the figure A.1, where $(\mathbf{e}_1, \mathbf{e}_2, \mathbf{e}_3)$ are unit vectors forming an orthogonal system. The gyroradius of the particle is defined as follows:

$$\boldsymbol{\rho} = \rho(e_2 \sin \Omega t + e_3 \cos \Omega t) \quad (\text{A.11})$$

¹To simplify the notation, ρ_c will be written as ρ

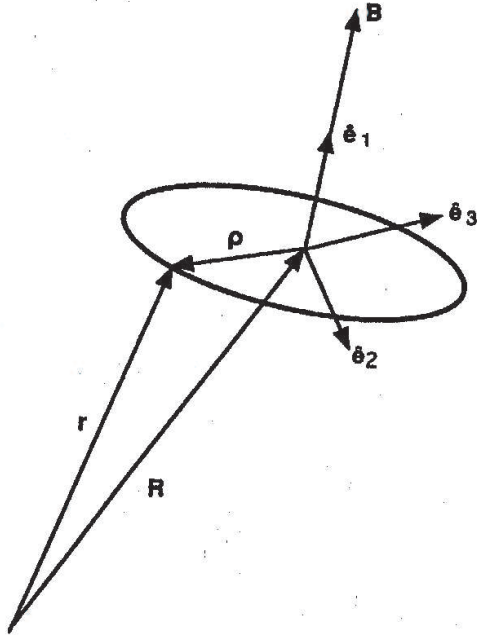


Figure A.1: Coordinate system for particle gyration in a inhomogeneous magnetic field.

This implies that: $\langle \rho \rangle = \langle \dot{\rho} \rangle = \langle \ddot{\rho} \rangle$, which allows for simplifications in the equation of motion that is averaged over time, i. e., integrated for a cyclotron period.

Using some vector algebra the equation of motion is reduced to :

$$m\ddot{\mathbf{R}} = q[\dot{\mathbf{R}} \times \mathbf{B}(\mathbf{R})] - q\frac{\rho^2\Omega}{2}\nabla B + \dots \quad (\text{A.12})$$

where B is the field magnitude.

It is useful to separate the equation of motion into its parallel and perpendicular forms.

The perpendicular component of the equation is given by :

$$\dot{\mathbf{R}}_{\perp} = \frac{m}{Bq}(e_1 \times \ddot{\mathbf{R}}) + \frac{\rho^2\Omega}{2B}e_1 \times \nabla B \quad (\text{A.13})$$

Considering s to be the distance measured along the field line, the perpendicular velocity, which is the drift velocity, can be obtained in terms of two drifts:

$$\dot{\mathbf{R}}_{\perp} = e_1 \times \left(\frac{mv_{\perp}^2}{2qB^2}\nabla B + \frac{m}{Bq}v_{\parallel}^2\frac{\partial e_1}{\partial s} \right) \quad (\text{A.14})$$

The first term is the gradient drift. As the particle is moving circularly, it will experience regions of stronger and weaker magnetic field with its gyroradius being smaller in large fields and bigger in small fields. This motion causes a drift in the perpendicular direction to \mathbf{B} and to the gradient of B , implying that the transport of particles is made along a line of constant B . Since it is dependent on the charge it means that negative and positive particles travel in opposite directions. The second term is the curvature drift. It reflects the effect of the curvature of the magnetic field lines in the particles trajectory. If the field line is curved the particle experiences a centrifugal force as it moves along the field line, which makes it drift perpendicular to the magnetic field and to the centrifugal

force. It is also charge dependent and therefore positive and negative particles travel in opposite directions.

The parallel component of the equation of motion (A.12) is given by:

$$\frac{dv_{\parallel}}{dt} = -\frac{1}{2} \frac{v_{\perp}^2}{B} (\nabla B)_{\parallel} \quad (\text{A.15})$$

This shows that the particle's parallel speed varies opposite to the magnetic field variation, decreasing when the magnetic field increases until it reaches a point (known as the magnetic mirror point) where it becomes zero and the particle reverses the direction until it reaches the opposite magnetic mirror point. The particle describes a bouncing motion between mirror points.

A.2 The adiabatic invariants

The derivation of the adiabatic invariants of motion is based in the notion from mechanics that the quantity which remains constant is called action and can be defined by the conjugate momentum \mathbf{p} and generalised coordinates \mathbf{q} :

$$J = \oint \mathbf{p} \cdot d\mathbf{q} \quad (\text{A.16})$$

The first adiabatic invariant is given by the following action integral (according to *Walt* (1994)):

$$J_1 = \oint [\mathbf{p} + q\mathbf{A}] \cdot d\mathbf{l} \quad (\text{A.17})$$

The integration is made for one gyroperiod, around the gyration orbit and $d\mathbf{l}$ is an element of the path of the particle. Using the Stokes theorem $\mathbf{B} = \nabla \times \mathbf{A}$, and remembering that the gyroradius is given by $\rho_c = \frac{v_{\perp}}{Bq}$ one obtains:

$$\begin{aligned} J_1 &= p_{\perp} \cdot 2\pi\rho_c + q \oint \mathbf{A} \cdot d\mathbf{l} \\ &= \frac{2\pi p_{\perp}^2}{Bq} - qB\pi\rho_c^2 \end{aligned} \quad (\text{A.18})$$

$$= \frac{\pi p_{\perp}^2}{qB} \quad (\text{A.19})$$

The first adiabatic invariant can be expressed in terms of the magnetic moment of the particle, and using the relation between the momentum and the kinetic energy of the particle (W_{\perp}) allows to obtain a very useful relation:

$$\mu = \frac{W_{\perp} \sin^2 \alpha}{B} \quad (\text{A.20})$$

This relation allows the determination of the pitch angle at any point along the field line, knowing the equatorial pitch angle and magnetic field (α_{eq}, B_{eq}), or the values at the mirror point (α_m, B_m):

$$\sin \alpha(s) = \sqrt{\frac{B(s)}{B_{eq}}} \sin \alpha_{eq} = \sqrt{\frac{B(s)}{B_m}} \quad (\text{A.21})$$

This equation also allows to define the nominal loss cone. The nominal loss cones are defined as the loss cone for each hemisphere $\alpha_{N,S}$ dependent on the magnitude of the magnetic field at the location in the equatorial plane where the particles originate B_{eq} and on the magnitude of the magnetic field at the location in the ionosphere where the particles precipitate $B_{N,S}$:

$$\sin^2 \alpha_{N,S} = \frac{B_{eq}}{B_{N,S}} \quad (\text{A.22})$$

The second adiabatic invariant is described by the following action integral (according to *Walt* (1994)):

$$\begin{aligned} J_2 &= \oint [\mathbf{p} + q\mathbf{A}] \cdot d\mathbf{l} \\ &= \oint \mathbf{p} ds = \oint p_{\parallel} ds \end{aligned} \quad (\text{A.23})$$

where ds is an element of length along the field line.

The action integral associated with the third adiabatic invariant is:

$$\begin{aligned} J_3 &= \oint [\mathbf{p} + q\mathbf{A}] \cdot d\mathbf{l} \\ &= q \oint (\nabla \times \mathbf{A}) \cdot d\mathbf{S} \end{aligned} \quad (\text{A.24})$$

Here $d\mathbf{S}$ is an element of the drift surface. Taking the Stokes theorem into consideration:

$$J_3 = q \oint \mathbf{B} \cdot d\mathbf{S} = q\Phi \quad (\text{A.25})$$

B Galileo instruments and associated principal investigators

B Galileo instruments and associated principal investigators

Instrument	Principal Investigator	Study objectives
Remote Sensing		
SSI	Michael Belton National Optical Astronomy Observatories	Galilean satellites, high resolution, atmospheric small-scale dynamics
NIMS	Robert Carlson Jet Propulsion Laboratory	Surface/atmospheric composition thermal map- ping
PPR	James Hansen Goddard Institute for Space Studies	Atmospheric particles thermal/reflected radiation
UVS/EUV	Charles Hord University of Colorado	Atmospheric gases, aerosols, etc.
Fields and Particles		
MAG	Margaret Kivelson University of California Los Angeles	Strength and fluctuations of magnetic fields
EPD	Donald Williams Johns Hopkins Applied Physics Laboratory	Electrons, protons, heavy ions
PLS	Lou Frank University of Iowa	Composition, energy distribution of ions
PWS	Donald Gurnett University of Iowa	Electromagnetic waves and wave-particle interactions
DDS	Eberhard Grün Max Planck Institut für Kernphysik	Mass, velocity, charge of submicrometer particles
Eng. Experiment		
HIC	Edward Stone California Institute of Technology	Spacecraft charged-particle environment
Radio Science		
Celestial Mechanics	John Anderson Jet Propulsion Laboratory	Masses and internal structures of bodies from s/c tracking
Propagation	H. Taylor Howard Stanford university	Satellite radii and atmospheric structure from radio propagation

Table B.1: Galileo Orbiter instruments and the associated principal investigators

C Record mode coverage

Orbit	Date
G2	1996 250, 1996 255
C3	1996 309, 1996 310
E4	1996 354
E6	1997 051, 1997 089
G7	1997 095
G8	1997 126, 1997 127
C9	1997 176, 1997 179, 1997 219, 1997 235
C10	1997 259, 1997 260, 1997 261
E11	1997 310
E12	1997 350
E14	1998 088
E15	1998 151
E19	1999 032
C20	1999 123
C21	1999 182, 1999 183
C22	1999 224
C23	1999 257, 1999 284
I25	1999 329
E26	2000 003
I27	2000 053
G28	2000 141
G29	2000 363
C30	2001 145
I31	2001 218
I32	2001 288
A34	2002 309

Table C.1: Record mode data coverage in the 40 R_J radial range, considered in this work. The format is "day of year".

D Jovian magnetic field models

The O4 internal field model

The internal field model GSFC O4 is based on magnetic field measurements by the flux gate magnetometer experiment on Pioneer 11 and it makes use of spherical harmonics analysis in its description. The magnetic field is considered to be the gradient of a scalar potential which combines both internal and external sources.

$$\mathbf{B} = -\nabla(V^e + V^i) \quad (\text{D.1})$$

Expressing the potential in terms of spherical harmonics gives:

$$V = a \sum_{n=1}^{\infty} \left\{ \left(\frac{r}{a} \right)^n T_n^e + \left(\frac{a}{r} \right)^{n+1} T_n^i \right\} \quad (\text{D.2})$$

Where r is the distance from the planet and a is the planet radius, and:

$$\begin{aligned} T_n^i &= \sum_{m=0}^n P_n^m(\cos \theta) [g_n^m \cos m\phi + h_n^m \sin m\phi] \\ T_n^e &= \sum_{m=0}^n P_n^m(\cos \theta) [G_n^m \cos m\phi + H_n^m \sin m\phi] \end{aligned} \quad (\text{D.3})$$

Here θ is the colatitude and ϕ the system III longitude. $P_n^m(\theta)$ are the associated Schmidt normalised Legendre functions and g_n^m, h_n^m and G_n^m, H_n^m the internal and external Schmidt coefficients respectively.

The O4 model has significant quadrupole and octupole moments which are appropriate to describe the structure of the field and its effects on the motion of trapped particles in the inner Jovian magnetosphere.

The current sheet

The current sheet is represented by an annular current sheet of finite extent. The coordinate system used is the magnetic equatorial cylindrical with $\hat{\rho}$ and $\hat{\phi}$ in the equatorial plane and \hat{z} parallel to the dipole axis. In the current sheet region the model assumes that only azimuthal currents are present, which means that the vector potential only has a component in $\hat{\phi}$, in this case the magnetic field is given by:

$$\mathbf{B} = \nabla \times A(\rho, z)\hat{\phi} = -\frac{\partial A}{\partial z}\hat{\rho} + \frac{1}{\rho}\frac{\partial}{\partial \rho}(\rho A)\hat{z} \quad (\text{D.4})$$

The solutions for the vector potential A can be found, considering the curl of B to be zero in a current free region, which obeys the equation:

$$-\frac{\partial^2 A}{\partial z^2} + \frac{A}{\rho^2} - \frac{1}{\rho} \frac{\partial A}{\partial \rho} - \frac{\partial^2 A}{\partial \rho^2} = 0 \quad (\text{D.5})$$

The solutions are of the type:

$$A^\pm = \int_0^\infty C(\lambda) J_1(\lambda \rho) e^{\mp \lambda z} d\lambda \quad (\text{D.6})$$

With the upper sign for $z < 0$ and the lower sign for $z > 0$. $J_1(\lambda \rho)$ is given by the solution to the Bessel equation resulting from D.5, and $C(\lambda)$ is determined in order to satisfy boundary conditions resulting from the reversal of B_ρ across the current sheet:

$$\left. \frac{\partial A^+}{\partial z} \right|_{z=0} = \left. \frac{\partial A^-}{\partial z} \right|_{z=0} - \mu_0 I(\rho) \quad (\text{D.7})$$

The current sheet geometry is chosen to be that of an annular current sheet starting at $R_0 = 5 R_J$ and ending at $R_1 = 50 R_J$, with a half thickness of $D = 2.5 R_J$. In this way the surface current density, $I(\rho)$ (at $z = 0$), for the different regions is given by:

$$\begin{aligned} I(\rho) &= 0 & \rho < R_0 \\ I(\rho) &= I_0 & R_0 < \rho < R_1 \\ I(\rho) &= 0 & \rho > R_1 \end{aligned} \quad (\text{D.8})$$

The solutions for the vector potential and for the magnetic field components can be found by analytical integration under certain simplifications and assuming a thin current sheet. The field is modeled in three different regions:

Region I considers values of $\rho < R_0$:

$$\begin{aligned} B_\rho^I &= \left(\frac{\mu_0 I_0}{2} \right) \frac{\rho}{2} [1/F_1 - 1/F_2] \\ B_z^I &= \left(\frac{\mu_0 I_0}{2} \right) \left[\frac{2D}{(z^2 + R_0^2)^2} - \frac{\rho^2}{4} \left(\frac{z-D}{F_1^3} - \frac{z+D}{F_2^3} \right) \right] \end{aligned} \quad (\text{D.9})$$

where,

$$\begin{aligned} F_1 &= [(z-D)^2 + R_0^2]^{1/2} \\ F_2 &= [(z+D)^2 + R_0^2]^{1/2} \end{aligned} \quad (\text{D.10})$$

Region II considers values of $\rho > R_0$ and values of $z > D$, which means for the exterior of the current sheet:

$$\begin{aligned} B_\rho^{II} &= \left(\frac{\mu_0 I_0}{2} \right) \left[\frac{1}{\rho} (F_1 - F_2 + 2D) - \frac{R_0^2 \rho}{4} \left(\frac{1}{F_1^3} - \frac{1}{F_2^3} \right) \right] \\ B_z^{II} &= \left[2D(z^2 + \rho^2)^{-1/2} - \frac{R_0^2}{4} \left(\frac{z-D}{F_1^3} - \frac{z+D}{F_2^3} \right) \right] \end{aligned} \quad (\text{D.11})$$

Region III considers the field in the interior of the current sheet, for both positive and negative z . In this case B_z^{III} is considered to be equal to B_z^{II} and B_ρ^{III} is given by:

$$B_\rho^{III} = \left(\frac{\mu_0 I_0}{2} \right) \left[\frac{1}{\rho} (F_1 - F_2 + 2z) - \frac{R_0^2 \rho}{4} \left(\frac{1}{F_1^3} - \frac{1}{F_2^3} \right) \right] \quad (\text{D.12})$$

The model showed that due to the current sheet the magnetic field lines are stretched in the magnetic equatorial plane and the field is mainly radial at distances larger than 15 R_J both above and below the current sheet. The current sheet was taken to be, in a first approximation, cylindrically symmetric with deviations from symmetry occurring in the dayside. The radial dependence of the current density is $\sim 1/\rho$. The model also showed that the inner boundary of the current sheet was extended up to the orbit of Io. One of the big advances of the model was the enlargement of the auroral zone which at the time caused some questions as to the interpretation of the auroral emission sources. This problem was better constrained in subsequent work by *Connerney et al.* (1998) which constitutes the current VIP 4 model, in use in this work. The model uses the observations of the Io footprint (both H_3^+ and ultraviolet emissions) and magnetic field in-situ measurements to improve the previous version. The resulting magnetic field which combines the O4 internal field model plus a current sheet (described above) and observational constraints can be of use to better explain a variety of phenomena related to the magnetospheric region up to 30 R_J . The VIP 4 model is currently considered to be the state of the art in magnetic field models (up to 30 R_J) and field line mapping from the equatorial plane to Jupiter's ionosphere.

The Khurana model for the Jovian magnetic field developed by *Khurana* (1997) uses the GSFC O6 model for the internal field, and an Euler potential formulation for the external field.

The internal field O6 model

The O6 internal field model described by *Connerney* (1992) uses the same spherical harmonics analysis previously used in the GSFC O4 model to describe the magnetic field due to the internal field of the planet.

In this model both Pioneer 11 (1974) and Voyager 1 (1979) measurements are considered. The parameters are comparable to those of the O4 model with the biggest exceptions being found for the octupole terms. The Schmidt normalised coefficients in use for both models are indicated in table D.1

The overall result is the derivation of a more "Earth-like" model than the one obtained by the O4 model.

Current sheet structure

In order to accurately describe the external field in the Jovian magnetosphere the Khurana model considers the complex structure of the Jovian current sheet and the plasma outflow from Io which generates radial and field aligned currents.

The Khurana model makes use of a hinged-magnetodisc description for the current sheet structure (*Khurana* 1992), which explains the observed delay. The hinging is due to solar wind forcing.

Schmidt coeffi cient	VIP 4	GSFC O6
g_1^0	4.205	4.242
g_1^1	-.659	-.659
h_1^1	0.250	0.241
g_2^0	-.051	-.022
g_2^1	-.619	-.711
g_2^2	0.497	0.487
h_2^1	-.361	-.403
h_2^2	0.053	0.072
g_3^0	-.016	0.075
g_3^1	-.520	-.155
g_3^2	0.244	0.198
g_3^3	-.176	-.180
h_3^1	-.088	-.388
h_3^2	0.408	0.342
h_3^3	-.316	-.224
g_4^0	-.168	
g_4^1	0.222	
g_4^2	-.061	
g_4^3	-.202	
g_4^4	0.066	
h_4^1	0.076	
h_4^2	0.404	
h_4^3	-.166	
h_4^4	0.039	

Table D.1: Schmidt normalised spherical harmonic coeffi cients, in reference to Jupiter SIII coordinates for the VIP 4 and O6 models.

The important parameter is the distance of the current sheet Z_{cs} to the Jovigraphic equator, considering the distance x of the spacecraft (in the Jupiter-Sun-Orbital plane) and a ρ dependence to the wave velocity. In these conditions Z_{cs} for a radial distance of ρ_{III} and at a certain longitude λ (in left-handed system III longitude) is given by:

$$Z_{cs} = \rho_{III} \tan(9.6^\circ) \frac{x_0}{x} \tanh\left(\frac{x}{x_0}\right) \cos(\lambda - \delta) \quad (\text{D.13})$$

where x_0 is the hinge distance of the current sheet. The longitude δ towards which the current sheet has the maximum tilt θ_{cs}^1 depends on the angular velocity of the planet Ω_J , on the asymptotic value of the wave velocity v_0 and on the distance ρ_0 beyond which the propagation delay is signifi cant , according to:

$$\delta = 22^\circ + \frac{\Omega_J \rho_0}{v_0} \ln \cosh\left(\frac{\rho_{III}}{\rho_0}\right) \quad (\text{D.14})$$

¹For a dipole fi eld $\delta = 22^\circ$ and $\theta_{cs} = 9.6^\circ$

Using these equations both the hinging of the current sheet and the wave delay are modeled.

The coordinate system used in the computation is the magnetic dipole coordinate system (ρ, φ, Z) , with the Z axis aligned with the dipole axis, ρ the distance from the z axis and φ the azimuthal angle measured from the prime meridian ($\lambda = 202^\circ$).

In this case the equations D.13 and D.14 are rewritten:

$$Z_{cs} = \rho \tan(9.6^\circ) \left[\frac{x_0}{x} \tanh\left(\frac{x}{x_0}\right) \cos(\varphi - \delta) - \cos(\varphi - \pi) \right] \quad (\text{D.15})$$

$$\delta = \pi - \frac{\Omega_J \rho_0}{v_0} \ln \cosh\left(\frac{\rho}{\rho_0}\right) \quad (\text{D.16})$$

The current sheet obtained is aligned with the dipole equator up to $30 R_J$ and afterwards it deviates towards the Jovigraphic equator.

External field model

In the Khurana model the external field of Jupiter is described by an Euler potential formulation. This means that the magnetic field is expressed by two scalar functions, which are constant along a field line:

$$B = \nabla f \times \nabla g \quad (\text{D.17})$$

The functions are considered to be dependent on the three variables of the magnetic dipole coordinate system (ρ, φ, Z) , which gives for the field components:

$$\begin{aligned} B_\rho &= \frac{\partial f}{\rho \partial \varphi} \frac{\partial g}{\partial Z} - \frac{\partial f}{\partial Z} \frac{\partial g}{\rho \partial \varphi} \\ B_\varphi &= \frac{\partial f}{\partial Z} \frac{\partial g}{\partial \rho} - \frac{\partial f}{\partial \rho} \frac{\partial g}{\partial Z} \\ B_Z &= \frac{\partial f}{\partial \rho} \frac{\partial g}{\rho \partial \varphi} - \frac{\partial f}{\rho \partial \varphi} \frac{\partial g}{\partial \rho} \end{aligned} \quad (\text{D.18})$$

The forms of the functions f and g are chosen in agreement to previous works, but also in order to provide better fits to the observed data. The functions have the form $|\tanh(r_0/r)|^\alpha$. For large values of r the function assumes the form of a power law and for $r \ll r_0$ it approaches unity.

Although the Khurana model provides a description of the magnetosphere for distances greater than the VIP4 model, which means $> 30 R_J$, it does not accurately map the southern auroral oval. For this reason the VIP4 model was the preferred in this work.

Bibliography

- Acuña, M. H. and N. F. Ness, The main magnetic field of Jupiter. *J. Geophys. Res.*, 81, 2917, 1976 .
- Acuña, M. H., K. W. Behannon and J. P. Connerney, Jupiter's Magnetic field and magnetosphere. In: Dessler, A. J. (Ed.), *Physics of the Jovian magnetosphere*, Cambridge Univ. Press, Cambridge, 1-50, 1983.
- Balogh, A., M. K. Dougherty, R. J. Forsyth, D. J. Southwood, E. J. Smith, B. T. Tsurutani, N. Murphy and M. E. Burton, Magnetic field observation during the Ulysses flyby of Jupiter. *Science*, 257, 1515-1518, 1992.
- Bhardwaj, A. and G. R. Gladstone Auroral emissions of the Giant planets. *Rev. Geophys.*, 38, 295-353, 2000.
- Bhattacharya, B., R. M. Thorne, and D. J. Williams, On the energy source for diffuse Jovian auroral emissivity, *Geophys. Res. Lett.*, 14, 2751-2754, 2001.
- Broadfoot, A. L., M. J. S. Belton, P. Z. Takacs, B. R. Sandel, D. E. Shemansky, J. M. Holberg, J. M. Ajello, S. K. Atreya, T. M. Strobel, H. W. Moos, J. L. Bertaux, J. E. Blamont, D. F. Strobel, J. C. McConnell, A. Dalgarno, R. Goody and M. B. McElroy, Extreme ultraviolet observations from Voyager 1 encounter with Jupiter. *Science*, 204, 979-982, 1979.
- Burke, B. F. and K. L. Franklin, Observations of a variable radio source associated with the planet Jupiter. *J. Geophys. Res.*, 60, 213, 1955.
- Carr, T. D. and S. Gulkis, The magnetosphere of Jupiter. *Ann. Rev. Astron. Astrophys.*, 7, 577-618, 1969.
- Clarke, J. T., J. Ajello, J. Ballester, L. B. Jaffel, J. E. P. Connerney, J.-C. Gérard, G. R. Gladstone, D. Grodent, W. Pryor, J. Trauger and J. H. Waite, Ultraviolet auroral emissions from the magnetic footprints of Io, Ganymede and Europa on Jupiter. *Nature*, 415, 997-1000, 2002.
- Clarke, J. T., D. Grodent, S. W. H. Cowley, E. J. Bunce, P. Zarka, J. E. P. Connerney and T. Satoh, Jupiter's aurora, In: Bagenal, F., T. Dowling, W. Mckinnon (Eds.), *Jupiter: The Planet, Satellites and Magnetosphere*, Cambridge Planet. Science, Cambridge, 639-670, 2004.

- Connerney, J. E. P., M. H. Acuña and N. F. Ness, Modeling the Jovian current sheet and inner magnetosphere. *J. Geophys. Res.*, 86, 8370-8384, 1981.
- Connerney, J. E. P., Doing more with Jupiter's magnetic field. In: Ruecker, H. O., Bauer, S. J., Kaiser, M. L. (Ed.), *Planetary radio emissions III*, Osterreichischen Akad. der Wiss., Vienna, 13-33, 1992.
- Connerney, J. E. P., R. L. Baron, T. Satoh and T. Owen, Images of excited H_3^+ at the foot of the Io flux tube in Jupiter's atmosphere. *Science*, 262, 1035-1038, 1993.
- Connerney, J. E. P., M. H. Acuña, N. F. Ness and T. Satoh, New models of Jupiter's magnetic field constrained by the Io flux tube footprint. *J. Geophys. Res.*, 103, 11 929-11 939, 1998.
- Cowley, S. W. H. and E. J. Bunce, Origin of the main auroral oval in Jupiter's coupled magnetosphere-ionosphere system. *Planet. Space Sci.*, 49, 1067-1088, 2001.
- Dougherty, M. K., D. J. Southwood, A. Balogh and E. J. Smith, Field-aligned currents in the Jovian magnetosphere during the Ulysses fly-by. *Planet. Space Sci.*, 41, 291-300, 1993.
- Drossart, P., J. P. Maillard, J. Cladwell, S. J. Kim, J. K. G. Watson, W. A. Majewski, J. Tennyson, S. Miller, S. K. Atreya, J. Clarke, J. H. Waite Jr. and R. Wagoner, Detection of H_3^+ on Jupiter. *Nature*, 340, 539-541, 1989.
- Fillius, W., The trapped radiation belts of Jupiter. In: Gehrels, T (Ed.), *Jupiter - Studies of the interior, atmosphere, magnetosphere and satellites*, The Univ. of Arizona Press, Tucson, Arizona, 896-927, 1976.
- Fujimoto, M. and A. Nishida, Monte Carlo simulation of energization of Jovian trapped electrons by recirculation. *J. Geophys. Res.*, 95, 3841-3853, 1990.
- Gérard, J.-C., J. Gustin, D. Grodent, P. Delamere and J. T. Clarke, Excitation of the FUV Io tail on Jupiter: characterization of the electron precipitation. *J. Geophys. Res.*, 107, 2002.
- Goertz, C.K., Jupiter's Magnetosphere: Particles and fields. In: Gehrels, T. (Ed.), *Jupiter - Studies of the interior, atmosphere, magnetosphere and satellites*, The Univ. of Arizona Press, Tucson, Arizona, 32-58, 1976.
- Goertz, C. K. and M. F. Thomsen, The dynamics of the Jovian magnetosphere. *Rev. Geophys. and Space Phys.*, 17, 731-743, 1979.
- Grodent, D., J. H. Waite Jr., and J. C. Gérard, A self-consistent model of the Jovian auroral thermal structure. *J. Geophys. Res.*, 106, 12 933-12 952, 2001.
- Grodent, D., J. T. Clarke, J. Kim, J. H. Waite Jr., S. W. H. Cowley, Jupiter's main auroral oval observed with HST-STIS. *J. Geophys. Res.*, 108(A11), 1389, doi:10.1029/2003JA009921, 2003.

- Gurnett, D. A. and F. L. Scarf, Plasma Waves in the Jovian Magnetosphere. In: Dessler, A. J. (Ed.), *Physics of the Jovian magnetosphere*, Cambridge Univ. Press, Cambridge, 285-316, 1983.
- Gurnett, D. A., W. S. Kurth, R. R. Shaw, A. Roux, R. Gendrin, C. F. Kennel, F. L. Scarf and S. D. Shawhan, The Galileo plasma wave investigation. *Space Sci. Rev.*, 60, 341-355, 1992.
- Hamilton, D. C., G. Gloeckler, S. M. Krimigis, C. O. Bostrom, T. P. Armstrong, W. I. Axford, C. Y. Fan, L. J. Lanzerotti and D. M. Hunten, Detection of energetic hydrogen molecules in Jupiter's magnetosphere by Voyager 2 - Evidence for an ionospheric plasma source., *Geophys. Res. Lett.*, 7, 813-816, 1980.
- Hamilton, D. C., G. Gloeckler, S. M. Krimigis and L. J. Lanzerotti, Composition of non-thermal ions in the Jovian magnetosphere. *J. Geophys. Res.*, 86, 8301-8318, 1981.
- Hill, T. W., A. J. Dessler and C. K. Goertz, Magnetospheric models. In: Dessler, A. J. (Ed.), *Physics of the Jovian magnetosphere*, Cambridge Univ. Press, Cambridge, 353-394, 1983.
- Hill, T. W., The Jovian auroral oval. *J. Geophys. Res.*, 106, 8101-8107, 2001.
- Hill, T. W., Auroral structures at Jupiter and Earth. *Adv. Space Res.*, 33, 2021-2029, 2004.
- Kennel, C. F. and H. E. Petschek, Limit on stably trapped particle fluxes. *J. Geophys. Res.*, 71, 1-28, 1966.
- Kennel, C. F. and F. V. Coroniti, Jupiter's Magnetosphere. *Ann. Rev. Astron. Astrophys.*, 15, 389-436, 1977.
- Khurana, K. K., A generalized hinged-magnetodisc model of Jupiter's nightside current sheet. *J. Geophys. Res.*, 97, 6269-6276, 1992.
- Khurana, K. K., Euler potential models of Jupiter's magnetospheric field. *J. Geophys. Res.*, 102, 11 295-11 306, 1997.
- Khurana, K. K., M. G. Kivelson, V. M. Vasylunas, Krupp, N., J. Woch, A. Lagg, B. H. Mauk and W. S. Kurth, The Configuration of Jupiter's magnetosphere, In: Bagenal, F., T. Dowling, W. Mckinnon (Eds.), *Jupiter: The Planet, Satellites and Magnetosphere*, Cambridge Planet. Science, Cambridge, 593-616, 2004.
- Kivelson, M. G., K. K. Khurana, J. D. Means, C. T. Russel and R. C. Snare, The Galileo Magnetic field investigation. *Space Sci. Rev.*, 60, 357-383, 1992.
- Kivelson, M. G., K. K. Khurana, C. T. Russel, R. J. Walker, J. Warnecke, F. V. Coroniti, C. Polanskey, D. J. Southwood, and G. Schubert, Discovery of Ganymede's magnetic field by the Galileo spacecraft. *Nature*, 384, 537-541, 1996.
- Kivelson, M. G. and K. K. Khurana, Properties in the magnetic field in the Jovian magnetotail. *J. Geophys. Res.*, 107, 1196, doi: 10.1029/2001JA000249, 2002.

- Krimigis, S. M., T. P. Armstrong, W. I. Axford, C. O. Bostrom, C. Y. Fan, G. Gloeckler, L. J. Lanzerotti, E. P. Keath, R. D. Zwickl and D. C. Hamilton, Low-energy charged particle environment at Jupiter: A first look. *Science*, 204, 998-1003, 1979.
- Krimigis, S. M., J. F. Carbary, E. P. Keath, C. O. Bostrom, W. I. Axford, G. Gloeckler, L. J. Lanzerotti and T. P. Armstrong, Characteristics of Hot Plasma in the Jovian Magnetosphere: Results from the Voyager Spacecraft. *J. Geophys. Res.*, 86, 8227-8257, 1981.
- Krimigis, S. M. and E. C. Roelof, Low energy particle population. In: Dessler, A. J. (Ed.), *Physics of the Jovian magnetosphere*, Cambridge Univ. Press, Cambridge, 106-156, 1983.
- Kronberg, E., J. Woch, N. Krupp, A. Lagg, K. K. Khurana and K.-H. Glassmeier, Mass release at Jupiter - substorm-like processes in the Jovian magnetotail. *J. Geophys. Res.*, accepted for publication, 2005.
- Krupp, N., E. Keppler, R. Seidel, J. Woch, A. Korth, A. F. Cheng, S. E. Hawkins III, L. J. Lanzerotti, C. G. MacLennan and M. K. Dougherty, Field-aligned particle streaming in the darkside high latitude Jovian magnetosphere. *Adv. Space Res.*, 20, 225-228, 1997.
- Krupp, N., J. Woch, A. Lagg, B. Wilken, S. Livi and D. J. Williams, Energetic particle bursts in the predawn Jovian magnetotail. *J. Geophys. Res.*, 25, 1249-1252, 1998.
- Krupp, N., E. Roelof, J. Woch, D. J. Williams, A. Lagg, B. Wilken and S. Livi, Global flows of energetic ions in Jupiter's equatorial plane: First-order approximation. *J. Geophys. Res.*, 106(A11), 26 017-26 032, 2001.
- Krupp, N., J. Woch, A. Lagg, S. A. Espinosa, S. Livi, S. M. Krimigis, D. G. Mitchell, D. J. Williams, A. F. Cheng, B. H. Mauk, R. W. McEntire, T. P. Armstrong, D. C. Hamilton, G. Gloeckler, J. Dandouras and L. J. Lanzerotti, Leakage of energetic particles from Jupiter's dusk magnetosphere: Dual spacecraft Observations. *Geophys. Res. Lett.*, 29, 10.1029/2001GL014290, 2002.
- Krupp, N., V. M. Vasyliūnas, J. Woch, A. Lagg, K. K. Khurana, M. G. Kivelson, B. H. Mauk, E. C. Roelof, D. J. Williams, S. M. Krimigis, W. S. Kurth, L. A. Frank and W. R. Paterson, Dynamics of the Jovian Magnetosphere, In: Bagenal, F., T. Dowling, W. Mckinnon (Eds.), *Jupiter: The Planet, Satellites and Magnetosphere*, Cambridge Planet. Science, Cambridge, 617-638, 2004
- Krupp, N., J. Woch, A. Lagg, S. Livi, D. G. Mitchell, S. M. Krimigis, M. K. Dougherty, P. G. Hanlon, T. P. Armstrong and S. A. Espinosa, Energetic particle observations in the vicinity of Jupiter: Cassini MIMI/LEMMS results, *J. Geophys. Res.*, 109, A09S10, doi:10.1029/2003JA010111, 2004.
- Lagg, A., J. Woch, N. Krupp and D. J. Williams, In-situ observations of a neutral gas torus at Europa. *Geophys. Res. Lett.*, 30, doi: 10.1029/2003GL017214, 2003.

- Lagg, A., *Energierreiche Teilchen in der inneren Jupitermagnetosphäre: Simulation und Ergebnisse des EPD-Experimentes an Bord der Raumsonde Galileo*. University of Innsbruck, Austria, 1998.
- Lanzerotti, L. J., T. P. Armstrong, R. E. Gold, K. A. Anderson, S. M. Krimigis, R. P. Lin, M. Pick, E. C. Roelof, E. T. Sarris, G. M. MacLennan, H. T. Choo and S. J. Tappin, The hot plasma environment at Jupiter: Ulysses results. *Science*, 257, 5118-1524, 1992.
- Morabito, L. A., S. P. Synnott, P. N. Kupferman and S. A. Collins Discovery of currently active extraterrestrial volcanism. *Science*, 204, 972, 1979.
- Ness, N. F., M. H. Acuña, R. P. Lepping, L. F. Burlaga, K. W. Behannon and F. M. Neubauer, Magnetic field studies at Jupiter by Voyager 1: Preliminary results. *Science*, 204, 982-987, 1979.
- Nishida, A., Outward diffusion of energetic particles from the Jovian radiation belt. *J. Geophys. Res.*, 81, 1771-1773, 1976.
- Opp, A. G., Pioneer 10 mission: Summary of scientific results from the encounter with Jupiter. *Science*, 183, 302-303, 1974.
- Opp, A. G., Scientific results from the Pioneer 11 mission to Jupiter. *Science*, 188, 447-448, 1975.
- Paranicas, C. P., A. F. Cheng, B. H. Mauk and S. M. Krimigis, Ion phase space densities in the Jovian magnetosphere. *J. Geophys. Res.*, 95, 20 833-20 838, 1990.
- Roberts, C. S., Pitch angle diffusion of electrons in the magnetosphere. *Rev. Geophys. Space Phys.*, 7, 305-337, 1969.
- Roederer, J. G., *Dynamics of geomagnetically trapped radiation*, Springer-Verlag, Berlin-Heidelberg, 1970.
- Russell C. T., The dynamics of planetary magnetospheres. *Planet. Space Sci.*, 49, 1005-1030, 2001.
- Scarf, F. L., D. A. Gurnett and W. S. Kurth, Jupiter Plasma Waves Observations: An initial Voyager 1 Overview. *Science*, 204, 991-998, 1979.
- Seidel, R., E. Keppler, N. Krupp, J. Woch, S. E. Hawkins, L. J. Lanzerotti and M. K. Dougherty, Energetic electron beams in the duskside Jovian magnetosphere: Ulysses EPAC and HI-SCALE measurements. *Planet. Space Sci.*, 45, 1474-1480, 1997.
- Smith, E. J., L. Davis Jr., E. D. Jones, D. S. Colburn, P. J. Coleman Jr., P. Dyal and C. P. Sonnet, Magnetic field of Jupiter and its interaction with the Solar Wind. *Science*, 183, 305-306, 1974.
- Sentman, D. D., J. A. Van Allen, C. K. Goertz, Recirculation of energetic particles in Jupiter's magnetosphere. *Geophys. Res. Lett.*, 2, 465-468, 1975.

- Smith, E. J., L. Davis Jr., E. D. Jones, P. J. Coleman Jr., D. S. Colburn, P. Dyal and C. P. Sonnet, Jupiter's Magnetic field, magnetosphere and interaction with the Solar Wind: Pioneer 11. *Science*, 188, 451-455, 1975.
- Smith, E. J., L. Davis Jr. and E.D. Jones, Jupiter's Magnetic field and magnetosphere. In: Gehrels, T. (Ed.), *Jupiter - Studies of the interior, atmosphere, magnetosphere and satellites*, The Univ. of Arizona Press, Tucson, Arizona, 788-829, 1976.
- Thomas, N., F. Bagenal, T. W. Hill, J. K. Wilson, The Io Neutral Clouds and Plasma Torus, In: Bagenal, F., T. Dowling, W. Mckinnon (Eds.), *Jupiter: The Planet, Satellites and Magnetosphere*, Cambridge Univ. Press, Cambridge, 561-591, 2004.
- Thorne, R. M. and B. T. Tsurutani, Diffuse Jovian aurora influenced by plasma injection from Io. *Geophys. Res. Lett.*, 6, 649-652, 1979.
- Thorne, R. M., Microscopic plasma processes in the Jovian magnetosphere. In: Dessler, A. J. (Ed.), *Physics of the Jovian magnetosphere*, Cambridge Univ. Press, Cambridge, 454-488, 1983.
- Tomás, A., J. Woch, N. Krupp, A. Lagg, K.-H. Glassmeier, M. K. Dougherty and P. G. Hanlon, Changes of the energetic particle characteristics in the inner part of the Jovian magnetosphere: a topological study. *Planet. Space Sci.*, 52, 491-498, 2004.
- Tomás, A., J. Woch, N. Krupp, A. Lagg, K.-H. Glassmeier and W. S. Kurth, Energetic electrons in the inner part of the Jovian magnetosphere and their relation to auroral emissions. *J. Geophys. Res.*, 109, A06203, doi:10.1029/2004JA010405, 2004.
- Van Allen, A. J., High-energy particles in the Jovian magnetosphere. In: Gehrels, T. (Ed.), *Jupiter - Studies of the interior, atmosphere, magnetosphere and satellites*, The Univ. of Arizona Press, Tucson, Arizona, 928-960, 1976.
- Vasyliūnas, V. M. , Plasma distribution and flow. In: Dessler, A. J. (Ed.), *Physics of the Jovian magnetosphere*, Cambridge Univ. Press, Cambridge, 395-453, 1983.
- Vogt, R. E., W. R. Cook, A. C. Cummings, T. L. Garrard, N. Gehrels, E. C. Stone, J. H. Trainor, A. W. Schardt, T. Conlon, N. Lal and F. B. McDonald , Voyager 1: Energetic Ions and Electrons in the Jovian Magnetosphere. *Science*, 204, 1003-1007, 1979.
- Voigt, G.-H., Magnetospheric configuration. In: Volland, H. (Ed.), *Handbook of Atmospheric Electrodynamics*, Vol. II, CRC Press, Boca Raton, Florida, 333-388, 1995.
- Walt, M., *Introduction to geomagnetically trapped radiation*, Cambridge University Press, Cambridge, 1994.
- Williams, D. J., R. W. McEntire, S. Jaskulek and B. Wilken, The Galileo Energetic Particles Detector. *Space Sci. Rev.*, 60, 385-412, 1992.
- Williams, D. J., Ganymede's ionic radiation belts. *Geophys. Res. Lett.*, 28, 3793-33796, 2001.

- Woch, J., N. Krupp, A. Lagg, B. Wilkin, S. Livi and D. J. Williams, Quase-periodic modulations of the Jovian magnetotail. *J. Geophys. Res.*, 25, 1253-1256, 1998.
- Woch, J., N. Krupp, K. K. Khurana, M. Kivelson, A. Roux, S. Perraut, P. Louarn, A. Lagg, D. J. Williams, S. Livi and B. Wilkin, Plasma sheet dynamics in the Jovian magnetotail: Signatures for substorm-like processes?. *Geophys. Res. Lett.*, 26, 2137-2140, 1999.
- Woch, J., N. Krupp, A. Lagg and A. Tomás, The structure and dynamics of the Jovian energetic particle distribution. *Adv. Space Res.*, 33, 2030-2038, 2004.

Acknowledgements

First of all I would like to thank my supervisors at the Max-Planck-Institut für Sonnensystemforschung, Joachim Woch and Norbert Krupp for their support and encouragement, your active and interested participation has made this work possible. I would like to thank you for giving me the opportunity to learn and work in a great environment full of ideas and time for discussions, where the glass is always half full and never half empty, your positive words even when things went wrong were a valuable incentive. I have learned many things and greatly enjoyed working with you in this three years. And to all the group, Joachim, Norbert, Andreas, Markus, Katerina, Elena and Luciano for all the interesting discussions and for making coffee breaks and meetings always a relaxed and fun time.

I would like to thank my supervisor at the Technische Universität Braunschweig, Prof. Dr. Karl-Heinz Glassmeier for the helpful ideas and for taking the time for discussing them, and for all the help getting through the bureaucratic system at the University.

Special thanks to Andreas Lagg for the EPD software, without which this work would not be possible, but above all for his patience in answering the multitude of questions which never seemed to stop. And for all the discussions and comments which greatly improved this work.

Many thanks also to Luciano Rodriguez for his contribution with the Ulysses EPAC data, and for all the help with IDL questions.

My thanks to the Director of the Institut Prof. Dr. Sami K. Solanki, to Prof. Dr. V. Vasyliūnas and to the IMPRS school, for the financing of my work and for the opportunity to make my PhD in a unique and stimulating environment. This work was also in part financed by the Bundesministerium für Bildung und Forschung (BMBF) through the Deutsches Zentrum für Luft-und-Raumfahrt e. V. (DLR) under Contract No. 50 ON 0201.

In particular I would like to thank the school coordinator, Dr. Dieter Schmidt for all the support and help, for organising all the seminars and retreats which gave the wonderful opportunity to learn and share so much, not only about science but also about people and the World.

This work is the result of a cooperation between different teams, I would like to thank the PI of the EPD instrument D. Williams, JHU/APL, the PI of the MAG instrument M. Kivelson, IGPP/UCLA and the PI of the PWS instrument D. Gurnett, Univ. of Iowa.

During this three years I had the opportunity to work with interesting and friendly people from different fields of research who had a valuable contribution to this work, helping to make it complete. Their availability to answer questions and to have stimulating discussions (even through email) has given me the opportunity to learn so many things and made this work particularly interesting. I would like to thank Dr. Michele K. Dougherty

and Paul G. Hanlon, Imperial College London, for their work with the magnetic field data; Dr. William S. Kurth, University of Iowa for his work with the wave data; Dr. John Clarke, University of Michigan and Dr. Denis Grodent, University of Liège for their work with the HST auroral data; Dr. Krishan K. Khurana, IGPP/UCLA for his contribution with the Khurana magnetic field model and Dr. Renee Prangé Observatory Paris-Meudon for her contribution with the VIP4 model.

I would like to thank Sybilla Siebert-Rust, Frau Fahlbusch and the late Frau Schrader, for their friendly support and precious help with all the paper work and practical questions which made life so much easier and simple.

To the friends I have found here in Lindau, who were there for me when I needed, who showed me that there is a time for everything, for solving work problems, computer problems, and most important life problems. Thank you! For all the talks and laughter and attempts at jogging...and a lot of great moments. Your friendship was essential in this three years and it will be cherished in the years to come.

Para os meus pais, para a minha família e para os meus amigos, que estão sempre ao meu lado. Pelo vosso amor e apoio incondicional, obrigada! Mesmo com muitos quilómetros entre nós vocês estão sempre presentes, sem vocês estes anos e este trabalho não fariam sentido nem seriam possíveis.

To mlÜ because new worlds are only worth being found if you can share them. For all your love and courage. For all the times we shared and specially for all the times that wait for us.

Enfim dum escolha faz-se um desafio
enfrenta-se a vida de fim a pavio
navega-se sem mar, sem vela ou navio
bebe-se a coragem até dum copo vazio
e vem-nos à memória uma frase batida
hoje é o primeiro dia do resto da tua vida

E entretanto o tempo fez cinza da brasa
e outra maré cheia virá da maré vasa
nasce um novo dia no braço outra asa
brinda-se aos amores com vinho da casa
e vem-nos à memória uma frase batida
hoje é o primeiro dia do resto da tua vida.

Sérgio Godinho

Curriculum Vitae

PERSÖNLICHE DATEN

Name	Ana Teresa Monteiro Tomás
Geburtsdatum	Januar 24, 1977
Geburtsort	Lisboa/Portugal
Staatsangehörigkeit	Portugiesin

SCHULBILDUNG

1983 - 1985	Jardim Escola João de Deus, Lisboa, Portugal
1985 - 1992	Colégio D. Afonso V, Mem-Martins, Portugal
1992 - 1995	Escola Secundária Sta. Maria, Sintra, Portugal

STUDIUM

1995 - 2000	Physics Diplom, Faculdade de Ciências, Universidade de Lisboa, Portugal
2000 - 2001	DEA Astrophysique et Millieux Diluée, Université Joseph Fourier, Grenoble, Frankreich

PROMOTION

Feb. 2002 - Jan. 2005	Stipendium des Max-Planck-Instituts für Sonnensystemforschung
-----------------------	--